THE DETECTION AND IDENTIFICATION OF EXTRANEOUS METALS IN MATERIAL CONVEYANCE SYSTEMS

BY

HUSSAIN JOM'A ABBAS, B.Sc., M.Sc.

Submitted for the degree of
Doctor of Philosophy
at the
University of Aston in Birmingham

Department of Electrical and Electronic Engineering

MAY 1984

THE UNIVERSITY OF ASTON IN BIRMINGHAM

THE DETECTION AND IDENTIFICATION OF EXTRANEOUS METALS IN MATERIAL CONVEYANCE SYSTEMS

Hussain Jom'a Abbas

A thesis submitted to the
University of Aston in Birmingham
for the degree of
Doctor of Philosophy 1984

Summary

The aim of this work was to design and build an equipment which can detect ferrous and non-ferrous objects in conveyed commodities, discriminate between them and locate the object along the belt and on the width of the belt. The magnetic induction mechanism was used as a means of achieving the objectives of this research.

In order to choose the appropriate geometry and size of the induction field source, the field distributions of different source geometries and sizes were studied in detail. From these investigations it was found the square loop geometry is the most appropriate as a field generating source for the purpose of this project. The phenomena of field distribution in the conductors was also investigated.

An equipment was designed and built at the preliminary stages of the work based on a flux-gate magnetometer with the ability to detect only ferrous objects. The instrument was designed such that it could be used to detect ferrous objects in the coal conveyors of power stations. The advantages of employing this detector in the power industry over the present ferrous metal electromagnetic separators were also considered.

The objectives of this project culminated in the design and construction of a ferrous and non-ferrous detector with the ability to discriminate between ferrous and non-ferrous metals and to locate the objects on the conveying system.

An experimental study was carried out to test the performance of the equipment in the detection of ferrous and non-ferrous objects of a given size carried on the conveyor belt. The ability of the equipment to discriminate between the types of metals and to locate the object on the belt was also evaluated experimentally. The benefits which can be gained from the industrial implementations of the equipment were considered.

Further topics which may be investigated as an extension of this work are given.

Key Words

DETECTION, DISCRIMINATION, LOCATION, METAL
ELECTROMAGNETIC INDUCTION (E.M.I.)

ACKNOWLEDGEMENTS

I am extremely grateful to my supervisor, Dr. R. L. Brewster, for advice, patient and personal guidance, inspiration and many productive discussions which covered all aspects of the work.

I would like to thank Professor J. E. Flood, Head of the Department of Electrical and Electronic Engineering, for the provision of equipment, technical staff and other extensive departmental facilities.

Thanks are also due to the Technicians in the Department of Electrical and Electronic Engineering who assisted in building the experimental rig.

Finally, I wish to express my thanks to Helen Turner for typing the thesis, whose perfectionism greatly enhanced the presentation.

CONTENTS

Page

CHAPTER TWO

Page

CHAPTER SEVEN

LIST OF FIGURES

Figure Page

Figure Page

LIST OF TABLES

Chapter One

Introduction

INTRODUCTION

All powder producers and bulk material processors are continually seeking ways to increase production, improve the quality of the product and lower the operating costs. An obstacle on the way to these aims can be damaging tramp metal. When the presence of the tramp metal is ignored one or more costly events may occur (1,2).

(1) Damage to the processing machinery, dies, etc., resulting in considerable costs for repair and replacement parts and sometimes shutdowns and production loss.

(2) Contamination of the end product. Producers of plastics, cement, fertilizers, chemicals, paper products, pharmaceuticals, food, etc. strive to produce products free of metal contamination. The food and milling industries are especially vulnerable when even fine slivers of metal are discovered in their products.

(3) Explosions and fires.

To prevent the occurrence of these events, more magnetic separators, metal detectors and vibratory feeder-screens are being employed, not only at the beginning of the material entry and along processing lines but immediately ahead of bagging, packaging, canning or bulk shipping.

Most of the available metal detectors are designed with a very limited range especially to detect metals buried just under the surface of the earth. The detector employed currently for the detection of metal within a processing material carried on a conveying system in most of the industrial fields is the inductive loop metal detector(2). This equipment derives its operation from the change of the loop inductance when a metal object passes through it. The search coil in this detector is part of a tank circuit and the reactance of the circuit is sensitive to the capacitance as well as to the inductance. Thus any change in the stray capacitance for any reason may be significant enough at the operating frequency of the detector to cause the system to give false detection. The above factors reduce the sensitivity, accuracy and reliability of the equipment. Currently available detectors are generally unable to discriminate between ferrous and non-ferrous metals or to locate the object on the conveyor belt.

The ultimate objectives of this research were to design and build a metal detector that would detect ferrous and non-ferrous objects carried on a conveying system, discriminate between them and locate them along the belt and on the width of the belt.

At the early stages of the work a metal detector was designed based on the flux-gate magnetometer which has the ability of detecting only ferrous objects. This equipment may be used to detect tramp iron within the coal material in the power industry and control the operation of electromagnetic separators used for removing the iron pieces from the coal. The process of controlling the separator and putting it on only when required leads to a considerable saving in energy, since the presence of tramp iron in the coal is very rare. Also, it increases the efficiency of extraction of the iron objects and reduces the overall cost of the separator as its intermittent operation allows the coil to be wound using thinner wire and less cooling is required.

To achieve the complete objectives of this research a detector has been designed and built based on the transmit-receive coil configuration. The design was evaluated for detection of ferrous and non-ferrous objects, discrimination between them and location of the object on the belt.

An experimental rig was constructed and the performance of the equipment tested to determine how well it met the design objectives. The facility to discriminate between ferrous and non-ferrous metals enables the detector to be used for the detection of ferrous objects within the non-ferrous materials and vice-versa. Locating the object on the belt makes the removing of the tramp metal from the material a simple matter once the belt is stopped, thus reducing the period of interruption of production.

In Chapter 2 of this thesis, a survey of the literature relevant to metal detection is given with an indication of the deficiencies of various methods in relation of the current problem.

Chapter 3 contains an investigation of the magnetic field distributions of different source geometries. It also includes the selection of the appropriate source geometry for the purpose of this project.

Chapter 4 covers the theoretical principles of operation and practical development of the ferrous metal detector based on the flux-gate magnetometer.

Chapter 5 deals with the theoretical basis of the ferrous and non-ferrous equipment design. It also describes the principles of operation of the different functions of the equipment in detail.

Chapter 6 describes in detail the practical development of the ferrous and non-ferrous metal detector, together with the experimental tests carried out on the performance of the equipment.

The conclusions and suggestions for further work are presented in Chapter 7.

Chapter Two

A short review of detectors using an electromagnetic induction mechanism

2.1 INTRODUCTION

In this chapter, mention is made of some of the applications of the electromagnetic induction mechanism and the literature related to the topic of metal detection is reviewed. Brief descriptions of available detectors are given. The remainder of the chapter describes the general scope of the present work and details the important factors involved in the development of the prototype equipment.

Electromagnetic induction detection has been used in many different applications. Among these is that of vehicle detection(3,4,5,6) starting with its simple detector and ending with quite sophisticated techniques. Other typical applications include the locating of buried objects such as underground pipes and telephone cables(7,8). The mechanism has also been used at very low frequencies to communicate in the sea(9,10). The technique has been used for the detection of submarines under the surface of the sea and weapons buried under the ground(11). The relevant literature revealed various applications of electromagnetic induction in different fields such as, medical(12), industrial(13), military, communications(14) (for short ranges) and geological science(15,16).

Various metal detectors based on electromagnetic induction techniques have been described in the literature.

All such instruments depend on the measurement of magnetic field associated with eddy currents induced in the metal target by a primary magnetic field produced by an excitation coil.

2.2 A SHORT REVIEW OF METAL DETECTORS

2.2.1 The B.F.O. (Beat Frequency Oscillator) Detector

The principle of operation of the b.f.o. detector is described in Ref. (17) and illustrated in Fig. 2.1.

The b.f.o. detector consists of two oscillators with resonant frequencies within 10 Hz of each other. Oscillator (2) operates at a fixed frequency above that of oscillator (1). However, the detector's search coil forms part of the tuned circuit of oscillator (1). This means that any change in the inductance of the search coil will change the resonant frequency of oscillator (1). When the detector's search coil is brought near a metallic object, the inductance of the coil changes and hence the resonance frequency of the search oscillator changes. The output from both oscillators is fed into a mixer and the difference frequency emerges. This output is then processed to give an indication of a metal target. This system is very crude because there are two oscillators of similar frequencies operating in the same unit. This requires very good shielding since the two oscillators will tend to pull together to the same frequency and remain locked.

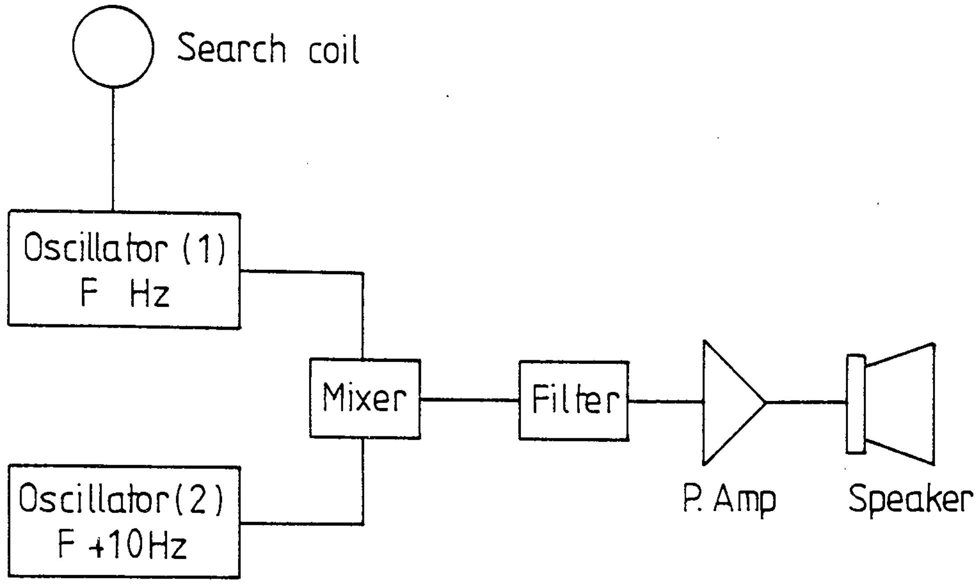

Fig 2.1 Beat frequency oscillator detector.

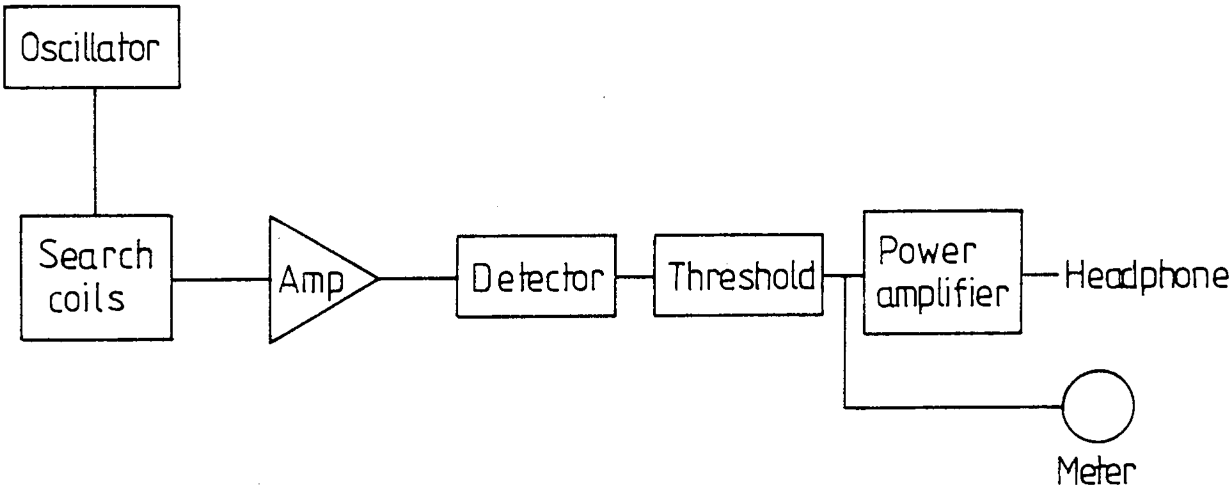

Fig 2.2 Block diagram of a typical Induction balance detector

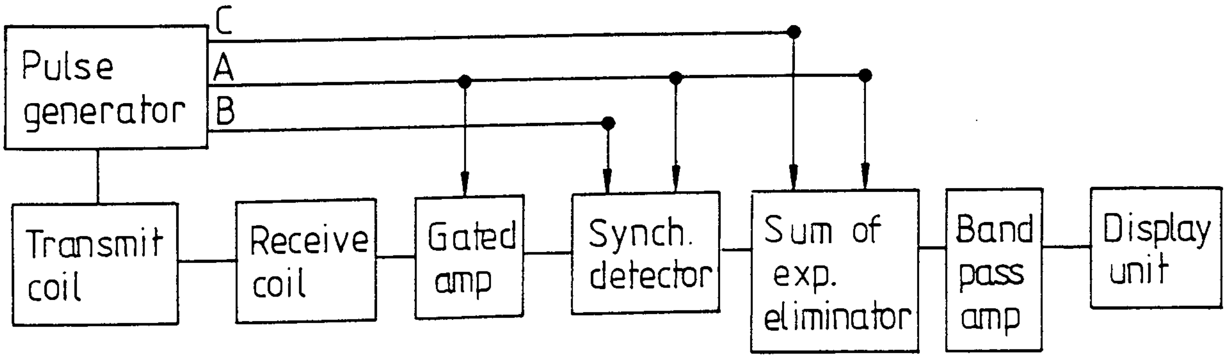

Fig 2.3 Block diagram of pulse induction detector.

A development of the b.f.o. detector is the discriminative metal detector. In this type of detector, instead of measuring the difference frequency between the two oscillators, the phase change between the two is measured. This increases the sensitivity since phase changes between the two frequencies can be much more easily detected.

Waddington(17) states that the equipment is discriminative because the sign of the phase change is dependent upon the type of metal near the search coil. Actually the discriminating process of this instrument is not always accurate, because the net effect of the ferrous metal object within the primary field on the sign of the phase shift is a function of the combination of both eddy currents and enhancement effect. It is therefore impossible to discriminate between ferrous and non-ferrous objects reliably.

A further problem concerned with this detector is the change in the frequency of oscillation due to changes in the reactance of the tank circuit. It is thus susceptible to both capacitance and inductance changes. This can lead to false detection and hence reduce the resolution of the system for the detection of metallic objects.

2.2.2 Induction Balance and Pulse Induction Detectors

Fig. 2.2 is the block diagram for the induction balance metal detector. The operation of the detector is based on the detection of the magnetic field associated with eddy currents induced in the metal(18). The oscillator (running at 100 - 120 kHz) drives a search coil and creates an alternating magnetic field around the search head. A pick-up coil is placed within this field. This coil is positioned so that the fields around it normally oppose each other and hence no output appears across it. A piece of metal within the searching field produces an imbalance which results in an output from the pick-up coil.

Both coils are normally tuned as this increases sensitivity. The detectors commercially available are limited in the range of detection and they cannot discriminate between ferrous and non-ferrous metals.

Pulse induction detectors have been described by Grant and West(19). A recently developed pulse induction detector is described by Corbyn(20). In this system a high current is passed through the drive coil, creating a strong magnetic field. This field is then allowed to collapse. At the start of the pulse the field is built up; at the switch off, or the end of the pulse, the collapsing field causes the output initially to shoot up in the opposite direction, then die rapidly away to zero. A metal object within the range of the system would have an eddy current induced in it. This in turn produces a field of its own, opposing the main field collapse and slowing it down. This would produce an output which is processed to indicate the presence of a metal target. The block diagram of one type of pulse induction metal detector is shown in Fig. 2.3.

2.2.3 Inductive Loop Detectors

Inductive loop detectors were used initially for traffic sensing(3). The loop is sunk into the surface of the road and sealed in with tar. The detection zone is very well defined by physical size of the loop, and a bigger area can easily be covered by paralleling of loops. The loop is energised by high frequency current and the presence of a metallic object in the electromagnetic field will cause a net decrease in the inductance of the loop due to the eddy currents induced in the object. Several loop detectors have been designed around the principle of change of inductance of the loop. One type is the self-tuning detector. Here the loop is part of a tuned tank circuit and a feedback loop is used to adjust the frequency of the oscillator to keep the detector automatically tuned to the same amplitude on the resonance curve. A change in the loop inductance due to the metal object shifts the resonant frequency of the tank circuit, which results in a change in the feedback voltage. The latter is used to indicate the presence of a metallic object.

A second type is the bridge balance detector. In this case, the loop forms one leg of a balanced bridge circuit and change of the inductance causes the balance of the bridge to be upset. This results in a change in the output signal which indicates the presence of the object.

In the phase shift detector the loop is tuned to the resonance. In this detector, the change in the relative phase-shift in the tank circuit, which is produced by a metallic object changing the loop inductance, is used as an indication of metal presence.

There are many metal detectors commercially available based on these principles and used for the detection of metal on conveyor belts. The change in the resonance condition of the detector depends on the change of the inductance of the search coil caused by the presence of a metallic object. Since the change of the inductance of the coil is very small compared to the total inductance of the loop(21), the change in the resonance condition is also very small. This results in a crude senstivity of the equipment for the detection of metal objects. The detector is also sensitive to changes in the capacitance of the tank circuit as well as to its inductance. The capacitance of the tank circuit includes the stray capacitance which may be considerable at the operating frequency of the detector. Any change in this capacitance for any reason will therefore affect the resonance of the tank circuit. The equipment is also affected by changes in temperature and humidity. All the above factors can lead to a false detection and reduce the efficiency of the processing plant. The block diagram of the phase sensitive inductive loop detector is shown in Fig. 2.4.

2.2.4 VLF Transmit-receive (T/R) Metal Detectors

Standard transmit-receive (T/R) detectors have been

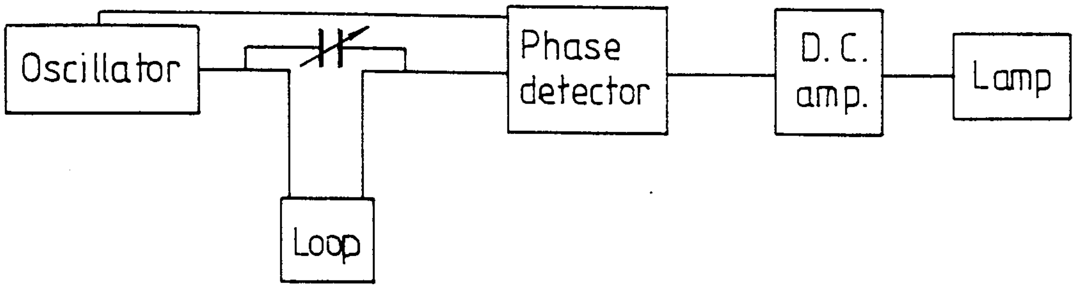

Fig 2.4 Block diagram of inductive loop phase sensitive detector.

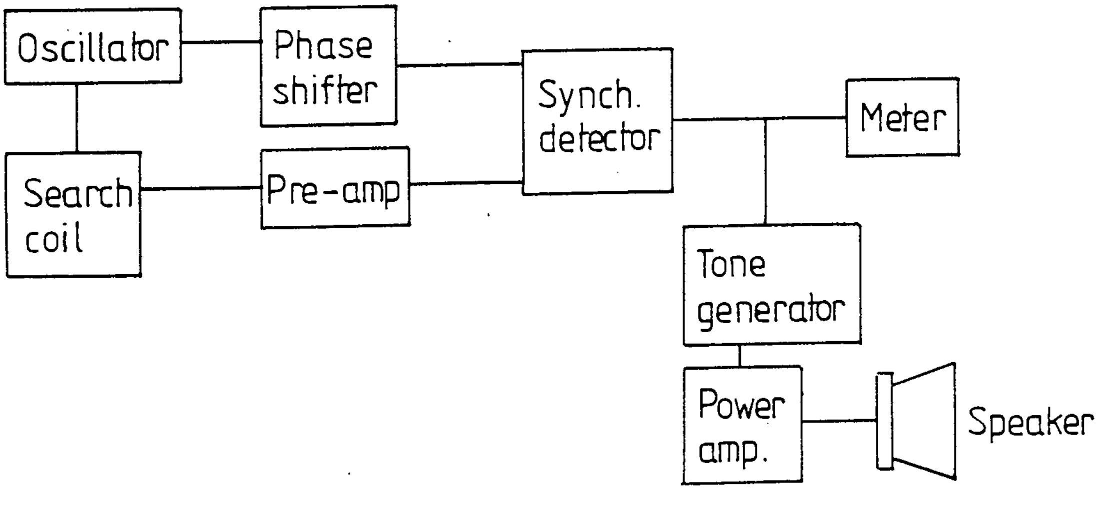

Fig 2.5 Block diagram of very low frequency metal detector.

available for several decades. Most of them operate within the frequency range of between 50 kHz and 100 kHz. The VLF metal detector's operating frequency covers the range of 3 kHz to 30 kHz. These detectors are usually designed to detect metal objects buried under the ground. By decreasing the frequency, the electromagnetic field produced by the transmitting coil penetrates more deeply into the ground and hence the detection range of the VLF detectors extends into the ground more than the standard (T/R) detectors(22). The principle of operation and design of VLF metal detectors are described in Refs. (22,23,24). However the theory of the VLF detector is reviewed here briefly. The oscillator power is fed into the transmitter coil which generates an electromagnetic field around the coil. The field penetrates the ground and, if metal is buried in the ground, eddy currents are thus generated on the surface of the metal target. These currents in turn generate their own electromagnetic field. A portion of this field is received by the pick-up coil which is situated in the field such that its output is zero when there is no metallic object in the field of the transmitting coil. The output of the receive coil due to the presence of metallic object is then processed to indicate the presence of metal.

The commercially available detectors of this type have been designed either to detect both ferrous and non-ferrous metal without discriminating between them or to detect the non-ferrous and reject the ferrous objects. Also, the detection range of these VLF detectors is limited, because the transmit and receive coils are both placed in the same plane(23). This arrangement causes the electromagnetic field to travel double the distance between the search coils and the metallic objects buried under the ground. The detection range may be improved for other applications by situating the transmitting and receiving coils in parallel planes and passing the materials (in the case of conveyed materials) to be inspected by the detector between the coils. The block diagram of the VLF metal detector is shown in Fig. 2.5.

A metal detector has been developed recently for tracing submarine telecommunication cables. The equipment is based on similar principles to the very low frequency transmit-receive detector. The theoretical basis and development of this detector is described in detail in reference (25).

2.3 GENERAL SCOPE OF THE WORK

2.3.1 Objectives of the Work

As a result of the review of the relevant literature, it was noted that most of the metal detectors were designed to detect objects buried just under the surface, and they have a very limited range of detection. To cover the complete width of conveyor belts used in material processing plants, it is necessary to use several detecting heads, which makes the system very costly and unreliable. It was also found that none of the available detectors are discriminative. They have been either designed to detect both ferrous and non-ferrous objects without distinguishing between them or detect the non-ferrous and reject the ferrous objects. It was also noted that most of the relevant literature publications do not include theoretical analysis of the detection principles.

The present work is aimed at designing and building an equipment to detect metal objects carried on conveyor belts, discriminate between ferrous and non-ferrous objects and locate the object along the belt and on the width of the belt. The proposed equipment has been designed such that it does not give false detection due to the changes of stray capacitance, temperature and humidity. This makes it more reliable than the currently available detectors. The detection range of the equipment is such that it is capable of covering the complete area of the given conveying system. By using a suitable geometry for the system, the sensitivity of the system may be increased over that of currently available conveying system detectors.

2.3.2 General Approach to the Problem

At the preliminary stages of the work the proposal was to use a flux-gate magnetometer as a means of sensing the presence of metallic objects in the processing material, in conjunction with an a.c. exciting field. In this way, the effect of the earth's magnetic field may be eliminated. In proceeding with the project, it was found that the flux-gate based detector cannot sense non-ferrous objects, but only detects ferrous objects (with specified size) due to the frequency bandwidth limitation of the flux-gate magnetometer which means that the excitation frequency cannot be increased to produce significant eddy currents. To overcome this problem a new design approach has been used. Based on this approach, an equipment was built employing the transmit-receive mechanism. The transmit and receive electromagnetic coils are situated orthogonal to each other and receiving coil was electromagnetically balanced against transmitting coil. There is therefore, no energy coupling between the coils as long as the balance is maintained. In this way it is possible to achieve the objectives described above. Further discussion of these factors is to be found later in the thesis.

2.4 KEY FACTORS IN THE DEVELOPMENT OF THE PROTOTYPE EQUIPMENT

To design and develop a suitable system, performance limiting factors have to be firmly established, and taken into account. This section summarises the key factors in the work. It should be noted that the main theme of the thesis is the practical development of equipment, and full details are given in Chapter 6.

2.4.1 The Principle of Detection and Sensitivity of the Equipment

In a normal transmit/receive detector, the transmitter coil is fed with power from an a.c. oscillator. This sets up a magnetic field around the coil and any metal which enters this field has eddy currents induced in it. These circulating eddy currents in turn generate their own magnetic field which radiates outwards and it is this field which the receive coil detects. The magnitude of the eddy currents induced, and hence the sensitivity of the equipment for a given size and distance of the object from the receiving coil, depends on the magnitude of the field at the point at which the metal object exists. The geometry of the transmitting electromagnetic coil should be optimised for maximum sensitivity. For a particular conveying system, it is necessary to generate the maximum field possible at each point in the space for a given exciting power. The geometry of the receiving coil should also be optimised for maximum possible sensitivity. By careful positioning of the receive coil, the net flux produced by the transmit coil linking the receive coil can be reduced to zero. Optimising the distance between the transmitting and receiving coil for a certain conveying system enables the overall sensitivity of the equipment to be maximised. When the metallic object enters the field it will upset the balance and detection starts at this point. The detailed theoretical analysis of the detection principles, and the practical development of the equipment are to be found in the following chapters.

2.4.2 The Importance of Tuning

The detector operates over such short ranges, relative to the radiation wavelength, that the energy of the induction field is much greater than that of the radiated field. The sensitivity of the equipment depends on the transfer of energy from the transmitting loop to the metallic object via the induction field for a given distance from the receiving coil. To maximise the transfer of energy, the magnetic flux at each point of interest should be made as large as possible. This is simply achieved by series tuning the transmitting loop to increase the current.

The receiving coil should also provide as large an induced voltage as possible from a given value of energy transferred from the metallic object to the receiving coil. Here again, series tuning directly increases performance by magnifying the induced emf. High permeability ferrite rods are used in the receiving transducer. This increases the induction energy picked-up and further magnifies the resultant voltage because the ferrite significantly increases the coil 'Q'. The increase in 'Q' reduces the bandwidth of the equipment and increases the accuracy of the detection. Tuning, Q factor and self-capacitance problems are extensively discussed later.

2.4.3 Discrimination of Ferrous and Non-ferrous Metal

When a metallic target enters the electromagnetic field of the transmitting loop and modifies it, (Chapter 5) a small signal appears at the output of the receiving coil. This voltage is amplified by the preamplifier. Using the signal from the search oscillator as a reference and comparing the time phase of the picked-up signal with the reference, it is found that there is a phase shift between the two signals. In the case of non-ferrous objects the phase difference is 45° because the non-ferrous metal is magnetically linear and the permeability is that of free space. When the metal is ferrous metal, the phase of the picked-up signal is dependent on the size and position of the object, because the received signal is due to the composite function of the eddy currents effect and the intensifying effect arising from the high permeability of the material. By using a phase shifter to modify the phase of the reference signal and a phase sensitive detector, it is possible to discriminate between ferrous and non-ferrous metal. The operating principle of the discrimination is given later.

2.4.4 Location of the Position of the Object on the Belt

The position of the object on the belt is located in two steps.

(1) Finding the object on the left hand side or right hand side of the belt,

(2) Measuring the distance of the object on either side from the edge of the belt.

To determine on which side of the belt the object is situated, another receiving coil has been employed with its axis perpendicular to the first receiving coil and directly underneath it. This coil is also balanced against the transmitting coil and a metallic object in the field will disturb the balance. The coil detects the effect of the disturbance in the direction parallel to the axis of the coil. By using a phase shifter and a phase sensitive detector it is possible to determine the side on which the object is situated.

The position of the object on either side of the belt is found by measuring the time taken by the object to travel within the boundaries of the loop in the direction of the belt. The measured time is then converted into a distance, calibrated to give the position of the object from the edge of the belt. The theoretical analysis and the development technique of the object location technique is described in greater detail later in the thesis.

2.5 SUMMARY

The general literature concerned with detectors using the electromagnetic induction mechanism has been reviewed briefly in this chapter. It was found that literature related to the metal detector is very small, and most of it consists of technical reports which give little attention to investigating the theoretical analysis of the operating principle. The chapter also included the general approach to the objectives of the present work and brief discussion of the key factors involved in the practical development of the equipment.

Chapter Three

Electromagnetic field distributions for different source geometries

3.1 INTRODUCTION

The theory associated with electromagnetic fields generated by different source geometries has been studied by many authors. The publications are far too numerous to mention them all. A selected number of the more important contributions relating to this work are therefore highlighted in the following discussion.

Any conducting element subjected to a time-varying current will set up a propagating eletromagnetic wave and an induction field. However, the amplitude of the radiated energy is proportional to the product of current and frequency. When the electromagnetic source is very small compared to the wavelength of the time-varying current, the conductor does not radiate significant energy. Only at higher frequencies, when phase-shifts in the aerial become significant, is the radiated eletromagnetic energy significant(26). In the case of very long wavelengths of the current compared to the dimensions of source, most of the energy is stored in the induction field and confined to the vicinity of the source(9,27,28). The magnitude of the energy in the induction field is proportional to the current and depends on the spatial geometry of the source.

The sensitivity and range of the detectors described in this thesis depends on the magnetic field distribution of the field sources. It is therefore important to calculate the field distribution for various source geometries at different points in the space near the detection zone.

In this chapter, the field distribution for different source geometries which may be used in the present work are investigated. The chapter also includes a study of the time-varying electromagnetic field in the conductors, in order to establish some theoretical principles for the equipment design.

3.2 I-SHAPE CORE ELECTROMAGNETIC COILS

3.2.1 Short Core Electromagnetic Coils

If a small electric coil is subjected to sinusoidally oscillating current $I e^{j\omega t}$, the coil is equivalent to a short magnetic dipole of length ℓ and pole strength q_m at each end of the dipole(26,28). When the dimensions of the dipole are very small compared to the wavelength and range, the magnetic field components produced by the dipole in the space are as follows(9,29):-

$$H_\theta = \frac{q_m \ell \sin\theta}{4\pi} e^{j(\omega t-\beta_r)} \left[-\frac{\beta_o^2}{r} + \frac{j\beta_o}{r^2} + \frac{1}{r^3} \right] \qquad (3.1)$$

$$H_r = \frac{q_m \ell \cos\theta}{2\pi} e^{j(\omega t-\beta_r)} \left[\frac{j\beta_o}{r^2} + \frac{1}{r^3} \right] \qquad (3.2)$$

where $q_m \ell$ = magnetic dipole moment

β_o = phase constant of free space

$= \frac{\omega}{c}$

ω = frequency of the excitation current in rad/sec.

c = velocity of the light

θ = the angle between the axis of the coil and radial distance r.

r = radial distance from the centre of the coil to the point at which the field is to be measured.

If the wavelength of radiation considered is very much larger than r then quasi-static conditions prevail and only the $\frac{1}{r^3}$ terms predominate; the other terms become negligible under such conditions. The quasi-static condition is applicable to all cases considered in this work. Under this condition the field equations reduce to:

$$H_r = \frac{q_m \ell \cos\theta}{2\pi r^3} \tag{3.3}$$

$$H_\theta = \frac{q_m \ell \sin\theta}{4\pi r^3} \tag{3.4}$$

3.2.1.1 Horizontal Magnetic Dipole

The arrangement of the horizontal magnetic dipole is shown in Fig. 3.1(a).

The component of the field along the x-direction in the x-y plane is found from equations (3.3) and (3.4) to be:

$$H_x = \frac{q_m \ell (2x^2-y^2)}{4\pi (x^2+y^2)^{5/2}} \tag{3.5}$$

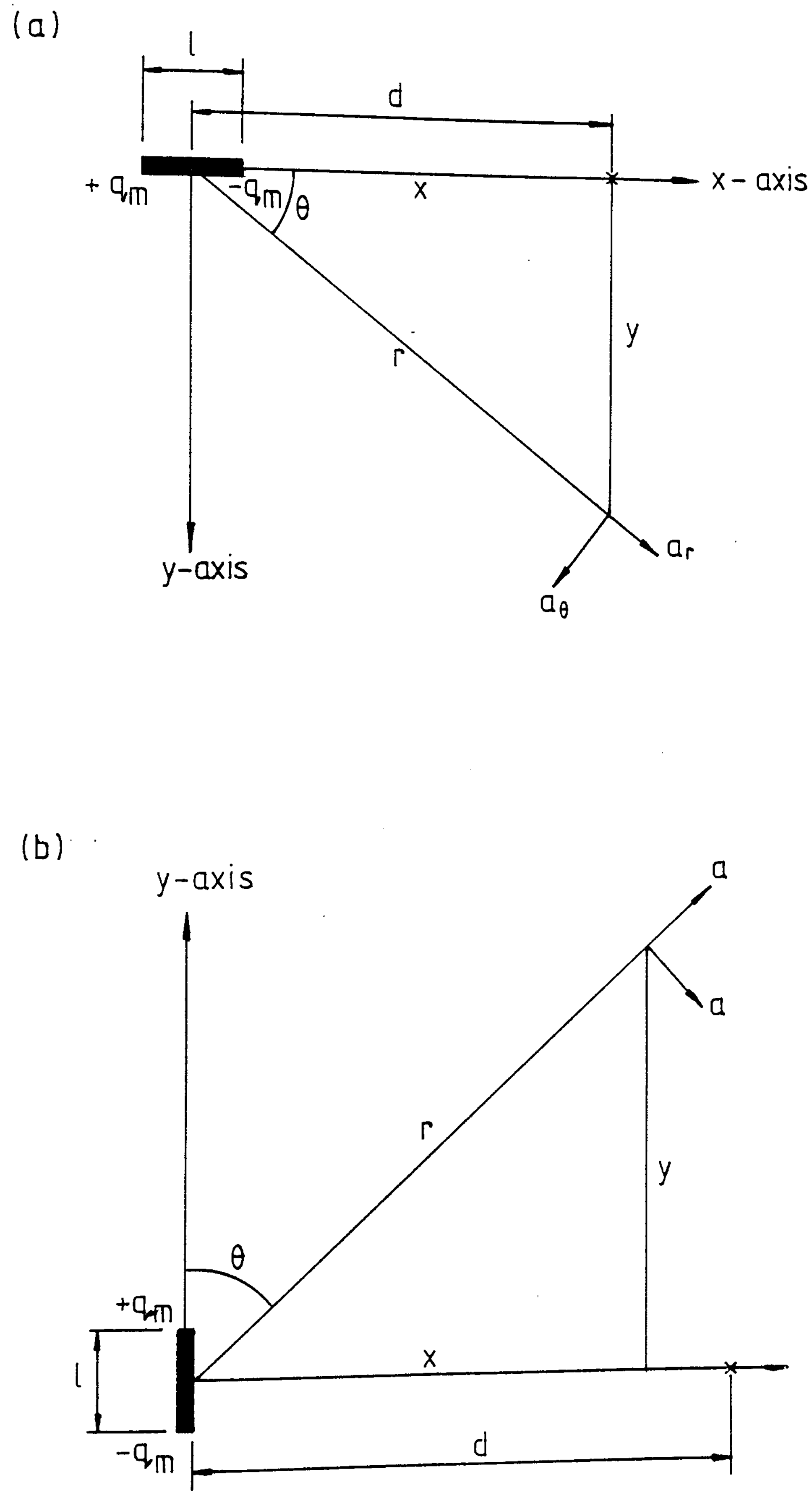

Fig 3.1 Magnetic dipole geometry
(a) horizontal (b) vertical

In the above equation, putting;

$x = k_1 d,$ $\qquad k_1 = 0.1$ to 1

$y = k_2 d,$ $\qquad k_2 = 0$ to 1,

the normalised field =

$$\frac{H_x d^3}{q_m \ell} = \frac{2k_1^2 - k_2^2}{4\pi (k_1^2 + k_2^2)^{5/2}} \tag{3.6}$$

where d, as shown in Fig. 3.1.(a), is the distance between the coil and a point on the x-axis to which the distribution of the field in the x-y plane is calculated. All other parameters are as stated in Section 3.2.

The field distribution of this geometry was determined at different points in the x-y plane. It was found that the field falls rapidly as the distance from the x-axis increases. The result of the calculations for $k_1 = 0.5$ is given as Fig. 3.2.

3.2.1.2 Vertical Magnetic Dipole

This geometry is shown in Fig. 3.1.(b). The normalised field in the x-direction for this geometry is given by:

$$\frac{H_x d^3}{q_m \ell} = \frac{3k_1 k_2}{4\pi (k_1^2 + k_2^2)^{5/2}} \tag{3.7}$$

All the parameters in the above equation are as defined previously.

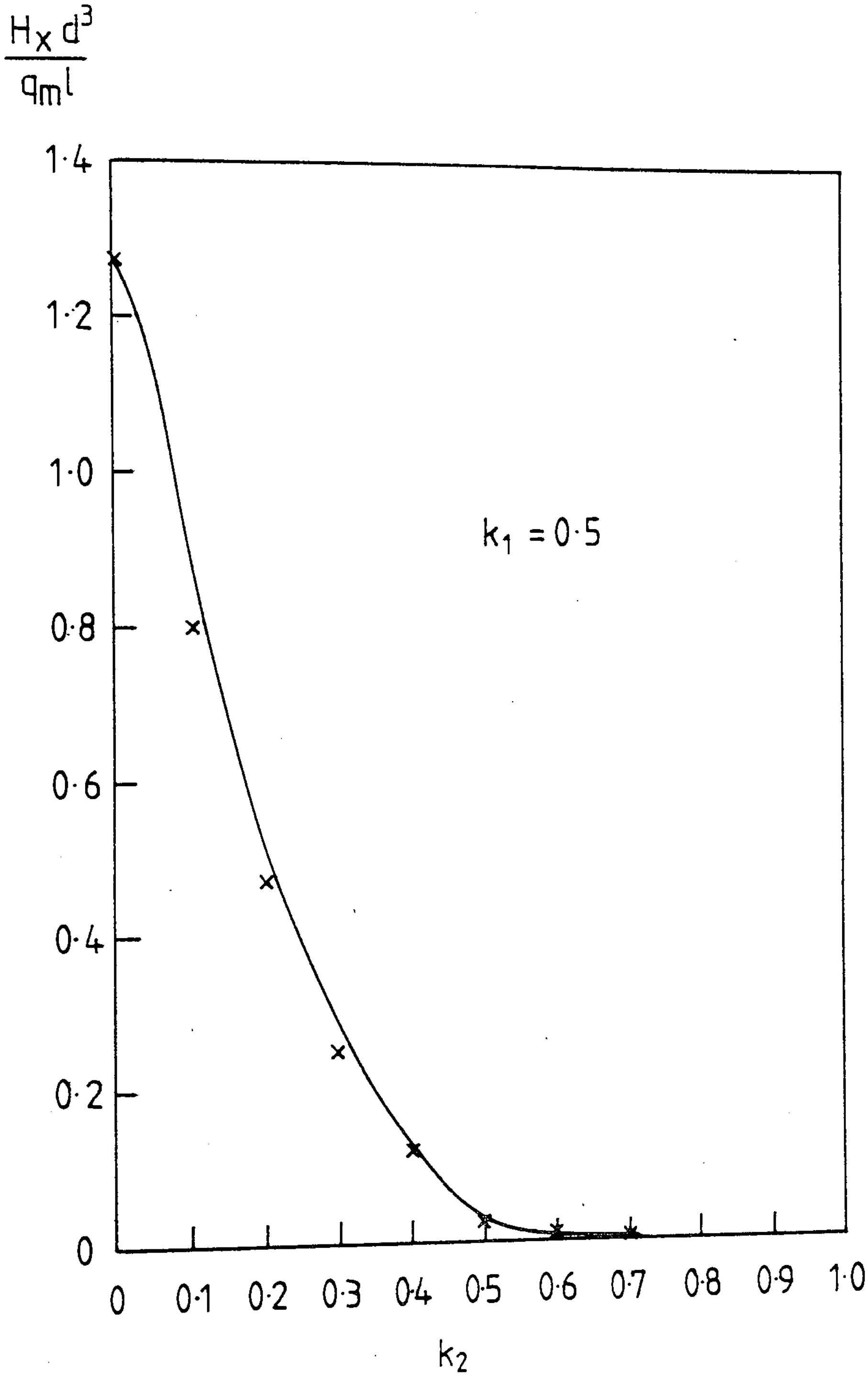

Fig 3.2 The distribution of the normalized x component of the field produced by a horizontal magnetic dipole along y-axis.

The field was calculated for different values of k_1 and k_2. The result for $k_1 = 0.5$ is shown in Fig. 3.3. The field of this geometry is zero at the centre-line of the coil and increases with distance from the centre-line until a maximum value is reached. Thereafter it starts to decrease.

3.2.2 Long Core Electromagnetic Coils

If the length of the core of an electromagnetic coil is not small compared to the distance between the coil and a point to which the field is to be calculated, then equations (3.3) and (3.4) cannot be used to determine the field distribution in close proximity to the coil producing the field. The field equations in the x-direction for horizontal and vertical geometries of long core coils at any point in the x-y plane are derived in the following sections 3.2.2.1 and 3.2.2.2.

3.2.2.1 Horizontal Geometry of the Long Core

The coil is regarded as a bar magnet of length ℓ and pole strength q_m at each end of the bar. The arrangement of the system is given in Fig. 3.4.(a).

The field components due to long bar magnet at any point in space may be found by considering the effect of each pole, and the total field in any direction is found by superposition(29).

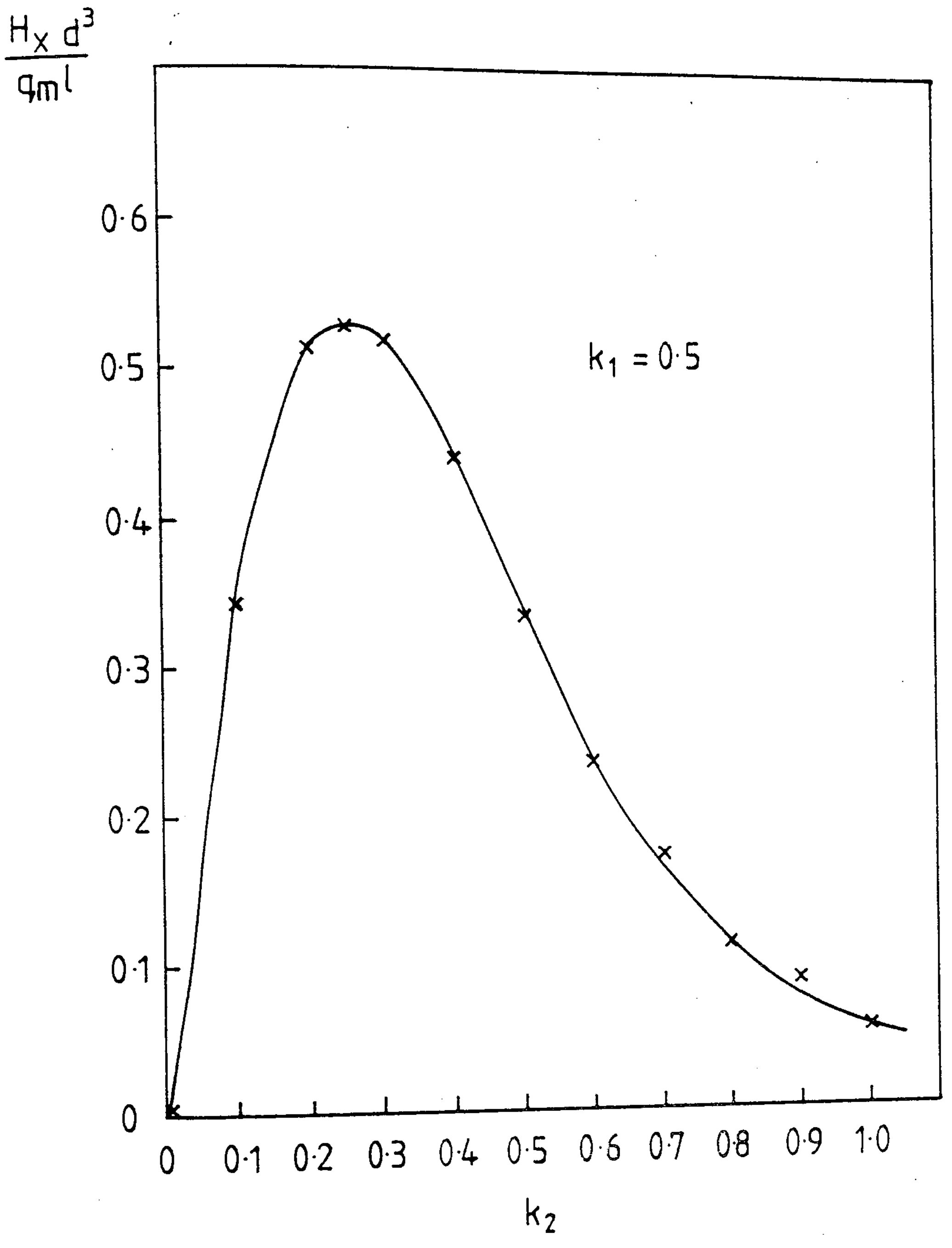

Fig 3.3 The distribution of the normalized field in the x direction produced by a vertical magnetic dipole along the y-axis.

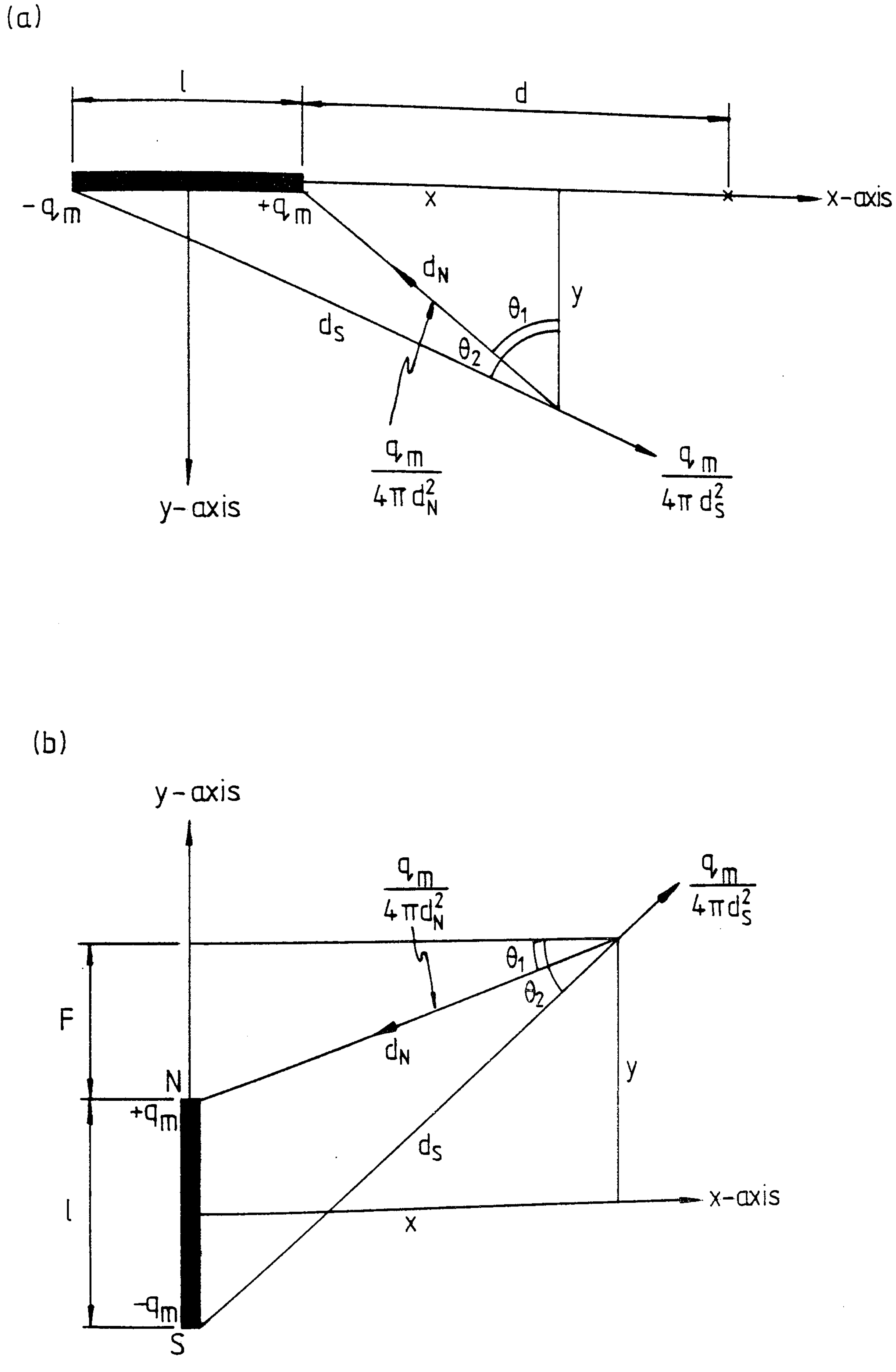

Fig 3.4 Long core coil geometry
(a) horizontal (b) vertical

In Fig. 3.4.(a)if

$\ell = k_1 d,$ $\quad k_1 = 0.1$ to 1

$y = k_2 d,$ $\quad k_2 = 0$ to 1

$x = k_3 d,$ $\quad k_3 = 0.1$ to 1

The x-component of the field in the x-y plane for the north pole is:

$$H_{xN} = \frac{q_m k_3}{d^2 4\pi (k_2^2 - k_1 k_2 + \frac{k_1^2}{4} + k_3^2)^{3/2}} \tag{3.8}$$

and

$$H_{xS} = \frac{q_m \ k_3}{4\pi d^2 (\frac{k_1^2}{4} + k_1 k_2 + k_2^2 + k_3)^{3/2}} \tag{3.9}$$

where subscripts N and S refer to the north and south pole respectively. The total field in x-direction H_{xT} is:

$$\begin{aligned} H_{xT} &= H_{xN} - H_{xS} \\ &= \frac{q_m k_3}{4\pi d^2} \left(\frac{1}{(k_2^2 - k_1 k_2 + \frac{k_1^2}{4} + k_3^2)^{3/2}} \right. \\ &\quad \left. - \frac{1}{(\frac{k_1^2}{4} + k_1 k_2 + k_2^2 + k_3^2)^{3/2}} \right) \end{aligned} \tag{3.10}$$

The normalised field =

$$\frac{H_{xT}d^2}{q_m} = \frac{k_3}{4\pi}\left(\frac{1}{\left(k_2^2 - k_2k_1 + \frac{k_1^2}{4} + k_3^2\right)^{3/2}}\right.$$

$$\left. - \frac{1}{\left(\frac{k_1^2}{4} + k_1k_2 + k_2^2 + k_3^2\right)^{3/2}}\right) \qquad (3.11)$$

where d and q_m are as defined in section 3.2.1.

The normalised field has been calculated for different values of k_1, k_2 and k_3. The results of the calculations for $k_3 = 0.5$ are shown in Fig. 3.5. From these graphs, it is seen that the field is maximum on the axis of the coil and decreases as the distance from the axis increases. The rate of decrease of the field depends on the length of the core. For longer cores, the rate of decrease of the field with increase in distance from the axis of the coil is slower.

3.2.2.2 Vertical Geometry of the Long Core Coil

Fig. 3.4.(b)shows the vertical geometry of the long core coil.

The x-component of the field H_{xT} for this geometry is found in a similar way to that for horizontal geometry.

$$H_{xN} = \frac{q_mk_3}{4\pi d^2\left(k_2^2 - k_2k_1 + \frac{k_1^2}{4} + k_3^2\right)^{3/2}} \qquad (3.12)$$

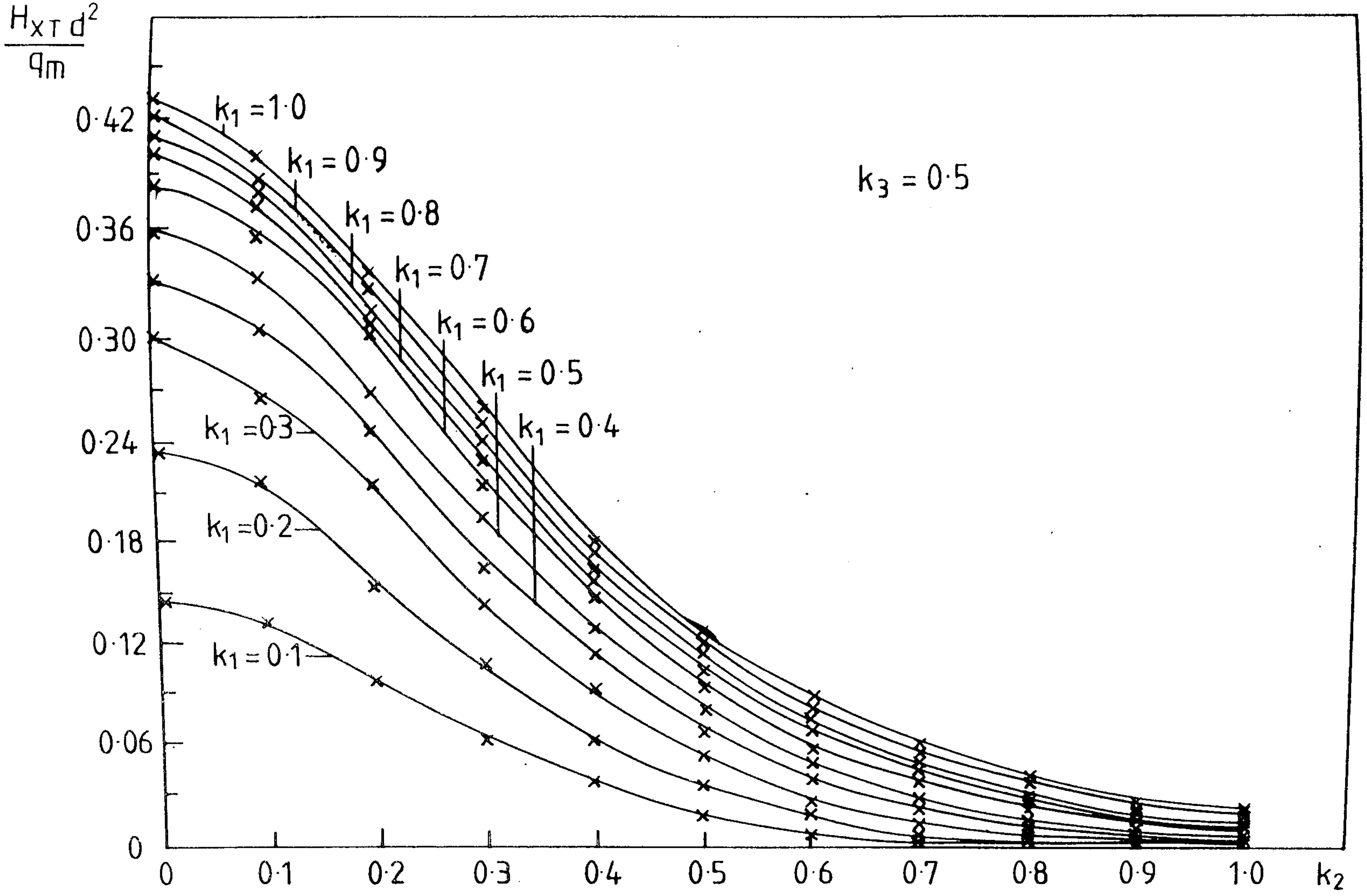

Fig 3.5 The distribution of the normalized field in the x direction produced by a horizontal coil for different lengths of the core of the coil versus distance along the y-axis.

$$H_{xS} = \frac{q_m k_3}{4\pi d^2 (\frac{k_1^2}{4} + k_1 k_2 + k_2^2 + k_3^2)^{3/2}} \qquad (3.13)$$

$$H_{xT} = H_{xN} - H_{xS} = \frac{q_m k_3}{4\pi d^2} \left(\frac{1}{(k_2^2 - k_2 k_1 + \frac{k_1^2}{4} + k_3^2)^{3/2}} \right.$$

$$\left. - \frac{1}{(\frac{k_1^2}{4} + k_1 k_2 + k_2^2 + k_3^2)^{3/2}} \right) \qquad (3.14)$$

The normalised field =

$$\frac{H_{xT} d^2}{q_m} = \frac{k_3}{4\pi} \left(\frac{1}{(k_2^2 - k_2 k_1 + \frac{k_1^2}{4} + k_3)^{3/2}} \right.$$

$$\left. - \frac{1}{(\frac{k_1^2}{4} + k_1 k_2 + k_2^2 + k_3^2)^{3/2}} \right) \qquad (3.15)$$

All the parameters are as defined in the previous section.

The normalised x-component of the field has been determined for various k_1, k_2 and k_3. The calculated fields are plotted in Fig. 3.6. It can be seen from these results that as the length of the core is increased, the point at which the field is maximum moves from the centre-line of the coil along the y-direction.

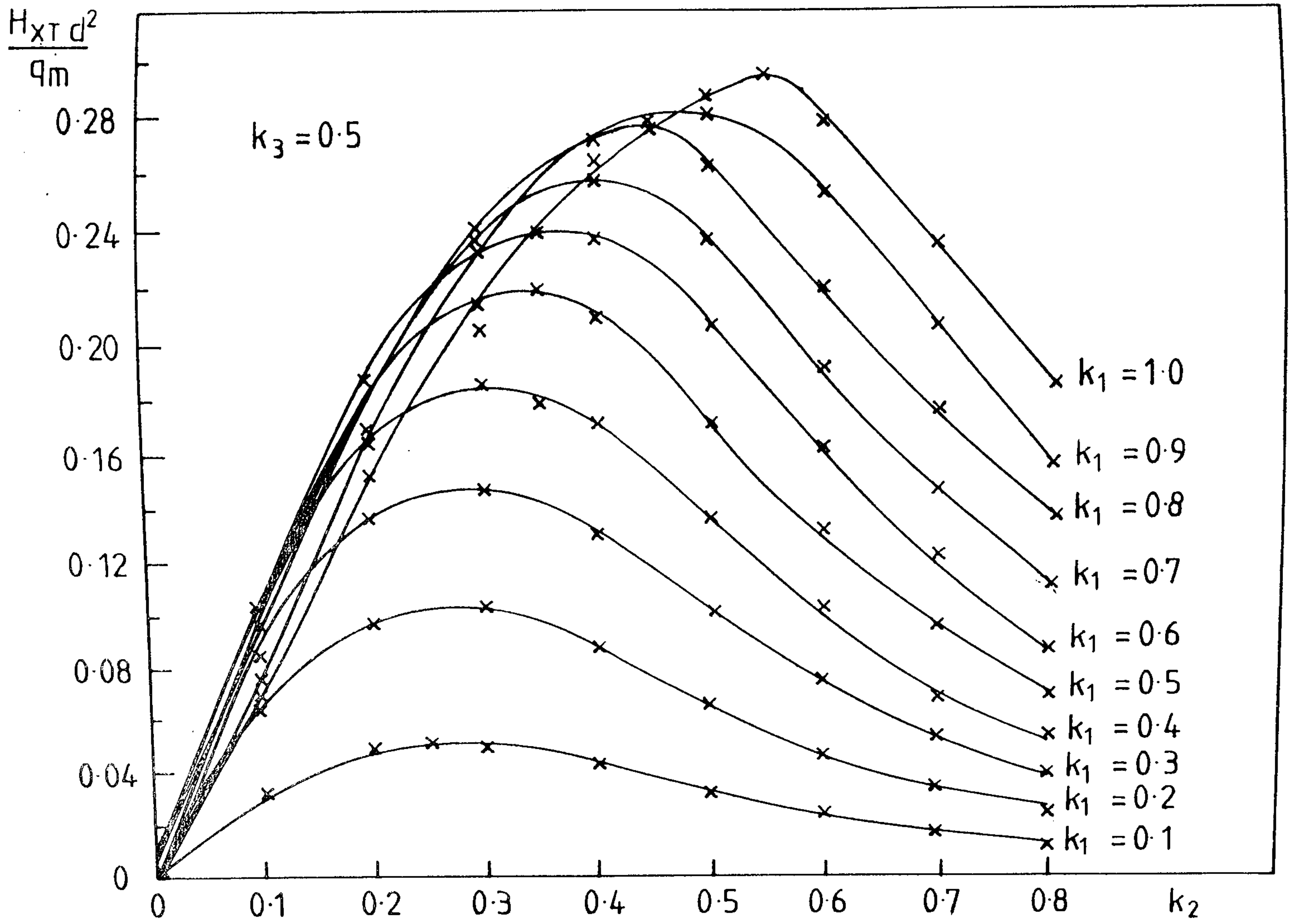

Fig 3.6 The distribution of the normalized field in the x direction produced by a vertical coil for different lengths of the core of the coil versus distance along the y-axis.

3.3 T-SHAPE CORE COIL

From the physical geometry of this coil and behaviour of the flux lines as shown in Fig. 3.7, it can be seen that the field is maximum along the axis of the coil as in the case of I-shape core coils. Also, from the physical shape of this geometry the overall reluctance of the magnetic path is less compared to the case of I-shape coils. The flux produced by the T-shape coils is therefore expected to be greater than that of I-shape coils for the same excitation current, number of turns and same material of the core, since:

$$\Phi = \frac{NI}{R} \tag{3.16}$$

where Φ = flux in Weber

NI = ampere-turn

R = reluctance of the magnetic path.

According to the above equation, if the R reduces, the flux produced will increase for the same ampere-turns. To determine the flux-distribution of complex problems such as the T-shape coil, either numerical analysis or analogy methods(30) are used. An electrical analogy method was therefore employed to calculate the field distribution of the T-shape coil. There are several different types of electrical analogues which may be used to calculate the field for such a problem(31,32). Among these analogues is the conducting paper analogy(33). This

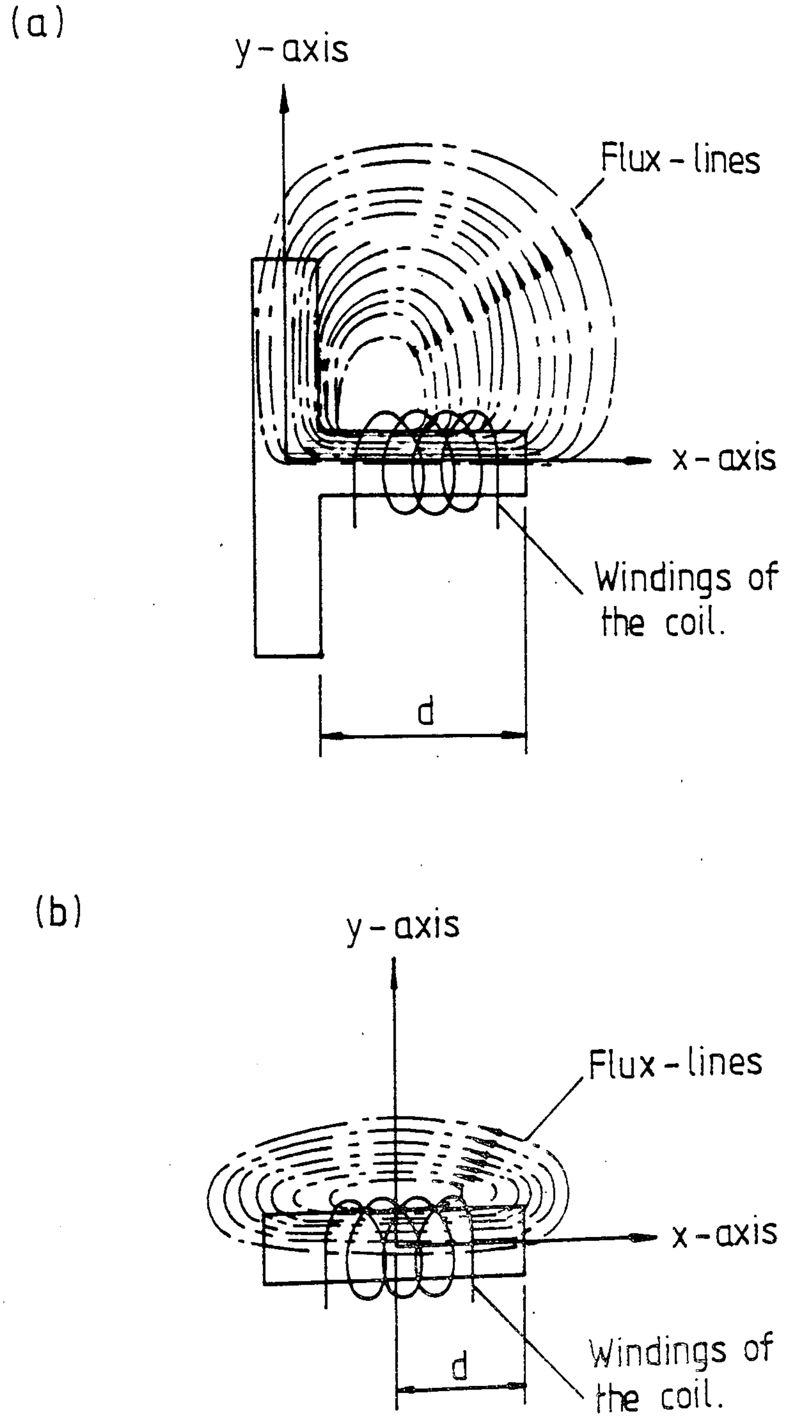

Fig 3.7 T and I shaped core coils.

technique can be used to determine the field in the plane of the source. However, it is impossible to determine the components of the field with this technique. Only the total field percentage can be determined at each point in the plane of the source. In order to compare between the fields produced by the T-shape and the I-shape coils, the field distribution of both geometries have been determined using conducting sheet paper.

Both geometries were cut from teledeltos paper using the same dimensional scale and the percentage of the flux density distribution of both geometries was determined at identical points on the paper. The measurement was carried out for both geometries for different values of y at x = d (d is as shown in Fig. 3.7). The results are given in Fig. 3.8. It is seen from these results that the T-shape coil has stronger flux than the I-shape coil at the identical points on the plane of the measurements. Also, the T-shape coil field is spread over a greater distance along the y-direction than for the I-shape core coil.

3.4 LOOP ELECTROMAGNETIC COILS

3.4.1 Square Loop with the Sides Parallel to the Co-ordinate Axes

If a loop is subjected to a time-varying current and the dimensions of the loop are very small compared to the wavelength, then the loop can be regarded as an equivalent

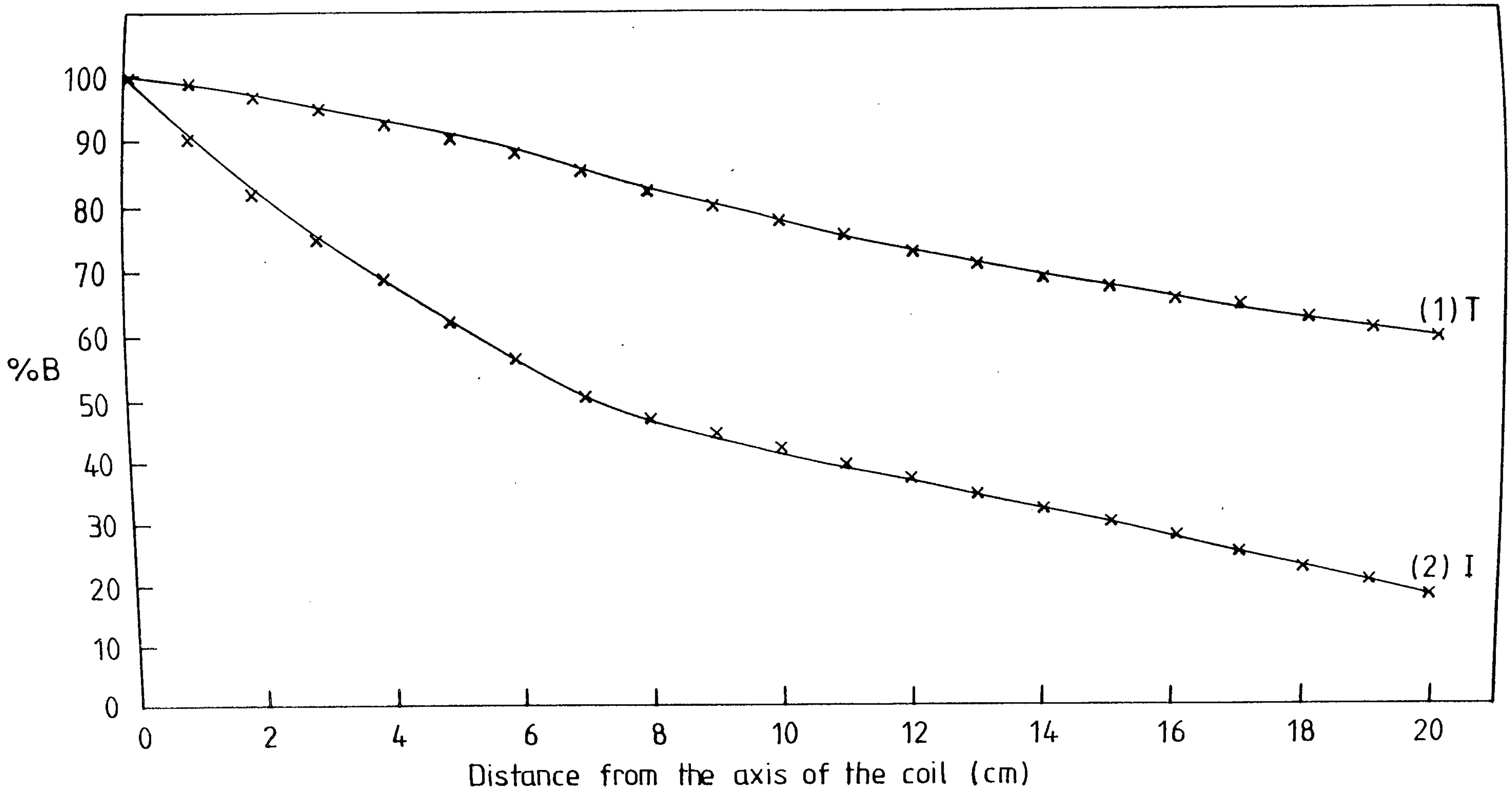

Fig 3.8 The percentage of the flux density for T and I shaped core-coils from the axes of the coils along a line perpendicular to the axis. (1) For T shaped coil, (2) For I shaped coil.

magnetic dipole (26,28). The magnetic field of the dipole at a point in space, where the distance between the point and dipole is larger compared to the dimensions of the loop, is given by equations (3.1) and (3.2). At ELF and VLF where the system may be regarded as quasi-static, the field can be found using equations (3.3) and (3.4). However, where the range at which the field to be calculated is comparable with the dimensions of the loop, equations (3.3) and (3.4) can not be employed to determine the field at the required points. If the quasi-static condition is prevalent, as is the case for the system considered in this work, the field equations in the near zone of the loop can be found using the Biot-Savart law (34,35).

Biot-Savart states that the magnetic field intensity for a current element, $\delta\ell$ at a point p, r metres distant from $\delta\ell$ is given by:

$$\overline{\delta H}_p = \frac{I}{4\pi}\left[\frac{\overline{\delta\ell}\times\overline{i}_r}{r^2}\right] \tag{3.17}$$

where $\overline{i}_r$ is the unit vector along r.

The magnitude of the field strength δH_p is

$$\delta H_p = \frac{I\delta\ell\sin\theta}{4\pi r^2}$$

where θ is the angle between r and $\delta\ell$.

The field due to a short wire as shown in Fig. 3.9 at an arbitrary point p using Biot-Savart is found to be (34,35):

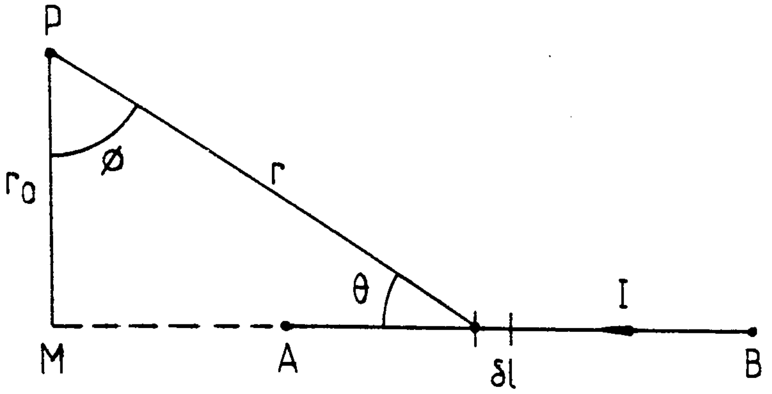

Fig 3.9 A geometry for the calculation of the field strength at point p due to a short wire AB carrying current I.

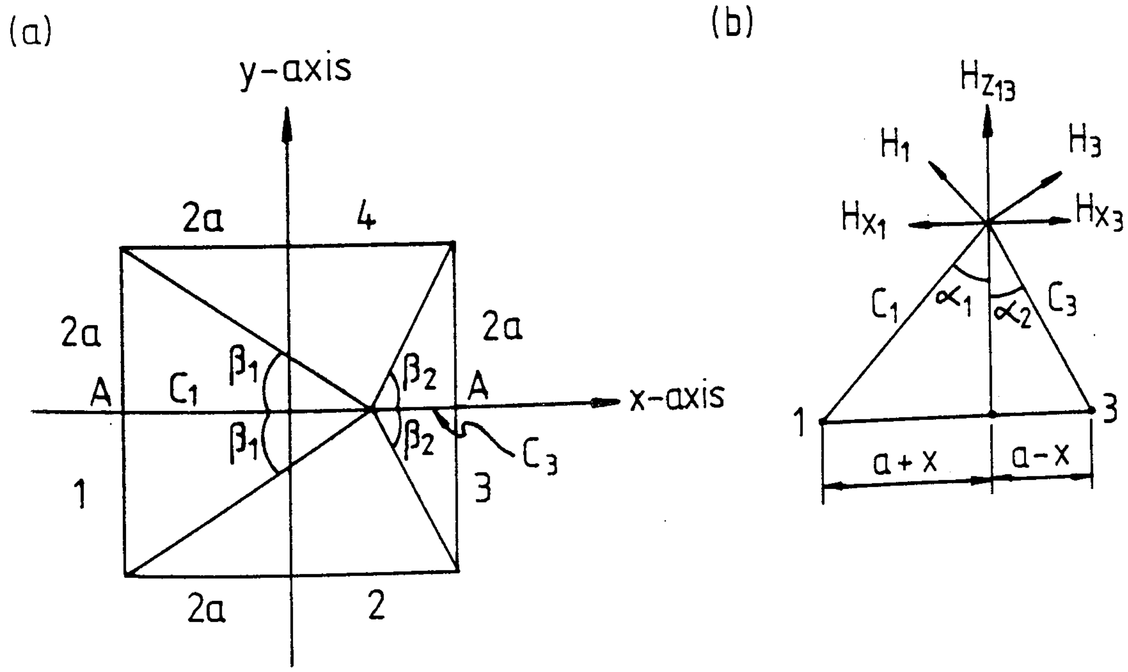

Fig 3.10 Square electromagnetic loop
(a) plane view (b) section AA.

$$H_p = \frac{I}{4\pi r_o} (\sin\beta - \sin\alpha) \qquad (3.18)$$

The angles β and α are the values of ϕ at the points A and B respectively. If M lies between A and B, either α or β must be taken as negative.

The square loop electromagnetic coil is built up of four straight pieces of such a wire. A plane view of a square loop and a section along the line AA are shown in Fig. 3.10.

In this geometry the x- and y-axes are taken to be in the plane of the loop and the z-axis perpendicular to the plane of the loop, pointing up out of the page.

The field generated by any side of the loop at an arbitrary point (p) may be found by direct application of equation (3.18). If, for simplicity, point p is taken on the x-z plane, then the field strength at p due to sides (1) and (3) of the loop is:

$$H_1 = \frac{I}{4\pi c_1} 2 \sin \beta_1 \qquad (3.19)$$

$$H_3 = \frac{I}{4\pi c_3} 2 \sin \beta_2 \qquad (3.20)$$

From Fig. 3.10 the field components in the x-direction at point p for sides (1) and (3) of the loop are:

$$H_{x1} = \frac{2I}{4\pi c_1} \sin \beta_1 \cos \alpha_1 \qquad (3.21)$$

$$H_{x3} = \frac{2I}{4\pi c_3} \sin \beta_2 \cos \alpha_2 \tag{3.22}$$

The resultant field component in the x-direction H_x is therefore given by:

$$H_x = \frac{Iaz}{2\pi} \left[\frac{1}{\left[z^2+(a-x)^2\right]\left[z^2+a^2+(a-x)^2\right]^{1/2}} - \frac{1}{\left[z^2+(a+x)^2\right]\left[z^2+a^2+(a+x)^2\right]^{1/2}} \right] \tag{3.23}$$

The loop sides (2) and (4) do not contribute to the x-component of the field.

The field in the y-direction H_y in x-z plane is zero. Following the same procedure in the y-z plane, H_y is given by:

$$H_y = \frac{Iaz}{2\pi} \left[\frac{1}{\left[z^2+(a-y)^2\right]\left[z^2+a^2+(a-y)^2\right]^{1/2}} - \frac{1}{\left[z^2+(a+y)^2\right]\left[z^2+a^2+(a+y)^2\right]^{1/2}} \right] \tag{3.24}$$

The field component H_y given in equation (3.24) is due to sides (2) and (4) of the loop, Sides (1) and (3) do not contribute to y-component of the field; H_x in this plane is zero.

To find the field in the z-direction H_z, the same procedure is used to find H_x and H_y. At any point in the space, H_z is given by:

$$H_z = \frac{Ia}{2\pi}\left[\frac{a-x}{[z^2+(a-x)^2][z^2+a^2+(a-x)^2]^{1/2}} + \frac{a+x}{[z^2+(a+x)^2][z^2+a^2+(a+x)^2]^{1/2}} + \frac{a-y}{[z^2+(a-y)^2][z^2+a^2+(a-y)^2]^{1/2}} + \frac{a+y}{[z^2+(a+y)^2][z^2+a^2+(a+y)^2]^{1/2}}\right] \quad (3.25)$$

The x-component of the field was calculated along the x-axis for different values of z and different areas of the loop. Fig. 3.11 shows the distribution of this component of the field at z = 0.2m. It can be seen from these graphs that the field strength is maximum near the conductors of the loop and reduces toward the centre to zero. The field strength in the x-direction at the other half of the loop by symmetry follows the same profile as that in the first half of the loop, but it is in the opposite direction. Also, it is apparent from Fig. 3.11 that this component of the field increases with increasing area of the loop. The field in the x-direction is also calculated along the z-axis for different values of x and areas of the loop. It is apparent from the results given in Fig. 3.12 that the field in the plane of the loop is zero and increases with increasing valuse of z until a

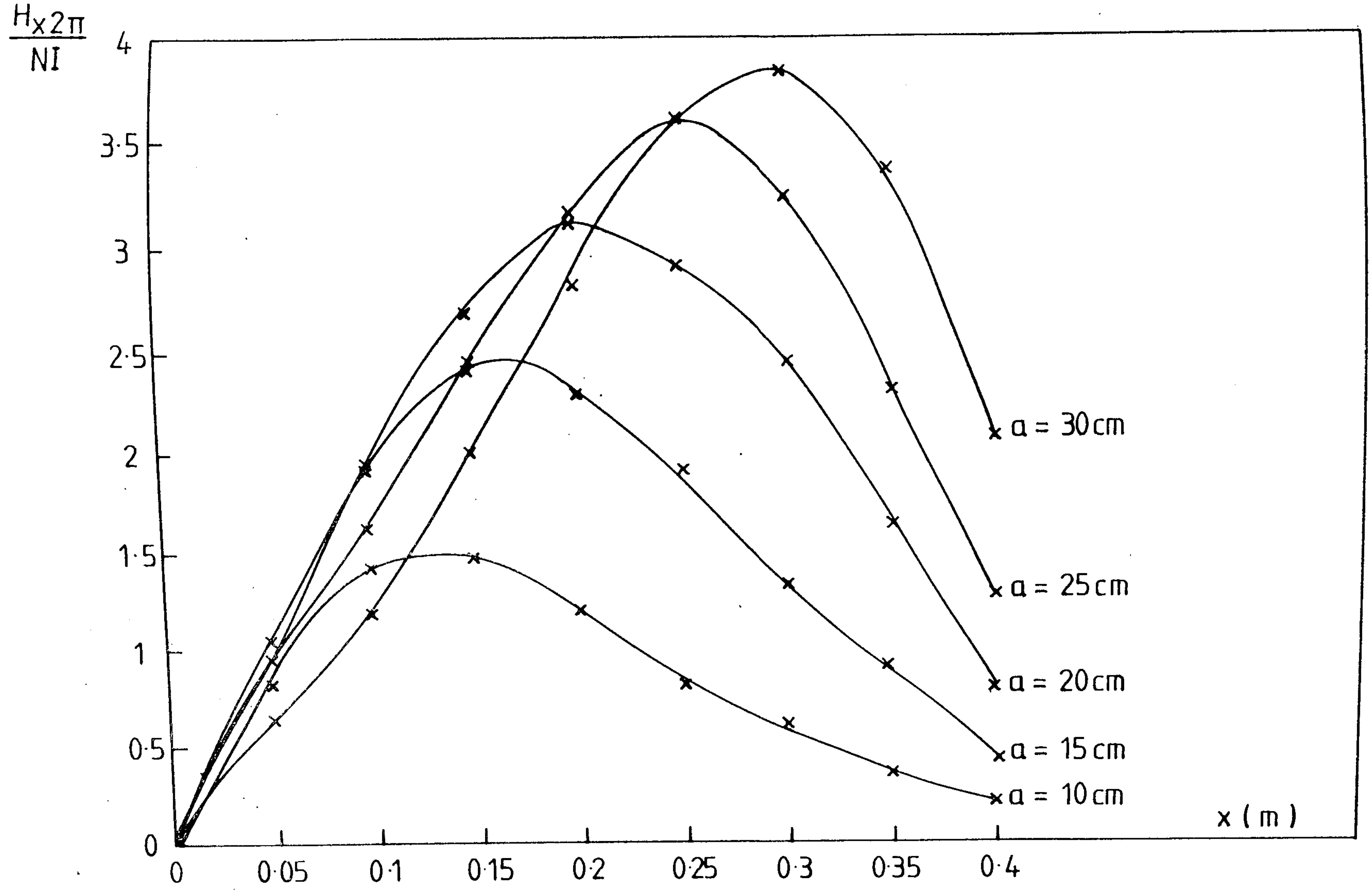

Fig 3.11 The normalized x component of the field for different dimensions of a square loop versus different distances along x-axis. The sides of the loop are parallel to x and y axes. The calculation is carried out at z = 0·2m.

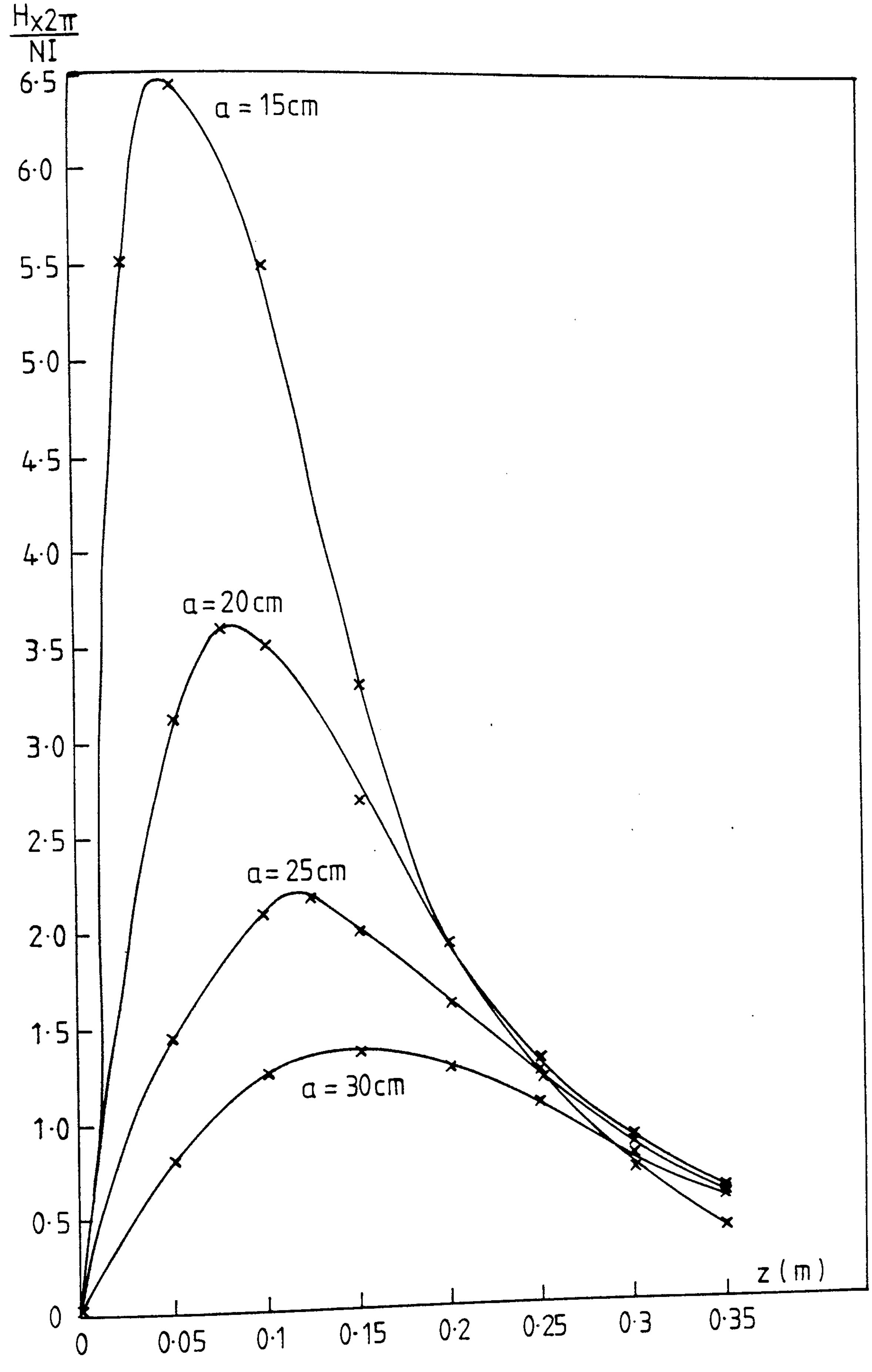

Fig 3.12 The normalized x component of the field at x = 0·1 m versus distances along z-axis for different dimensions of the square loop. The sides of the loop are parallel to x and y axes.

specific point is reached. After this point the field decreases along the z-axis for the same value of x. Also, it can be seen from Fig. 3.12 that the field strength decreases with increasing area of the loop for the same value of z.

3.4.2 Square Loop with the Diagonals Parallel to the Co-ordinate Axes

The field distribution equations in different directions for the square loop geometry with the diagonals coincident to the co-ordinate axes in the plane of the loop are found using a mathematical transformation of the field equations obtained for the geometry shown in Fig. 3.10. The square loop geometry with two systems of coordinate axes is given in Fig. 3.13. To obtain the field equation with respect to the new co-ordinate axes, the relation between the two co-ordinates system is derived as follows:

Let

$$u = x + jy = r\, e^{j(\theta+\pi/4)} \tag{3.26}$$

$$v = x' + jy' = r\, e^{j\theta} \tag{3.27}$$

then

$$\begin{aligned} x &= r\cos(\theta+\pi/4) \\ &= \frac{x'-y'}{\sqrt{2}} \end{aligned} \tag{3.28}$$

$$\begin{aligned} y &= r\sin(\theta+\pi/4) \\ &= \frac{x'+y'}{\sqrt{2}} \end{aligned} \tag{3.29}$$

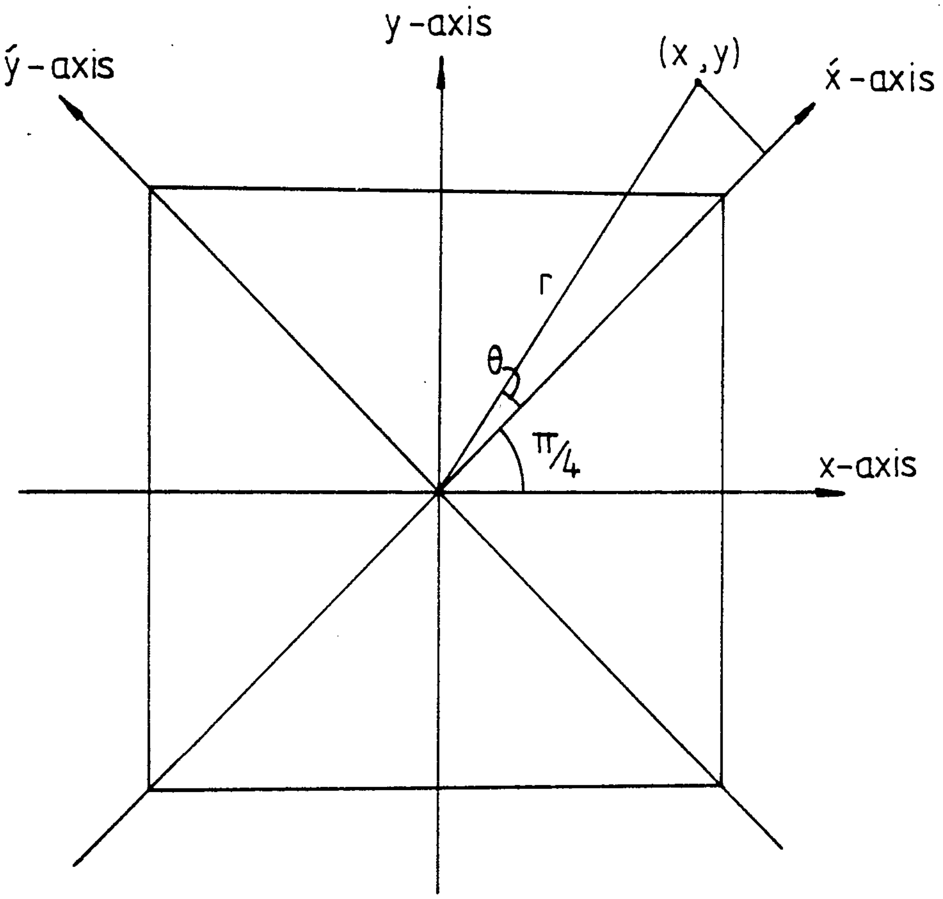

Fig 3.13 The square loop with both systems of coordinate axes.

All the parameters in the above equations are as shown in Fig. 3.13.

After establishing the relation between the two co-ordinate systems, the field components in the direction of the new co-ordinates can be derived as follows:

$$H_{x'} = \frac{H_x + H_y}{\sqrt{2}} \tag{3.30}$$

$$H_{y'} = \frac{H_y - H_x}{\sqrt{2}} \tag{3.31}$$

$$\begin{aligned} H_{x'} = \frac{Iaz}{2\sqrt{2}\pi} \Bigg[& \frac{1}{\left[\left(a-\frac{x'-y'}{\sqrt{2}}\right)^2+z^2\right]\left[a^2+\left(a-\frac{x'-y'}{\sqrt{2}}\right)^2+z^2\right]^{1/2}} \\ & - \frac{1}{\left[\left(a+\frac{x'-y'}{\sqrt{2}}\right)^2+z^2\right]\left[a^2+\left(a+\frac{x'-y'}{\sqrt{2}}\right)^2+z^2\right]^{1/2}} \\ & + \frac{1}{\left[\left(a-\frac{x'+y'}{\sqrt{2}}\right)^2+z^2\right]\left[a^2+\left(a-\frac{x'+y'}{\sqrt{2}}\right)^2+z^2\right]^{1/2}} \\ & - \frac{1}{\left[\left(a+\frac{x'+y'}{\sqrt{2}}\right)^2+z^2\right]\left[a^2+\left(a+\frac{x'+y'}{\sqrt{2}}\right)^2+z^2\right]^{1/2}} \Bigg] \end{aligned} \tag{3.32}$$

$$H_{y'} = \frac{Iaz}{2\sqrt{2}\pi}\left[\frac{1}{\left[\left(a-\frac{x'+y'}{\sqrt{2}}\right)^2+z^2\right]\left[a^2+\left(a-\frac{x'+y'}{\sqrt{2}}\right)^2+z^2\right]^{1/2}}\right.$$

$$-\frac{1}{\left[\left(a+\frac{x'+y'}{\sqrt{2}}\right)^2+z^2\right]\left[a^2+\left(a+\frac{x'+y'}{\sqrt{2}}\right)^2+z^2\right]^{1/2}}$$

$$-\frac{1}{\left[\left(a-\frac{x'-y'}{\sqrt{2}}\right)^2+z^2\right]\left[a^2+\left(a-\frac{x'-y'}{\sqrt{2}}\right)^2+z^2\right]^{1/2}}$$

$$\left.+\frac{1}{\left[\left(a+\frac{x'-y'}{\sqrt{2}}\right)^2+z^2\right]\left[a^2+\left(a+\frac{x'-y'}{\sqrt{2}}\right)^2+z^2\right]^{1/2}}\right] \qquad (3.33)$$

In the new co-ordinate system, the z'-axis is coincident with the z-axis in the original co-ordinate system and $H_{z'}$ in the new system is as follows:

$$H_{z'} = \frac{Ia}{2\pi}\left[\frac{a+\frac{x'-y'}{\sqrt{2}}}{\left[\left(a+\frac{x'-y'}{\sqrt{2}}\right)^2+z^2\right]\left[a^2+\left(a+\frac{x'-y'}{\sqrt{2}}\right)^2+z^2\right]^{1/2}}\right.$$

$$+\frac{a-\frac{x'-y'}{\sqrt{2}}}{\left[\left(a-\frac{x'-y'}{\sqrt{2}}\right)^2+z^2\right]\left[a^2+\left(a-\frac{x'-y'}{\sqrt{2}}\right)^2+z^2\right]^{1/2}}$$

$$+\frac{a+\frac{x'+y'}{\sqrt{2}}}{\left[\left(a+\frac{x'+y'}{\sqrt{2}}\right)^2+z^2\right]\left[a^2+\left(a+\frac{x'+y'}{\sqrt{2}}\right)^2+z^2\right]^{1/2}}$$

$$+\frac{a-\frac{x'+y'}{\sqrt{2}}}{\left[\left(a-\frac{x'+y'}{\sqrt{2}}\right)^2+z^2\right]\left[a^2+\left(a-\frac{x'+y'}{\sqrt{2}}\right)+z^2\right]^{1/2}}\Bigg] \qquad (3.34)$$

For simplicity, the field components were calculated only along the axes of the co-ordinates. The x'-component of the field was determined along the x'-axis for different values of z' and dimensions of the loop. Figure 3.14 shows the results of the calculation at z = 0.2m. It can be seen from these graphs that the field strength is maximum near the conductors of the loop and decreases toward the centre to zero. By symmetry on the other half of the loop, the field strength follows the same profile as that in the first half of the loop, but in the opposite direction. It was also found that this component of the field increases with increase of the loop area. The field strength $H_{y'}$ was also calculated along the y'-axis for different values of z' and sizes of the loop. These results are given as Fig. 3.15, for z' = 0.2m. From these graphs it can be seen that $H_{y'}$ along the y'-axis has the same profile as $H_{x'}$ along the x'-axis. The field component $H_{z'}$ has also been calculated along the x'-axis for various sizes of the loop. The results are shown in Fig. 3.16. It can be

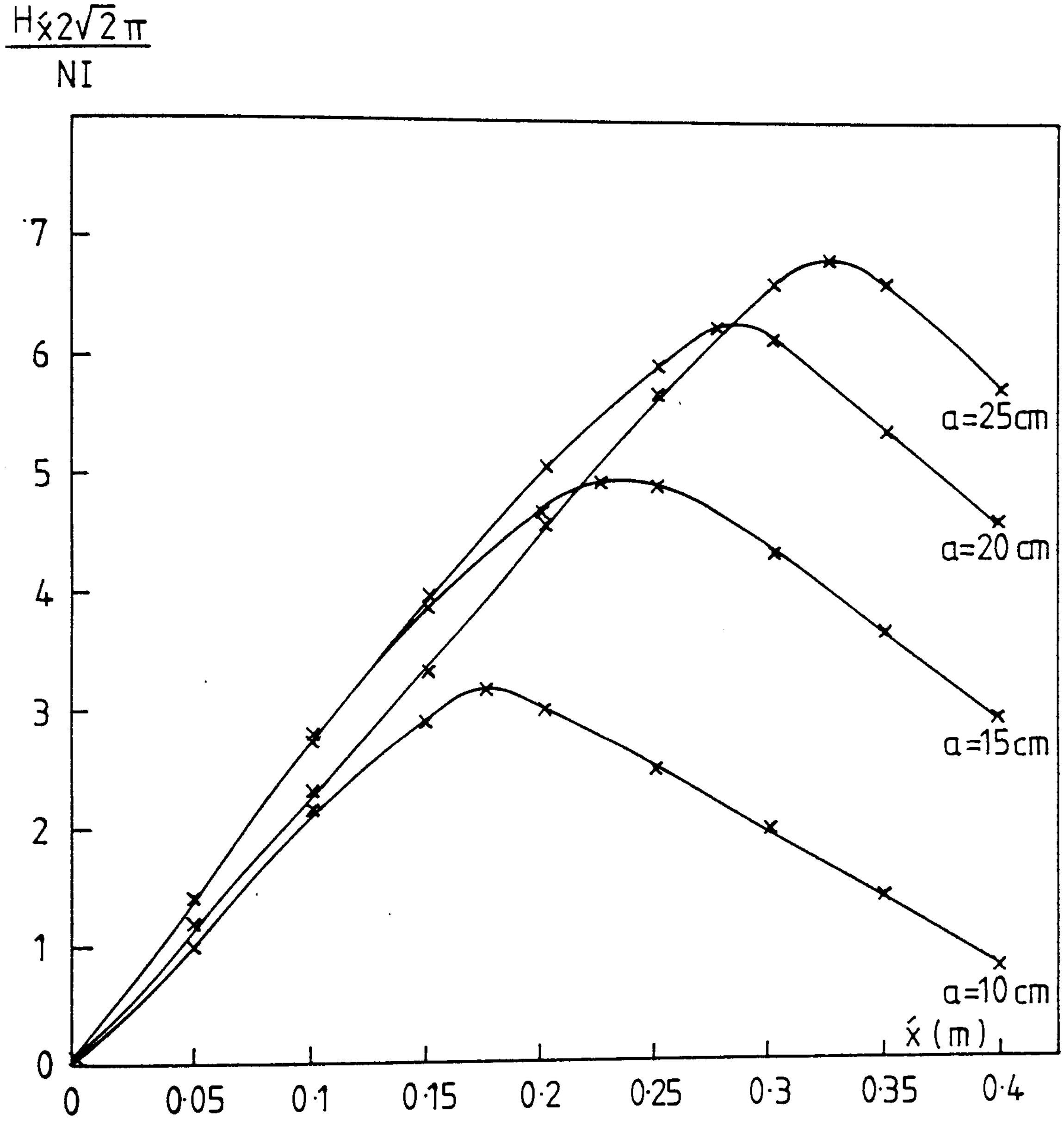

Fig 3.14 The normalized x́ component of the field at ź = 0·2m for different dimensions of the square loop versus different distances along x́-axis. The diagonals of the loop coincide with x́ and ý axes.

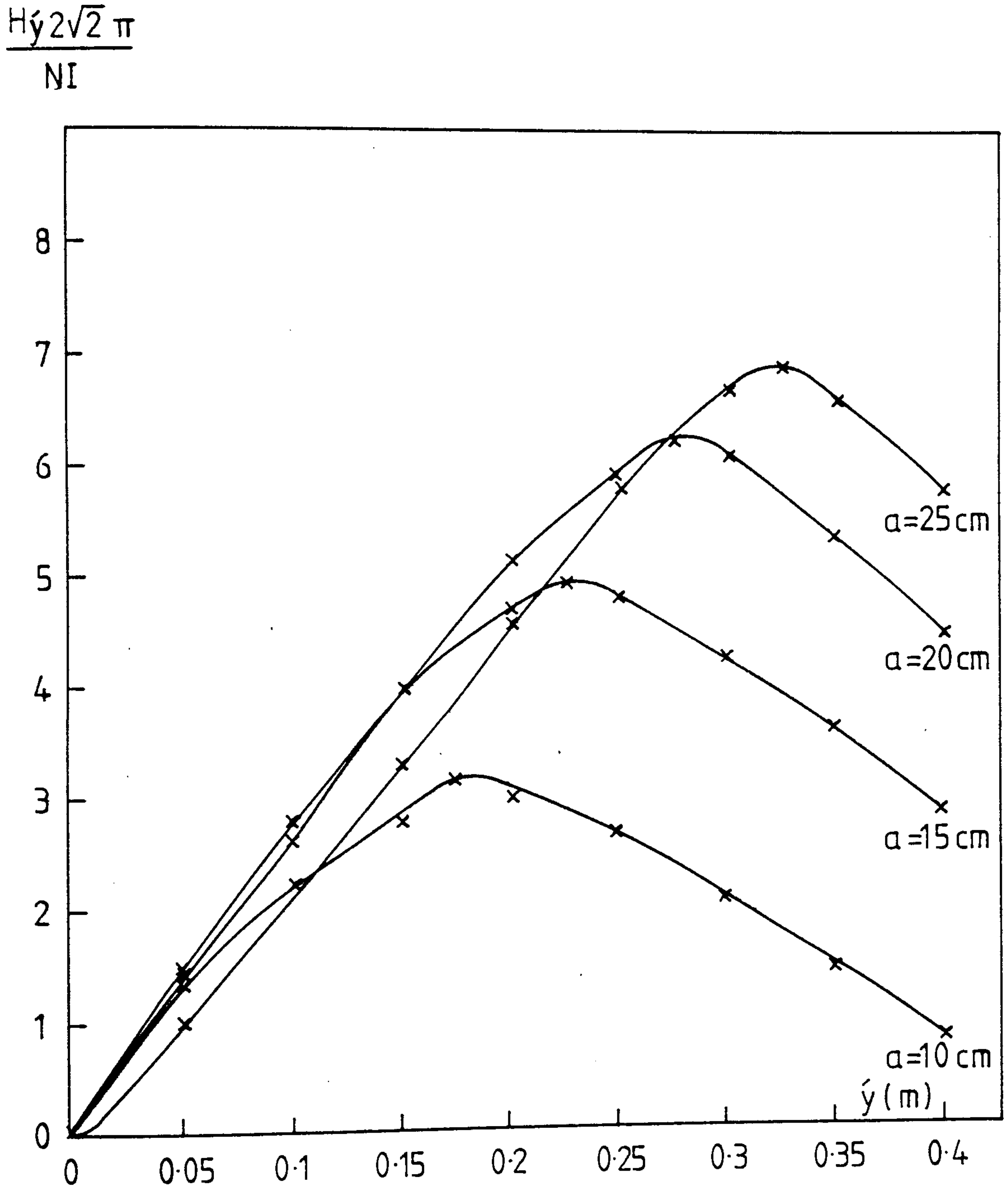

Fig 3.15 The normalized ý component of the field at ź=0·2 m for different dimensions of the square loop versus distances along ý-axis. The diagonals of the loop coincide with x́ and ý axes.

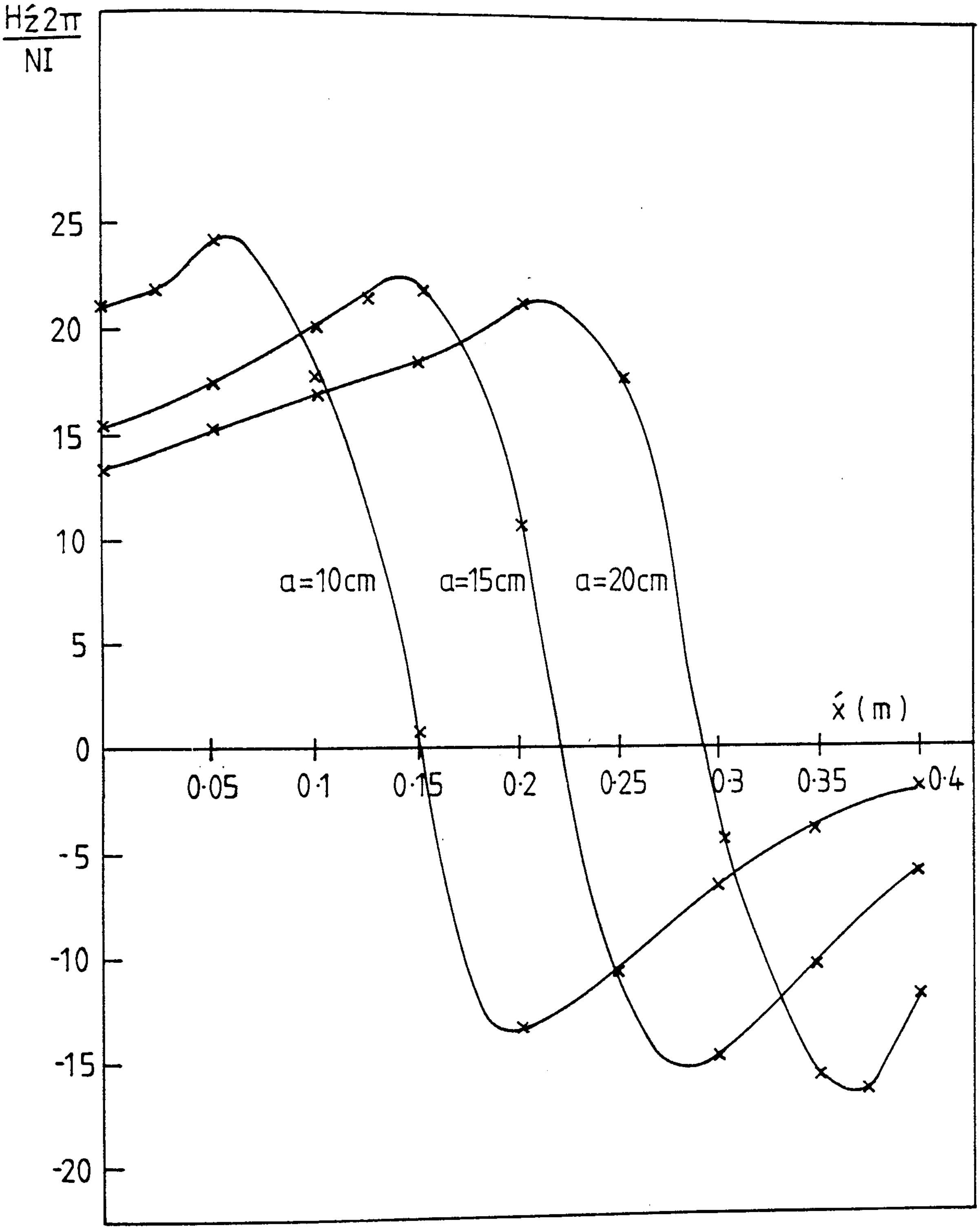

Fig 3.16 The normalized $\acute{z}$ component of the field at $\acute{z} = 5$ cm for different dimensions of the square loop versus different distances along $\acute{x}$ - axis. The diagonals of loop coincide with $\acute{x}$ and $\acute{y}$ axes

seen from these results that $H_{z'}$ is negative with high value outside the loop but near to the conductors, and positive high amplitude inside the loop and near to the conductors of the coil. In moving from the conductors towards the centre of the loop $H_{z'}$ decreases. On the other half of the loop, by symmetry $H_{z'}$ has the same distribution as in the first half of the loop.

3.5 COMPARISON OF THE FIELD DISTRIBUTIONS OF DIFFERENT SOURCE GEOMETRIES

Considering the I-shape core coils, the field distribution of the goemetry shown in Fig. 3.4.(a) extends over wider distances with greater magnitudes than the field distribution of the other I-shape geometries. In comparing the field of this geometry with field distribution of the T-shape core coil, it can be seen from the results shown in Fig. 3.8 that the T-shape coil has a stronger field and extends over wider distances than the I-shape coil.

In the case of the loop electromagnetic coil, the field distribution is well defined by the physical size of the loop as shown in Fig. 3.11. It is not possible to compare betweem the fields of the T-shape coil and the loop coil geometries by using theoretical analysis. However, there are many practical factors which have been taken into consideration in choosing the appropriate geometry of the coil for the purpose of this project and these are as follows:

(1) T-shape coils formed using transformer laminations, are suitable for use in the ELF range but not practicable in the VLF range.

(2) It is not practically possible to use transformer laminations or ferrite cores to form large loop coils.

(3) It is apparent from the field distributions of both geometries that the required size of the system to cover a specified width of conveyor belt using the T-shape coil is greater than that of the loop coil to cover the same width of belt. The larger size of the system reduces the accuracy of the detection, because the system becomes more susceptible to interference and noise than is the case for smaller sized systems.

(4) The location of the object on the width of the belt may be achieved using the loop electromagnetic coil. It is not possible using the T-shape coil.

The loop electromagnetic coil has been used in this work as a primary field source in both detectors. However, a practical comparison has been made in the case of the ferrous detector between the T-shape and the loop electromagnetic coils. The result of this comparison is given in Chapter 4.

3.6 ELECTROMAGNETIC FIELD PHENOMENA IN CONDUCTORS

3.6.1 General

When a conductor is subjected to an alternating magnetic field, the field penetrates into the conductor. The magnetic field at a point in the conductor is less than the field at the surface of the conductor. The reason of this is that the induced eddy-currents in the conductor themselves generate a magnetic field which opposes the inducing field. The main field and induced currents are therefore concentrated in a thin layer or skin near the surface. When a magnetic field penetrates into the conductor, it is not only attenuated in magnitude, but the phase of the field also changes. The effective depth to which the field penetrates into the conductor is called the penetration depth, which is the depth which would contain the whole flux at a density equal to the surface value. The penetration depth is a function of the material constants, conductivity and permeability, as well as the freqeuncy of the excitation.

It was found in the relevant literature that many authors(35,36,37,38,39) have studied the skin-effect in mangetic and non-magnetic conductors for different parameters such as electromagnetic field distribution, eddy-current distribution and surface impedance of the conductor. Most of the publications in the relevant literature solve Maxwell's equations analytically to determine the field distribution, eddy-current distribution and surface impedance of a plane conductor subjected to a one-dimensional field.

In most two- and three-dimensional problems, Maxwell's equations are solved numerically(40, 41) to calculate the field distribution and eddy-current distribution in the conductors.

Generally, the conductors may be classified as magnetically linear or non-linear conductors. In linear conductors the permeability is either equal to that of free space (non-ferrous conductors) or it has some value other than free space permeability, but is assumed to remain constant (ferrous conductors) with the change of the applied field strength (H). This assumption is applicable if the field strength employed is below the value at the knee-point of the B-H curve (Fig. 3.17). The constant permeability allows the magnetisation curve to be regarded as a straight line(38,42) as is the case in non-ferrous conductors. When the field strength has a magnitude greater than the field at the knee-point of the B-H curve, the permeability becomes the function of the applied magnetic field strength and hence the conductor must be regarded as a non-linear conductor.

However, the non-linear condition has been avoided in this work, because the field strength generated by the transmitting coil has been chosen so that it is not

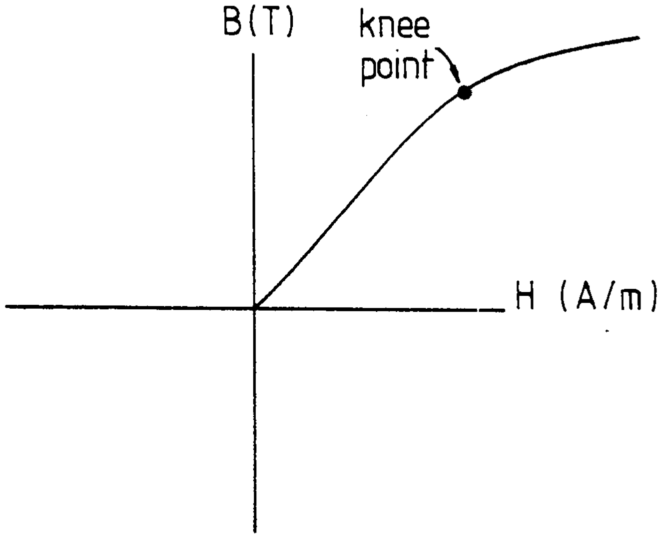

Fig 3.17 Normal B-H curve for ferrous metal.

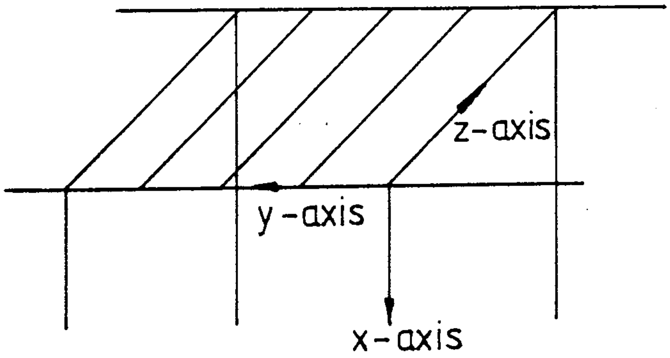

Fig 3.18 A plane solid conductor

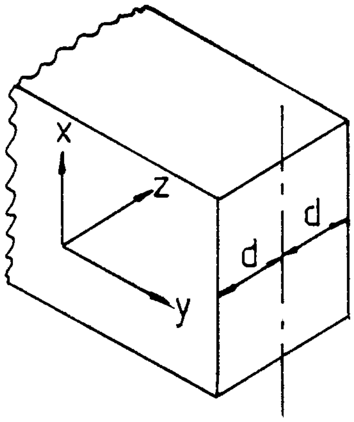

Fig 3.19 The plate of ferromagnetic material of thickness 2d.

strong enough to saturate the ferrous metal. This means the non-linear theory is not applicable to this work. The non-linear theory is therefore only described very briefly in section 3.6.3 of this thesis.

Maxwell's equations in general are given as (35,43):

$$\nabla\times\bar{E} = -\frac{\partial\bar{B}}{\partial t} \qquad (3.35)$$

$$\nabla\times\bar{H} = \bar{J} + \frac{\partial\bar{D}}{\partial t} \qquad (3.36)$$

$$\nabla.\bar{H} = 0 \qquad (3.37)$$

$$\nabla.\bar{D} = \rho \qquad (3.38)$$

where $\bar{E}$ = electric field vector
$\bar{H}$ = magnetic field strength vector
$\bar{B}$ = induction field vector
$\bar{D}$ = electric flux density vector
$\bar{J}$ = current density vector.
ρ = volum charge density

In addition, there is Ohm's Law, which may be taken as defining a conductor

$$\bar{J} = \sigma\bar{E} \qquad (3.39)$$

where σ is the conductivity of the conductor.

For good conductors, the displacement current may be regarded as negligible, then equation (3.36) becomes:

$$\nabla\times\bar{H} = \sigma\bar{E} \tag{3.40}$$

Taking the curl of both sides and using vector identity(43).

$$\nabla\times\nabla\times\bar{H} = \sigma\nabla\times\bar{E} \tag{3.41}$$

$$\nabla\times\nabla\times\bar{H} \equiv \nabla(\nabla.\bar{H}) - \nabla^2\bar{H} \tag{3.42}$$

Substituting values of $\nabla\times\bar{E}$ and $\nabla.\bar{H}$ from Maxwell's equations in the equation (3.42)

$$\nabla^2\bar{H} = \sigma\mu\frac{\partial\bar{H}}{\partial t} \tag{3.43}$$

where $\mu = \mu_o\mu_r$, μ_o = the permeability of free space, and μ_r is the relative permeability of the conductor.

The above equation may also be obtained in terms of $\bar{E}$ and $\bar{J}$

$$\nabla^2\bar{E} = \sigma\mu\frac{\partial\bar{E}}{\partial t} \tag{3.44}$$

$$\nabla^2\bar{J} = \sigma\mu\frac{\partial\bar{J}}{\partial t} \tag{3.45}$$

When all quantities are regarded as varying as $e^{j\omega t}$, the above equations may be written:

$$\nabla^2\bar{H} = j\omega\sigma\mu\bar{H} \tag{3.46}$$

$$\nabla^2\bar{E} = j\omega\sigma\mu\bar{E} \tag{3.47}$$

$$\nabla^2\bar{J} = j\omega\sigma\mu\bar{J} \tag{3.48}$$

These equations give the relation between the space and time derivatives of the magnetic field, electric field and current density at any point in the conductor.

3.6.2 Magnetically Linear Conductors

3.6.2.1 Magnetic Fields in Linear Conductors

If a plane conductor of infinite depth shown in Fig. 3.18 is subjected to a uniform sinusoidal magnetising force in the y-direction with no variation in the z-direction, the corresponding electric field and eddy-currents induced at the surface of the conductor are in the z-direction. The magnetic field distribution in the conductor is found by solving equation (3.46). Under the above conditions, equation (3.46) reduces to;

$$\frac{d^2H_y}{dx^2} = j\omega\mu\sigma H_y \tag{3.49}$$

A complete solution of this field distribution is in terms of exponentials(43)

$$H_y = H_o e^{-x/\delta} e^{-j(x/\delta)} \tag{3.50}$$

where H_o is the peak field strength at the surface of the conductor.

$\delta = \dfrac{1}{\sqrt{\pi f \mu \sigma}}$ = penetration depth of the conductor, and

x is the distance along the x-axis into the conductor.

In this form it is apparent that the magnitude of the magnetic field decreases exponentially with penetration into the conductor, and δ has the significance of the depth at which the field strength has decreased to 1/e of its value at the surface. The exponential decay of the field strength with the depth of penetration into the conductor is common in both ferrous and non-ferrous metals. In addition to this effect, the ferrous metal intensifies the magnitude of the induction field which enters the conductor, because of the high permeability of the ferrous metal.

The intensifying effect of the ferrous metal is used as a principle of detection in the design of the ferrous metal detector (Chapter 4).. It is also used in the ferrous and non-ferrous detector to discriminate between ferrous and non-ferrous metals.

3.6.2.2 Surface Impedance and Phase-Shift Calculations

The surface impedance of a conductor, which includes the resistance and internal reactance, may be found for the plane solid conductor shown in Fig. 3.18. The impedance is calculated for a unit length and unit width of the conductor. The surface impedance of the conductor per unit length is the quotient of the electric field at the surface and the total current in the conductor. The total current in the plane conductor is found by solving equation (3.45) to find the current density, then integrating it from the surface to the infinite depth. The current distribution equation (3.45) for the plane conductor shown in Fig. 3.18 becomes:

$$\frac{d^2 J_z}{dx^2} = j\omega\mu\sigma J_z \tag{3.51}$$

The solution of this equation in terms of exponential is

$$J_z = J_o\, e^{-x/\delta}\, e^{-j(x/\delta)} \tag{3.52}$$

where J_o is peak current density at the surface.

For a unit width, the total current is given by:

$$I_z = \int_o^\infty J_z dx = \int_o^\infty J_o\, e^{-(1+j)(x/\delta)} dx = \frac{J_o\,\delta}{(1+j)} \tag{3.53}$$

The electric field at the surface is given by the current density at the surface

$$E_{zo} = \frac{J_o}{\sigma} \tag{3.54}$$

The surface impedance for a unit length and unit width is then

$$Z_s = \frac{E_{zo}}{I_z} = \frac{(1+j)}{\sigma\delta} \tag{3.55}$$

For

$$Z_s = R_s + jx_s \tag{3.56}$$

where R_s = surface resistance.

x_s = surface reactance.

Then

$$R_s = \frac{1}{\sigma\delta} = \sqrt{\frac{\pi f \mu}{\sigma}} \qquad (3.57)$$

$$x_s = \frac{1}{\sigma\delta} = R_s \qquad (3.58)$$

The resistance and reactance of such a plane conductor are equal at any frequency. The surface impedance Z_s thus has always a phase angle of 45°. This impedance is calculated for a unit length and unit width of the plane conductor. For a finite area of conductor the impedance is obtained by multiplying Z_s by the length and dividing by the width. Equation (3.55) may also be used to calculate the surface impedances of conductors of other than plane shape, since it may be thought of as a constant of the material at a given frequency.

3.6.2.3 Power Flow into the Conductor

The power loss for a unit area of the plane conductor may be found by multiplying the surface resistance R_s calculated in the previous section by the square of the current per unit width I_z.

$$P_A = \frac{1}{2} R_s |I_z|^2 \qquad (3.59)$$

The reactive power flow in a unit area of the conductor is determined by multiplying the surface reactance x_s to the square of the magnitude of the current per unit width I_z.

$$P_R = \frac{1}{2} x_s |I_z|^2 \tag{3.60}$$

The current per unit width of the conductor is related to the magnetic field strength by (37,43):

$$\bar{I} = \bar{n}\times\bar{H} \tag{3.61}$$

where $\bar{n}$ is a unit vector perpendicular to the conductor surface and $\bar{H}$ is the magnetic field at the surface. Using the above relation and taking the surface value of H_y in Fig. 3.18 as H_o, then I_z in the equations (3.59) and (3.60) may be substituted by H_o and they then become:

$$P_A = \frac{1}{2} R_s |H_o|^2 \tag{3.62}$$

$$P_R = \frac{1}{2} x_s |H_o|^2 \tag{3.63}$$

3.6.3 Magnetically Non-linear Conductor

If a ferromagnetic material is subjected to a uniform alternating magnetizing force, with the magnitude of this field at the surface of the material H_o greater than the magnitude of the field strength at the knee-point of the B-H curve, then the relation between B and H becomes non-linear (i.e. the permeability of the material varies with H). The analysis presented in the last section for linear conductors is therefore no longer applicable.

Several authors (36,37,38,39) have considered the field distribution, current distribution and loss density in ferromagnetic materials. Agarwal$^{(37)}$ has employed a rectangular B-H curve assumption in his calculations for non-linear conductors. He derived his equations for a block of ferromagnetic material with thickness of 2d and infinite length. The conductor is subjected to a sinusoidal magnetic field in the y-direction with no variation in the x-direction. The geometry of the conductor is shown in Fig. 3.19.

Agarwal's equations are given below;

The surface impedance

$$Z_s = \frac{16}{3\pi\sigma\delta} \cdot \left[\left\{1-\left(1-\frac{d^2}{\delta^2}\right)^{3/2}\right\} + \frac{j}{2}\left(\frac{3d}{\delta} - 2\frac{d^3}{\delta^3}\right)\right] \tag{3.64}$$

where σ is the conductivity of the conductor,

δ is the penetration depth into the conductor.

The phase angle θ of the surface impedance

$$\theta = \tan^{-1} \frac{3\frac{d}{\delta} - 2\left(\frac{d}{\delta}\right)^3}{2\left[1-\left(1-\frac{d^2}{\delta^2}\right)^{3/2}\right]} \tag{3.65}$$

The active power loss per unit area P_A is given by

$$P_A = \frac{8}{3\pi} \cdot \frac{H_m^2}{\sigma\delta}\left[1-\left(1-\frac{d^2}{\delta^2}\right)^{3/2}\right] \tag{3.66}$$

where H_m is the peak value of the magnetising force at the surface

$$P_R = \frac{4H_m^2}{3\pi\sigma\delta}\left(3\frac{d}{\delta} - 2\frac{d^3}{\delta^{3/2}}\right) \tag{3.67}$$

When the half thickness of the plate is equal or greater than the depth of penetration, then

$$Z_s = \frac{16}{3\pi\sigma\delta}\left[1 + \frac{j}{2}\right] \tag{3.68}$$

$$\theta = \tan^{-1}\frac{1}{2} \tag{3.69}$$

$$P_A = \frac{8}{3\pi} \cdot \frac{H_m^2}{\sigma\delta} \tag{3.70}$$

$$P_R = \frac{4}{3} \quad \frac{H_m^2}{\sigma\delta} \tag{3.71}$$

Most recent publications use Agarwal's theory as a basis for the analysis of non-linear problems.

3.7 SUMMARY

The field distributions at different points in space for various source geometries have been determined. The results have been discussed and compared to enable a choice of the appropriate size and geometry of the coil to be made for the purpose of this project. Electromagnetic field distribution, induced current distribution, surface impedance and active and reactive power flow equations in the conductor have been obtained for both linear and non-linear conductors. The difference between magnetically linear and non-linear conductors has also been outlined briefly in this chapter.

Chapter Four

Development of the ferrous metal detector using flux-gate magnetometer

4.1 INTRODUCTION

It has been mentioned earlier in this thesis that the proposal was to use the flux-gate magnetometer for sensing the presence of metallic objects in the materials carried on conveying systems. The flux-gate magnetometer can only detect ferrous metal objects. A detector using a flux-gate magnetometer was developed, however, because of its application for the detection of tramp iron in conveyed commodities such as the coal used for firing the generating units of power stations(44).

The equipment was designed to be used in the power station environment. The application of the detector in the power station is described in more detail in section 4.7.

In this system the flux-gate magnetometer was placed in the field of the transmitting coil such that there was no output from the flux-gate if there was no tramp iron within the detection range of the system. When a ferrous object enters the zone of the equipment, it enhances the field intensity without affecting the field phase. This is fully discussed later in section 4.3. The flux-gate detects this enhancement and gives an output which is then processed electronically to indicate the presence of the ferrous object. The flux-gate was used as a sensor in conjunction with an a.c. exciting field. In this way the effect of the earth's magnetic field could be eliminated. This also increases the sensitivity of the detector because the flux-gate now operates about the centre of its characteristic.

This chapter describes the theoretical and practical development of the ferrous detector using the flux-gate magnetometer. The practical application of the equipment in the power station, together with experimental tests on the system, are also included in the chapter.

4.2 BACKGROUND OF THE FLUX-GATE MAGNETOMETER

4.2.1 A Brief Review on the Flux-gate Magnetometer

The flux-gate magnetometer is a device for measuring magnetic fields. It derives its detection capability from the non-linear characteristic of ferromagnetic core material. The flux-gate magnetometer is a directional device and therefore only measures the component of the field parallel to the sensing coil (45).

Flux-gates were first designed in the early 1930s and have had particular application in defence work. The so called MAD detector (magnetic airborne detection) was widely used in the second world war. When carried in an aircraft the magnetometer was capable of detecting the small field changes resulting from submarines. They became increasingly used in many different branches of science. Flux-gate magnetometers are popular because of their reliability, relative simplicity, low cost, low powerconsumption, high sensitivity, stability, wide measurement range and small size. The flux-gate magnetometer has found applications in magnetic field measurements of outer space(15) and in all forms of geophysical surveys(46). A precision flux-gate magnetometer has been included in a recently launched scientific survey satellite in order to map the earth's magnetic field(16). This satellite gathers a complete picture of the earth's field every 12 hours. As well as geophysical applications it has also been used in medical measurements(12). A low power flux-gate magnetometer has been especially designed for vehicle detection purposes(6).

4.2.2 The Principles of Operation of the Flux-gate Magnetometer

The flux-gate action is based upon variations of core permeability obtained by cyclically driving the core into its saturation zone. When the core is in saturation the permeability decreases. Fig. 4.1 shows a typical magnetisation curve for a ferromagnetic material commonly used in flux-gate magnetometer cores.

A primary coil is wound on the core of the flux-gate magnetometer into which an a.c. signal is fed. This primary coil sets up an oscillating magnetic field which produces the cyclic saturation of the core. The flux density in the core is given by:

$$B = \mu_o \mu_r H \tag{4.1}$$

where B is the magnetic flux density (Tesla)

H is the magnetic field strength (A/m)

μ_o is the permeability of free space (H/m)

μ_r is the relative permeability of the core.

The relative permeability μ_r of the core changes cyclically with time, since the alternating magnetic field drives the core of the flux-gate cyclically into saturation, as shown in Fig. 4.1. The core flux density B is related to the external flux density B_{ex}:

$$B = \mu_a B_{ex} \tag{4.2}$$

where μ_a is the apparent or effective core permeability and is dependent upon the core material and its physical configuration.

The apparent permeability μ_a and relative permeability μ_r are related as below:

$$\mu_a = \frac{\mu_r}{1+D(\mu_r-1)} \tag{4.3}$$

where D is the demagnetising factor of the core.

The secondary coil is wound around the core and primary windings. Because the permeability of the core changes with time, the flux in the core changes and a voltage is induced in the secondary coil. If two opposing magnetised cores are placed inside the same secondary, the only resultant flux change is that which

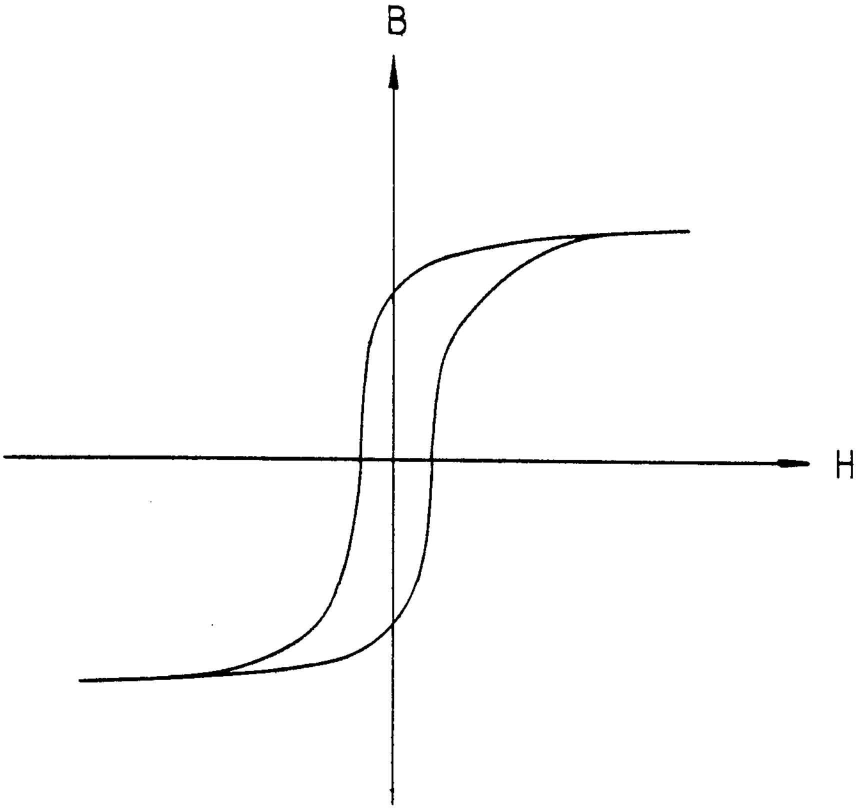

Fig 4.1 A magnetization curve for a typical flux-gate core material.

is caused either from a change in the external field or by a change of relative core permeability, μ_r. All other components cancel out because the primaries of the ring core flux-gate magnetometer are connected in series opposition.

The output voltage V_o of the flux-gate magnetometer is:

$$V_o = nA \frac{dB}{dt} \tag{4.4}$$

where n = number of turns of the secondary

A = cross sectional area of the core (m^2).

$$V_o = nAB_{ex} \frac{d\mu_a}{dt} \tag{4.5}$$

and

$$\frac{d\mu_a}{dt} = \frac{d}{dt} \left[\frac{\mu_r}{1+D(\mu_r-1)}\right] \tag{4.6}$$

then

$$V_o = \frac{nAB_{ex}(1-D) \frac{d\mu_r}{dt}}{\left[1+D(\mu_r-1)\right]^2} \tag{4.7}$$

The above equation gives the output voltage of the flux-gate for an external field B_{ex}.

The flux-gate magnetometer used in this work is a ring core parallel flux-gate. It detects only the component of the external field in the direction of the sensor axis.

The detailed principle of operation of this flux-gate is described in Reference (45).

4.3 THEORY OF OPERATION OF THE FERROUS DETECTOR

An a.c. electromagnetic field was generated by an appropriate field source. The flux-gate was situated within this field such that it was balanced against the component of the field parallel to its axis.

The shape of the coil used as a field source in this work was the loop electromagnetic coil.
The geometry of the loop with the flux-gate is shown in Fig. 4.2. In this geometry the only component of the field which is detected by the flux-gate is the x-component of the field. From the theoretical calculations given in Chapter 3, the horizontal components of the field at each half of the loop with respect to the flux-gate are equal and opposite at the corresponding point. This means that if the flux-gate is placed as shown in Fig. 4.2, the net field reaching it is zero and it therefore gives no output. In the actual application of the detector to the detection of ferrous objects in coal conveyors, the conveyed material is passed between the loop and flux-gate magnetometer, because this increases the sensitivity and the range of detection. The reason for this is discussed in section 4.4.2.

If a ferrous metal object enters the detection zone of the system, it intensifies the field of the corresponding

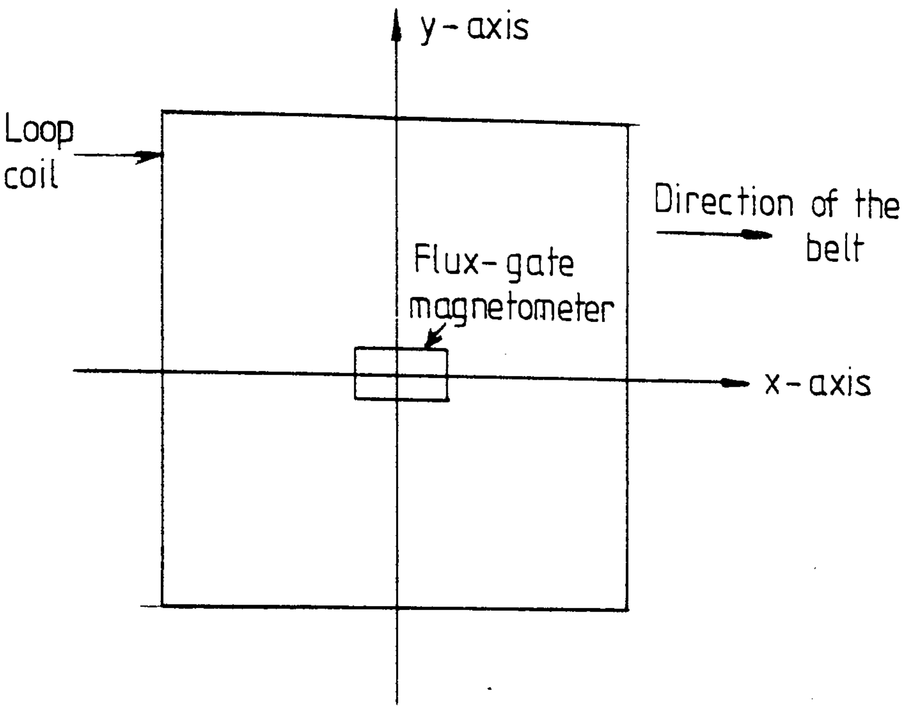

Fig 4.2 The geometry of the loop electromagnetic coil and flux-gate magnetometer

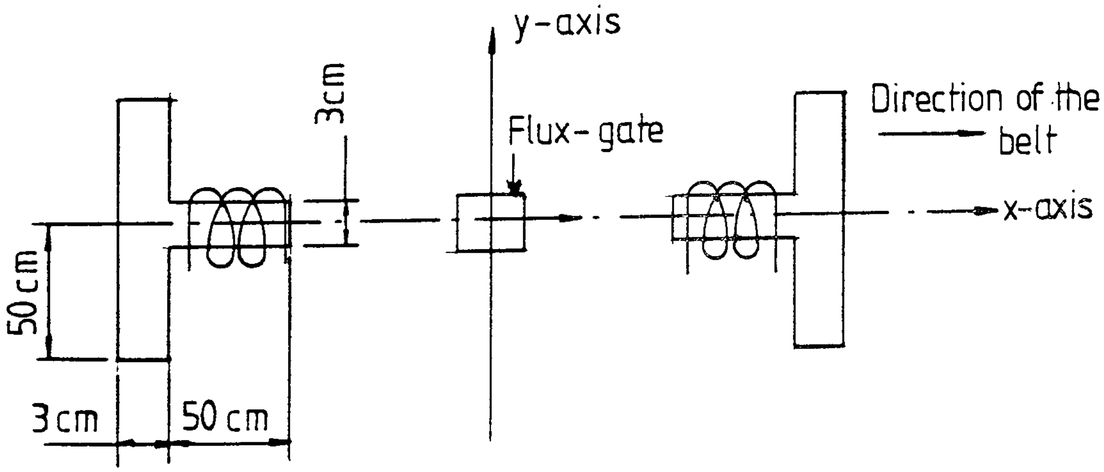

Fig 4.3 The geometry of the system using T shape core coils.

side of the zone because of the high permeability of the ferrous object. The flux-gate then detects the intensifying effect and gives an output voltage. The amplitude of the output is proportional to the magnitude of the parallel external field (equation (4.7)) which results from the ferrous metal object. The eddy-currents produced in the metal are negligible since the excitation frequency is kept low (section 4.5). The intensifying of the field is therefore the predominant effect in this detector. The detector using this flux-gate cannot therefore be used for the detection of non-ferrous objects. The intensifying effect is proportional to the size of the object and its position with respect to the field source and the flux-gate.

It is far too complex a problem to calculate analytically the output of the flux-gate due to the presence of a ferrous object within the detection zone of the system. The output can, however, be computed using numerical analysis. Since the main objective of the present work was the pratical development of the equipment the numerical analysis was considered outside the scope of this work and therefore not attempted. However, practical measurements of the output of the flux-gate were made for given sizes of the object at different points within the detection zone of the system along the direction of the belt, (i.e. parallel to the axis of the flux-gate) and across the width of the belt.

The output from the flux-gate may be electronically processed to indicate the presence of ferrous objects.

The flux-gate magnetometer detects the earth's field and gives an output proportional to it. The effect of the earth's field was eliminated by employing a feedback control circuit in conjunction with an a.c. excitation field. The detailed design and construction of the control system is given in section 4.6.

4.4 PRACTICAL DEVELOPMENT OF THE FIELD GENERATING SOURCES

The excitation electromagnetic field was generated by driving an electromagnetic coil with an a.c. current. The near-zone field produced by the coil for a given current, number of turns and core material is a function of the geometry and size of the coil. From the geometries studied in Chapter 3, it was concluded that the T-shape core coil has a stronger field distribution than the I-shape core coils. It is impossible, however, to make a theoretical comparison between T-shape core coils and loop electromagnetic coils.

It was finally decided to use a loop coil as a field generating source because of the smaller physical size of the system than can be achieved using the T-shape coil. However, both shapes have been developed practically from the theoretical basis given in Chapter 3. The output of the system for both field sources has been measured and compared for a given size of ferrous object at different points within the detection zone of the system.

4.4.1 The T-shape Core Coil

For complete detection of all ferrous objects on a conveyor belt it is necessary for the electromagnetic field produced by the field source to extend over the complete width of the belt. From the calculation given in section 3.4, it is possible to design any size of T-shape coil to cover the required detection range of the equipment.

The geometry of the system using the T-shape field source is shown in Fig. 4.3. The T-shape coils were formed from transformer laminations. The high permeability core material increases the flux produced by the coil for a given number of amp-turns. The dimensions of the coils constructed are as shown in Fig. 4.3. Coils consisting of 200 turns of SWG16 copper enamel wire were wound on each T-shape core. An electromagnetic field is produced when a current is passed through the coils. The net flux on the flux-gate magnetometer is zero, since the fields produced by the two coils are equal and opposite. If a ferrous metal enters the field, the balance is disturbed and the flux-gate detects the enhancement produced by the object and gives an output voltage which is then processed to indicate the presence of the object.

The output of the phase-sensitive detector (section 4.5) has been measured for different distances of the ferrous object (1×3×5 cm) from the axis of the coil along the y-axis at mid-distance between the coil and flux-gate. The measurement was carried out for different horizontal distances of the flux-gate from the coils. The results of the measurements are shown in Figs. 4.4, 4.5 and 4.6. The measurements were taken with the transmitting coils and flux-gate situated in two parallel planes, since this increases the sensitivity of the system. The distance between the plane of the coils and flux-gate was maintained at about 30 cm during the measurement, this being the typical depth of the coal on the conveying system of the power station.

From the results shown in Figs. 4.4, 4.5 and 4.6, the output is maximum on the axis of the coil and reduces with the distance along the y-axis for all the horizontal distances considered here between the flux-gate and coils. It can also be seen from the results that the detection range of the equipment is a function of the horizontal distance for a fixed vertical distance between the coils and flux-gate. For a specified belt area, the length of the core of the coil and horizontal distance between the coils and flux-gate adjusted (for a fixed vertical distance) to cover the required detection range for a given current and number of turns of the coil can thus be selected.

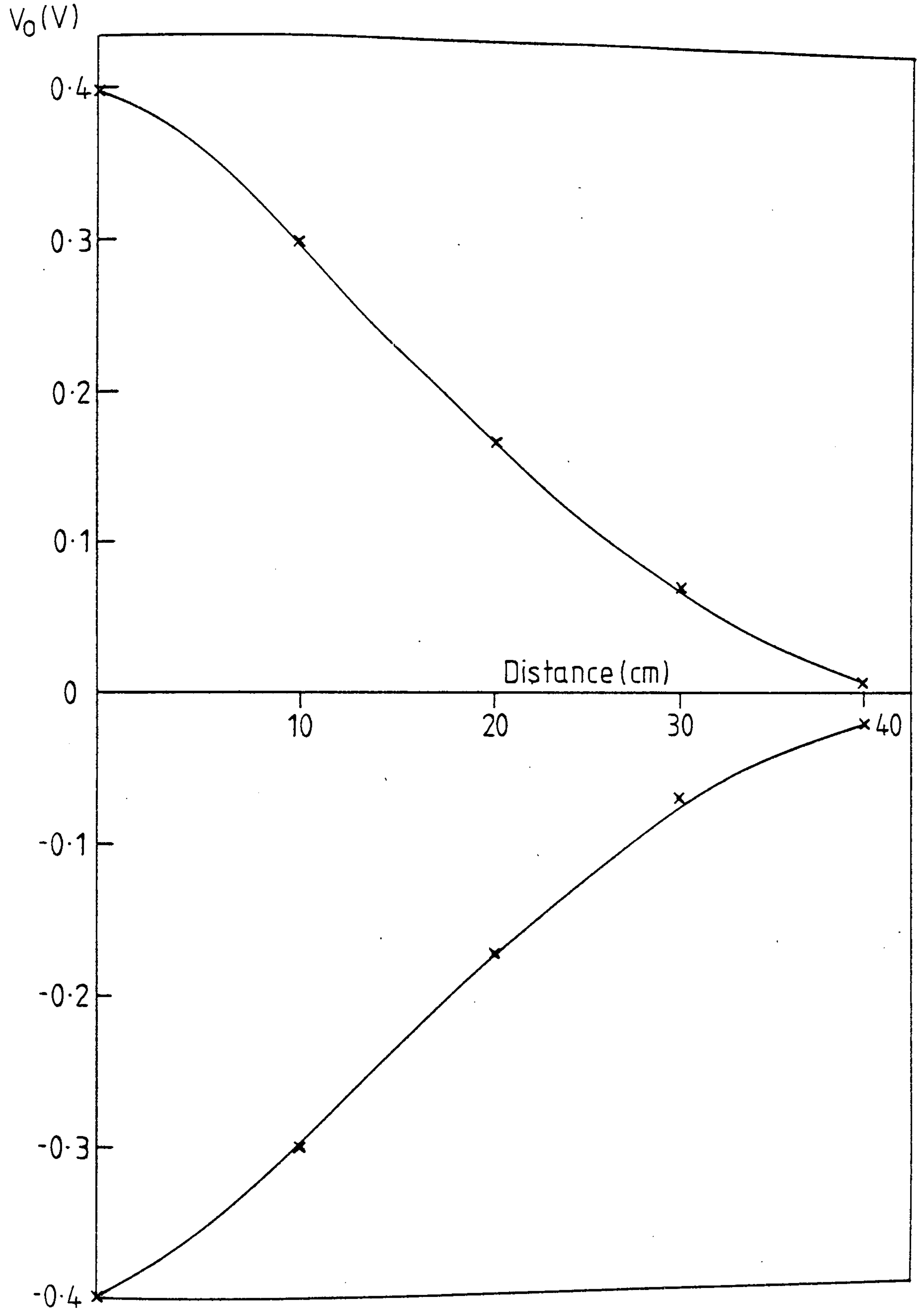

Fig 4.4 The output of the p.s.d. against distance along a line parallel to y-axis for object size (1×3×5 cm) Using T shape excitation coil, 200 turns, 1A current and 0·75m between the flux-gate and coils.

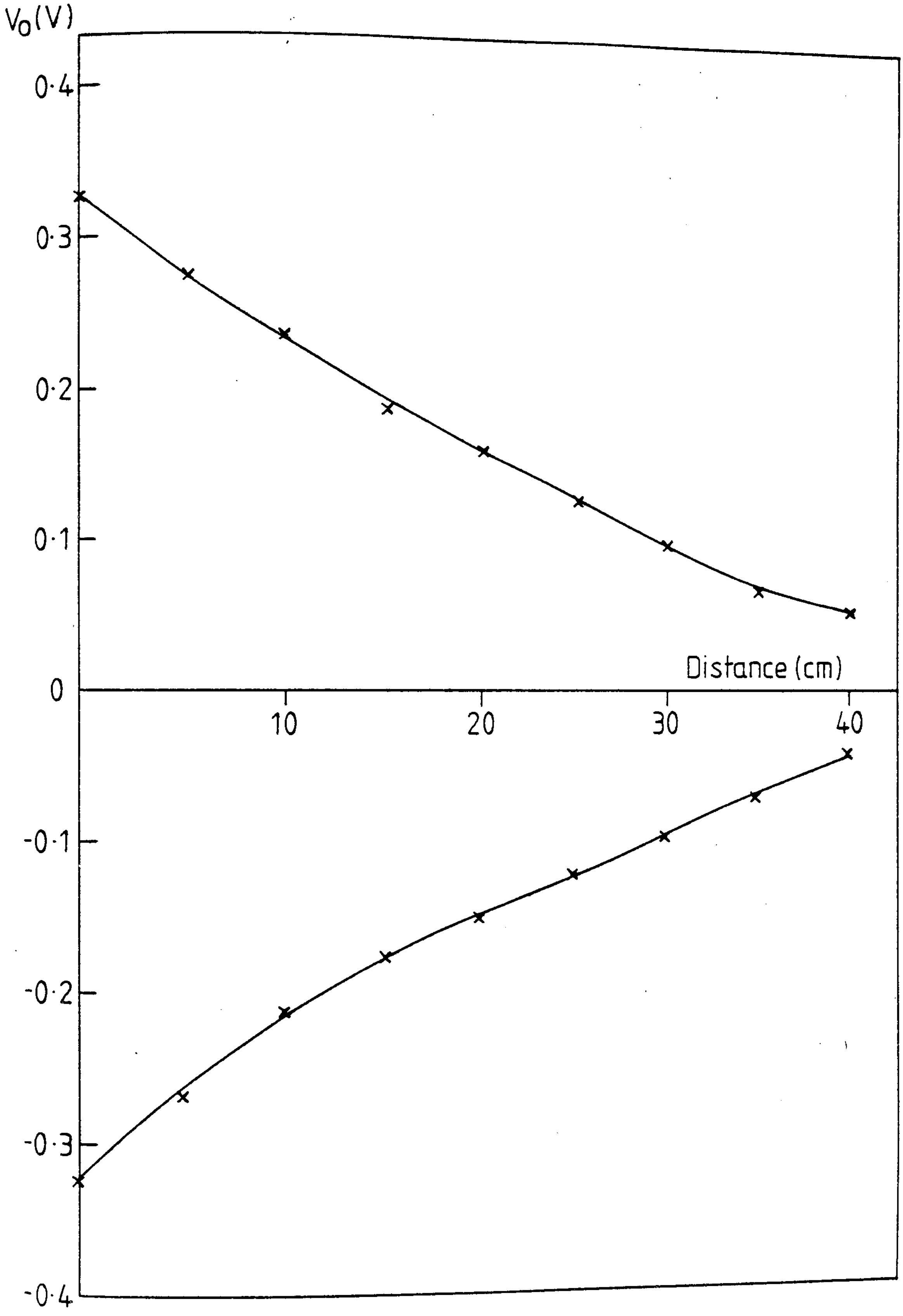

Fig 4.5 The output of the p.s.d. against distance along a line parallel to y-axis for object size (1×3×5cm) using T shape excitation coil, 200 turns, 1A current and 1m between the flux-gate and coils.

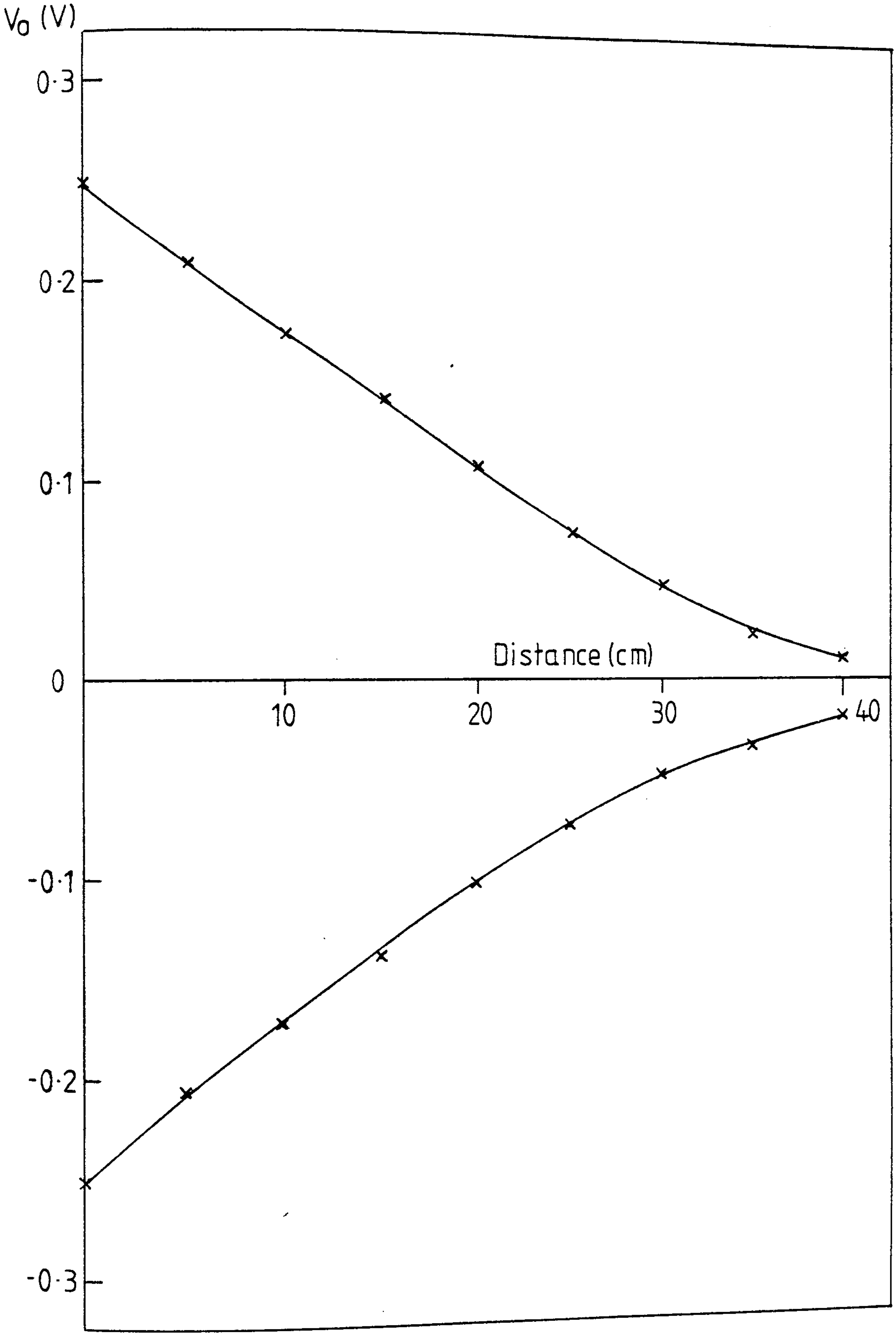

Fig 4.6 The output of the p.s.d. against distance along a line parallel to y-axis for object size (1×3×5 cm) using T shape excitation coil, 200 turns, 1A current and 1·25 m between the flux-gate and coils.

4.4.2 The Square Loop Electromagnetic Coil

According to the theoretical analysis given in section 3.4, the field distribution of the loop electromagnetic source is basically determined by the physical size of the loop. In practice, the loop is therefore constructed with a size capable of scanning the complete belt area of a specific conveying system. The geometry of the system using the loop electromagnetic coil is shown in Fig. 4.2. Since by symmetry the x-component of the field at each half of the loop is equal and opposite; the net field on the flux-gate is zero. The flux-gate detects any ferrous object in the zone of the system and gives an output voltage which indicates the presence of the object.

As was stated previously, (section 4.4.1), the transmitting loop and the flux-gate were situated in two parallel planes with a vertical distance of 30 cm. If the loop and flux-gate are placed in the same plane, the detection range of the equipment decreases. The reason for this is that as the ferrous object moves away from the plane of the loop, the x-component of the field decreases after a certain point (Section 3.4), and the distance of the object from the flux-gate increases. When the flux-gate and loop are on parallel planes, the field has the same profile as before, but the distance of the object from the flux-gate reduces as the object moves away from the plane of the loop.

To investigate practically the performance of the detector, several square loops have been constructed with different sizes and number of turns. The loops were formed using SWG16 wire size. Using a loop side of 60 cm, 20 turns and with 1A current through the coil, the output of the phase-sensitive detector against the distance along the x-axis was measured. The results are given in Fig. 4.7. In the above measurement an object of size 1×3×5 cm was moved along x-axis, the vertical distance from the loop being 15 cm. The results of the measurement are in agreement with the theory given in section 3.4.1. The output has the same profile of the x-component of the field as that produced by the loop. The reason for this is that the flux-gate detects the intensifying effect of the ferrous object which is parallel to its axis (i.e. x-axis in Fig. 4.2). The x-component of the field of the square loop is maximum at the boundary of the loop. The results also show that the output is maximum at about 8 cm from the side of the loop in the direction of motion of the belt. The reason for this is that the output of the flux-gate is a function of the excitation field as well as the distance from the flux-gate for a given size of object. The output of the phase-sensitive detector has also been measured using the same loop and current for different distances of the object along a line parallel to the y-axis at x = 15 cm. The results of the measurements are given in Fig. 4.8. When the object was on the axis of

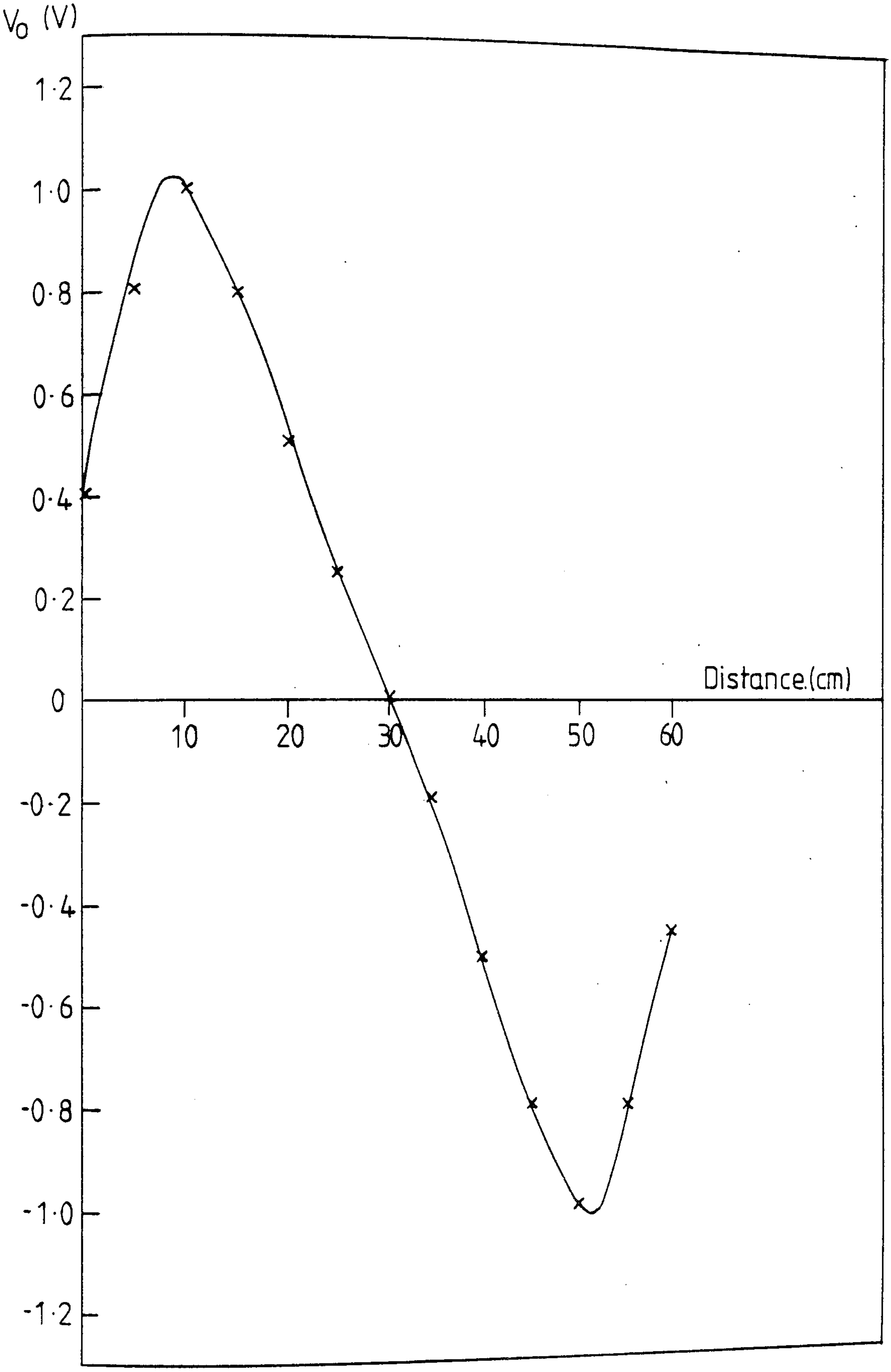

Fig 4.7 The output of the p.s.d. against the distance along the x-axis for object size (1×3×5cm) Using loop electro-magnetic coil, 20 turns, 1A current and loop side of 60cm.

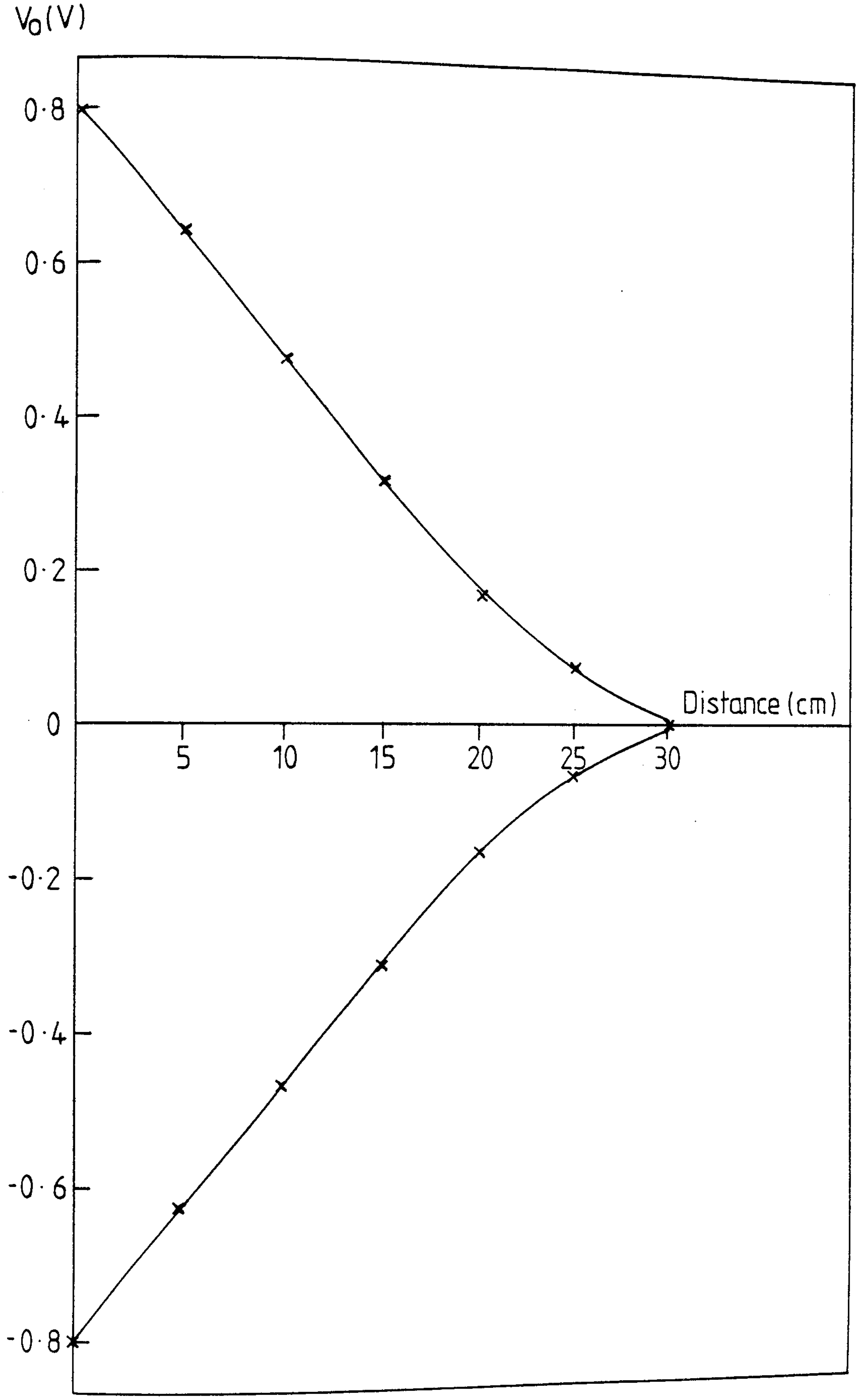

Fig 4.8 The output of the p.s.d. against distance along a line parallel to y-axis for object size (1×3×5 cm) Using square loop electromagnetic coils 20 turns, 1A current and 60 cm loop side.

the flux-gate the output was maximum and reduces with distance from the x-axis. From the above results it is clear that the detection range of the system is limited by the sides of the loop. The detection range of the equipment could therefore be extended to cover any required belt width by using appropriate loop dimensions. Fig. 4.8 shows that the output due to the presence of the object reduces to very small values near the sides of the loop which are parallel to the x-axis. To scan the required belt width completely, in practical applications of the equipment, the loop sides should be designed to be larger than the given belt width.

Comparing the results of the measurement for the T-shape coil and the loop coil, it is noted that the size of the geometry of the system in the case of the loop electromagnetic coil is less than the size of the comparable T-shape. It is therefore this geometry that was selected as a field source in the practical implementation of the detector.

4.4.3 The Power Amplifier

The amplifier shown in Fig. 4.9 was used to drive the electromagnetic coil from the oscillator. In this circuit an RS TDA 2030 integrated circuit amplifier is employed. The device is capable of producing an output power of 13 watts into a load impedance of 4Ω in the frequency range of up to 80 kHz.

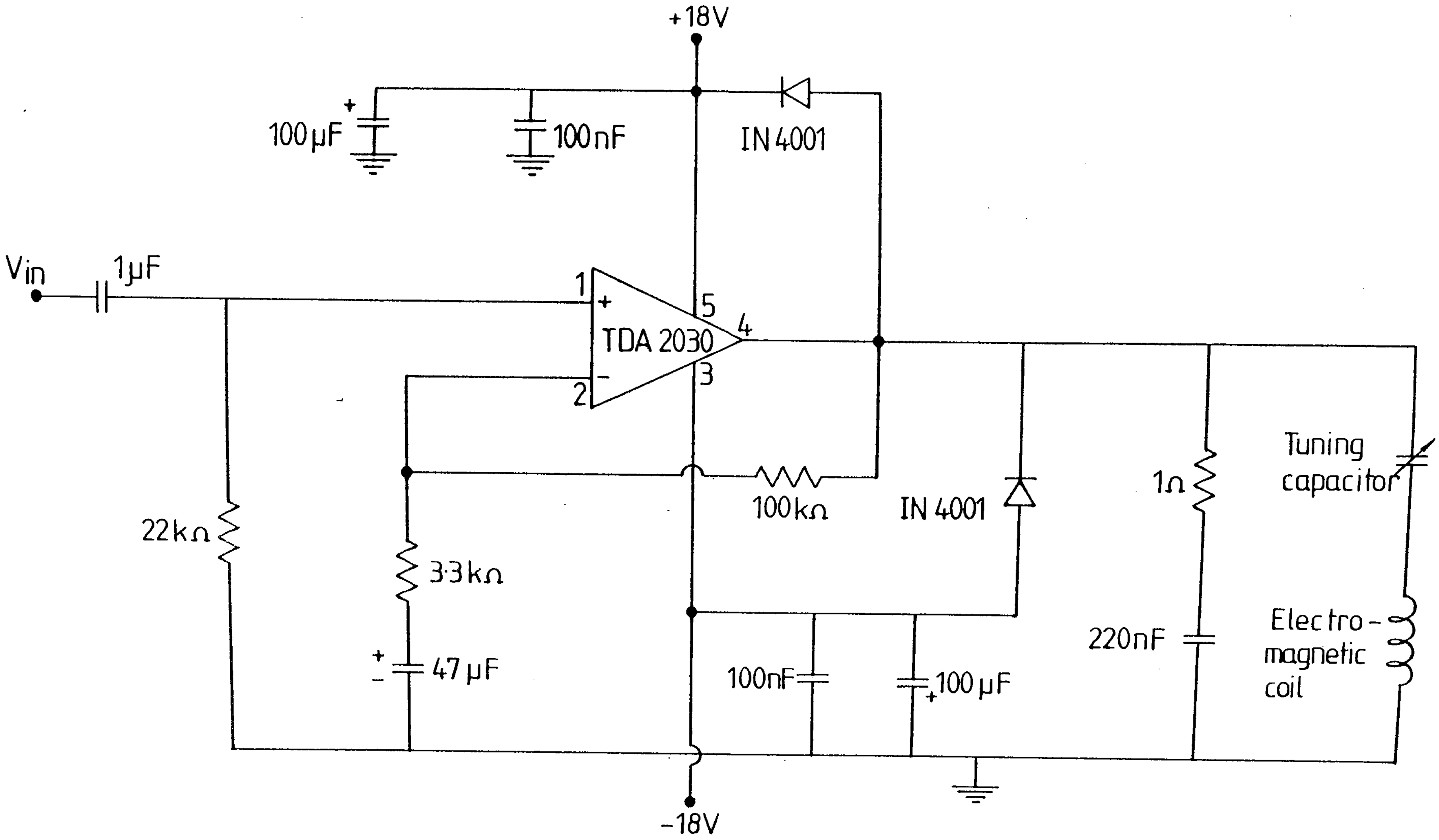

Fig 4.9 Circuit diagram of the power amplifier

The circuit diagram of the power amplifier was taken from the RS catalogue. The amplifier was built with short circuit protection, thermal stabilisation and safe operating area protection. The amplifier was mounted on a heat-sink to provide a means of heat dissipation when the amplifier is in operation.

Using the above circuit, the electromagnetic coil was fed with 1A rms current. The coil was connected in series with a capacitor, to tune the coil to the resonance at the operating frequency so as to increase the system efficiency. At the selected drive frequency of 10 Hz the value of the capacitor needed to achieve the resonance condition is very large. It was therefore difficult to tune the system properly to the resonance. A reasonable compromise therefore was achieved which gave satisfactory performance.

4.5 DEVELOPMENT OF THE RECEIVING SYSTEM

The receiving part of the detector consists of the flux-gate magnetometer and electronic circuits to process the output of the flux-gate to indicate the presence of the ferrous object.

It was mentioned earlier in this chapter that the equipment was intended to be used for the detection of ferrous objects in coal conveyors for power stations. The equipment was therefore designed to take the power station environment into consideration. Having detected the ferrous object on the coal conveyor it has to provide the necessary signal for switching on the electromagnetic separator to extract the tramp iron from the coal. The complete block diagram of the receiver is given as Fig. 4.10. The following sections describe the practical development of the equipment receiver in detail.

4.5.1 The Flux-gate Magnetometer

The flux-gate provided for this project was produced by Thorn Electronics. It is a ring core parallel gated magnetometer with an output voltage proportional to the steady-state magnetic field. The schematic diagram of the flux-gate is shown in Fig. 4.11. The design of the 'Thorn Electronics' flux-gate closely resembles that described in Reference (6). It is highly probable that the Thorn flux-gate is based on this design. Referring to Fig. 4.11 the drive oscillator is shown supplying primary coils A and B. The degree of saturation to which the ring core is subjected is governed by resistor R_S. Reference (6) gives details of a minature, low power magnetometer which can be used for vehicle detection.

The centre-tapped secondary coil produces two output waveforms of identical sign. The detection circuit consists of two diodes and a smoothing circuit. The output of the flux-gate is the difference in the voltage produced by the C and D secondary coils. This output is dependent

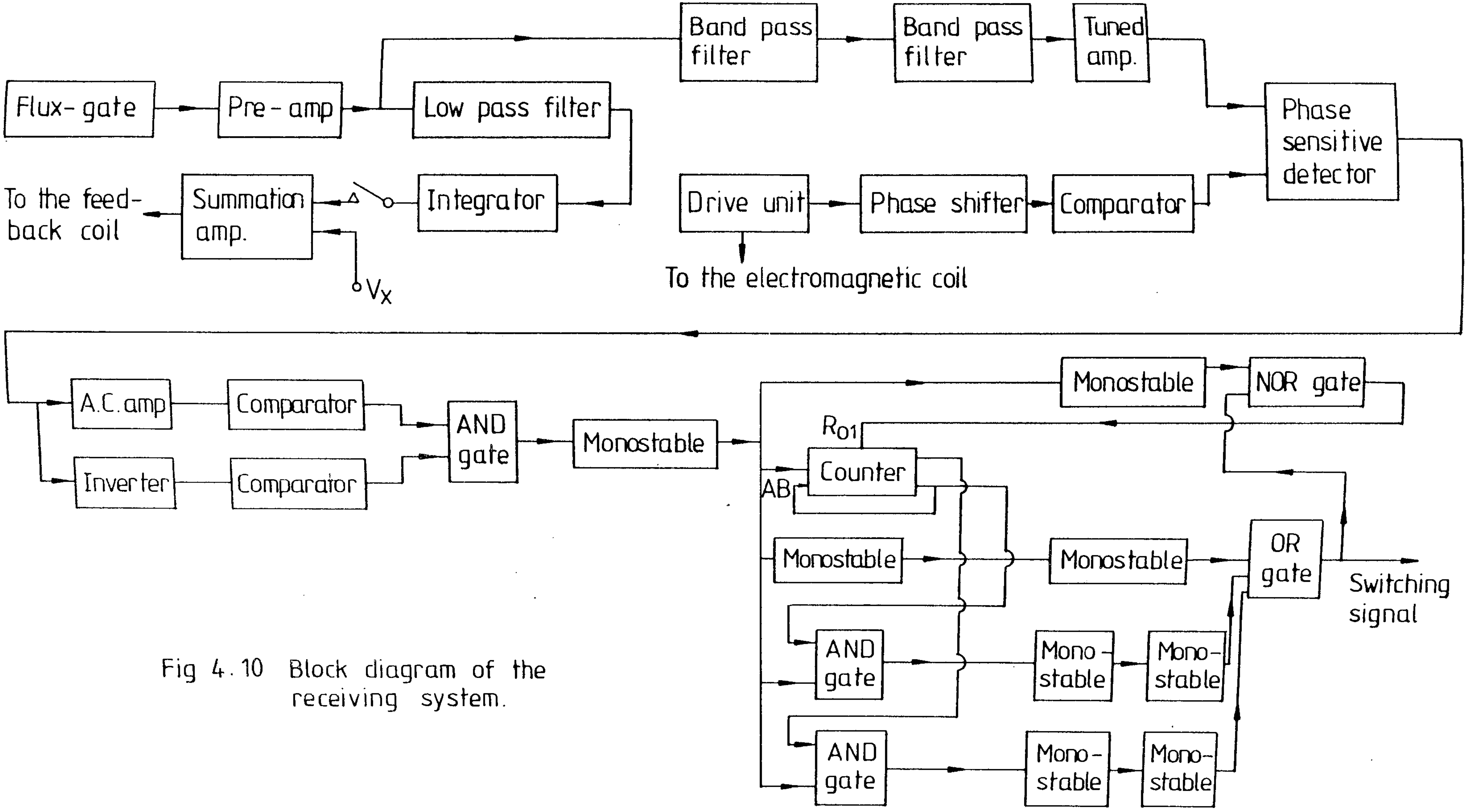

Fig 4.10 Block diagram of the receiving system.

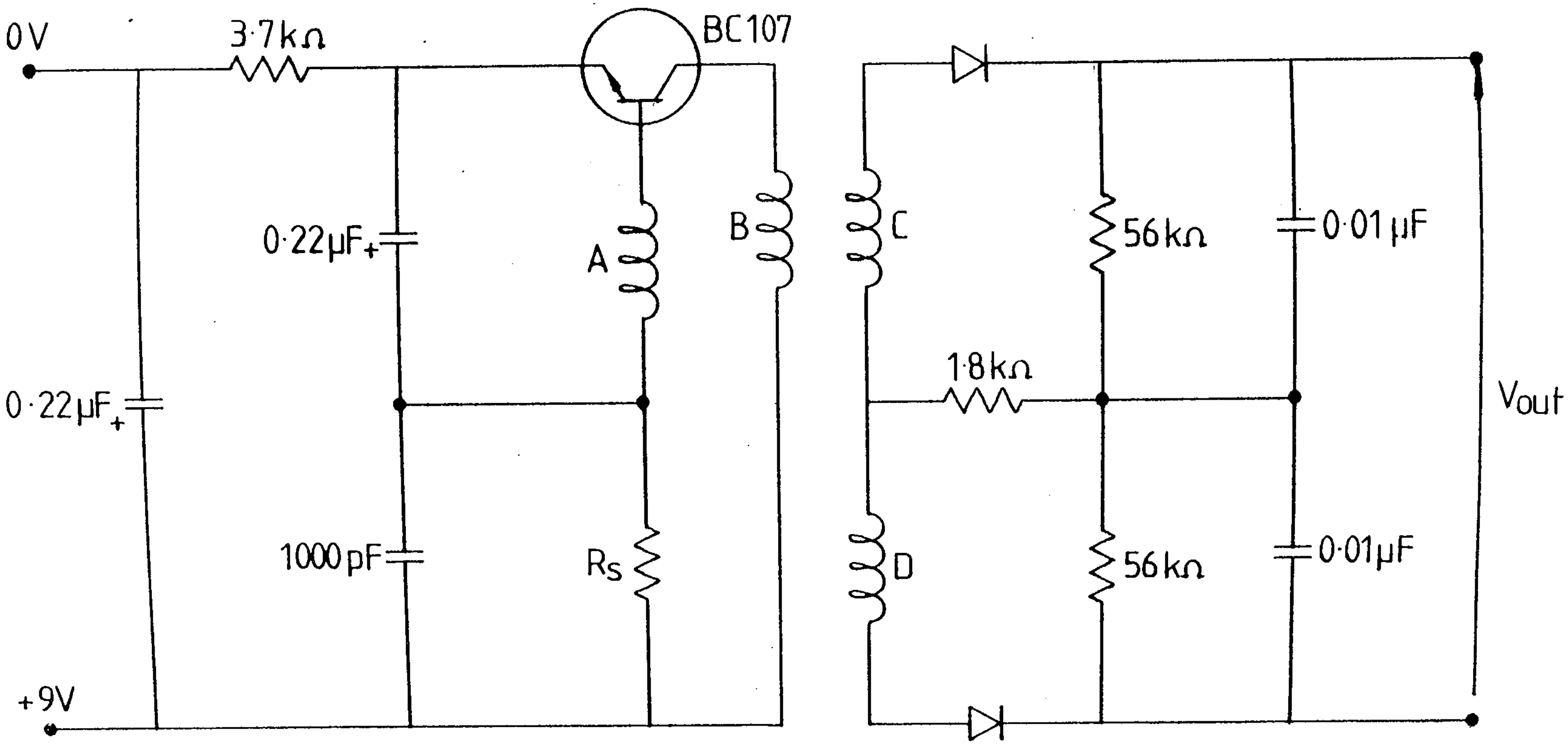

R_S has been selected to give a dynamic range of ± ·08 × 10^{-4} Tesla

Fig 4.11 Ring core flux-gate magnetometer circuit diagram on the component of the external field parallel to the axis of sensing coil.

The frequency response of the flux-gate was measured by driving the flux-gate feedback coil with signals of different frequencies and constant amplitude and measuring the output of the pre-amplifier after the flux-gate. The results of the test are given in Fig. 4.12. It can be seen from this graph that the magnetometer acts as a low-pass filter with -3 dB at about 17 Hz. This means that the flux-gate cannot satisfactorily detect magnetic fields at frequencies much above 17 Hz. A frequency of 10 Hz was therefore chosen for the excitation field in the ferrous metal detector.

4.5.2 Signal Conditioning Circuit

Since the output of the flux-gate was very small, an amplifier was needed to amplify the output to a reasonable level for both control system and detection purposes.

The output impedance of the flux-gate is relatively high ≃56kΩ. A high input impedance amplifier is therefore necessary to avoid loading the output voltage from the flux-gate to the amplifier. The amplifier was located as close as possible to the magnetometer to prevent pick-up of stray voltages by the connecting wires.

In the power station environment there is a very high 50 Hz stray field which may be detected by the equipment,

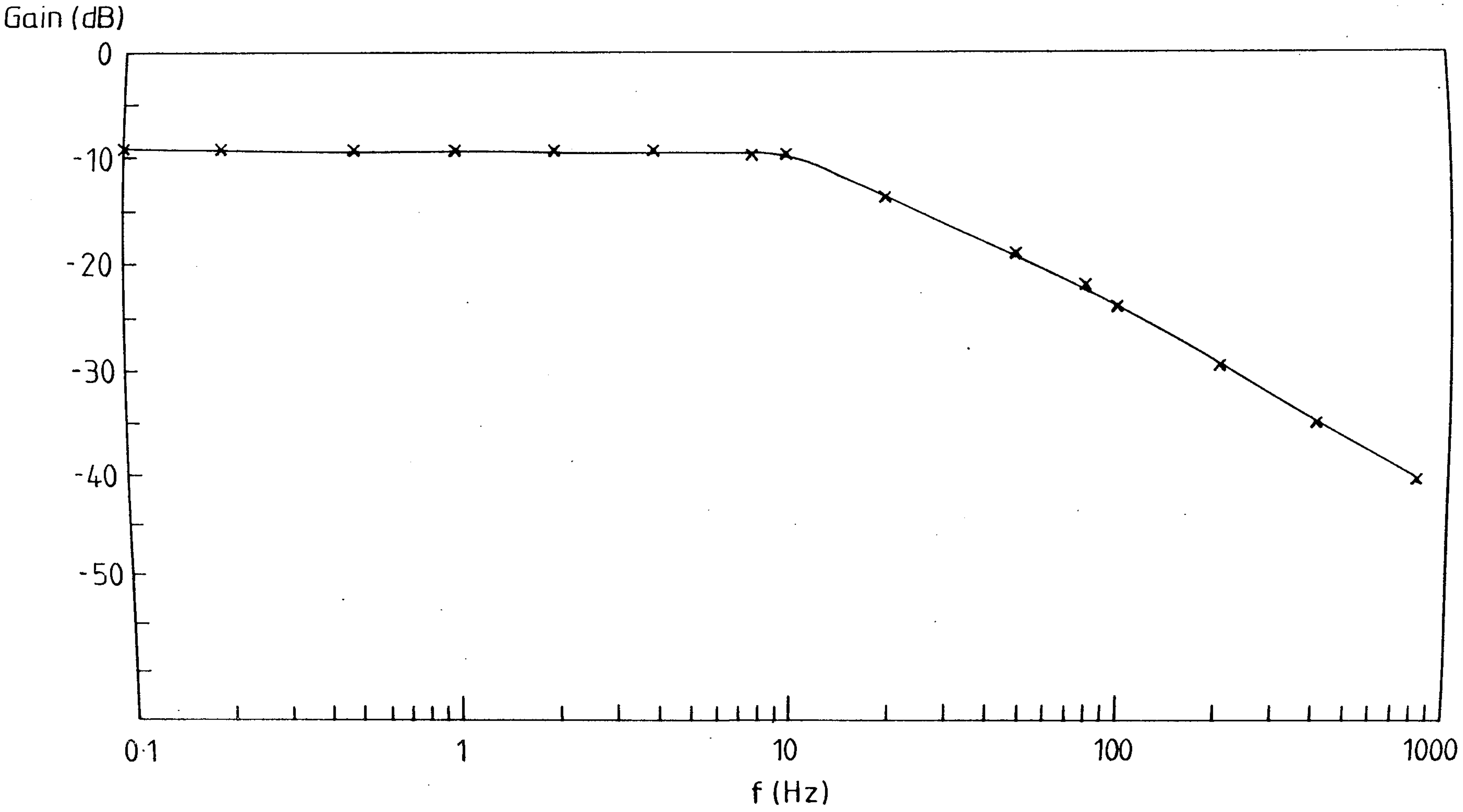

Fig 4.12 Frequency response of the flux-gate magnetometer. The output was measured at the output of the amplifier following the magnetometer, while the input was injected to the feedback coil, with amplitude of 6V p.p.

causing false switching of the magnetic separator. Section 4.7 describes the application of the detector in the power station. To overcome the above problem, two stages of bandpass filter, tuned to the drive frequency (10 Hz), were connected to the output of the pre-amplifier. The received signal is further amplified by a tuned amplifier with centre frequency at 10 Hz. This increases the sensitivity and accuracy of the detector. The circuit diagram of this part of the receiver is shown in Fig. 4.13. The frequency response of the cascaded bandpass filters with the tuned amplifier is given in Fig. 4.14. From this it can be seen that the 3 dB bandwidth of the cascaded bandpass filter and amplifier is about 1.5 Hz. This means that almost all unwanted signals can be eliminated thus increasing the accuracy of detection.

4.5.3 The Phase-sensitive Detector

If a waveform to be measured is obscured by a high level of noise, then a phase sensitive detector may be used to measure the amplitude and phase of the signal of interest. In this work, the signal produced by the presence of the ferrous object is very small compared to the expected noise signals produced by the rollers of the conveyor belt and other stray fields. The phase sensitive detector is therefore suitable for detecting the signal of interest and producing the signature of the movement of the ferrous object as it passes through the detection zone of the equipment.

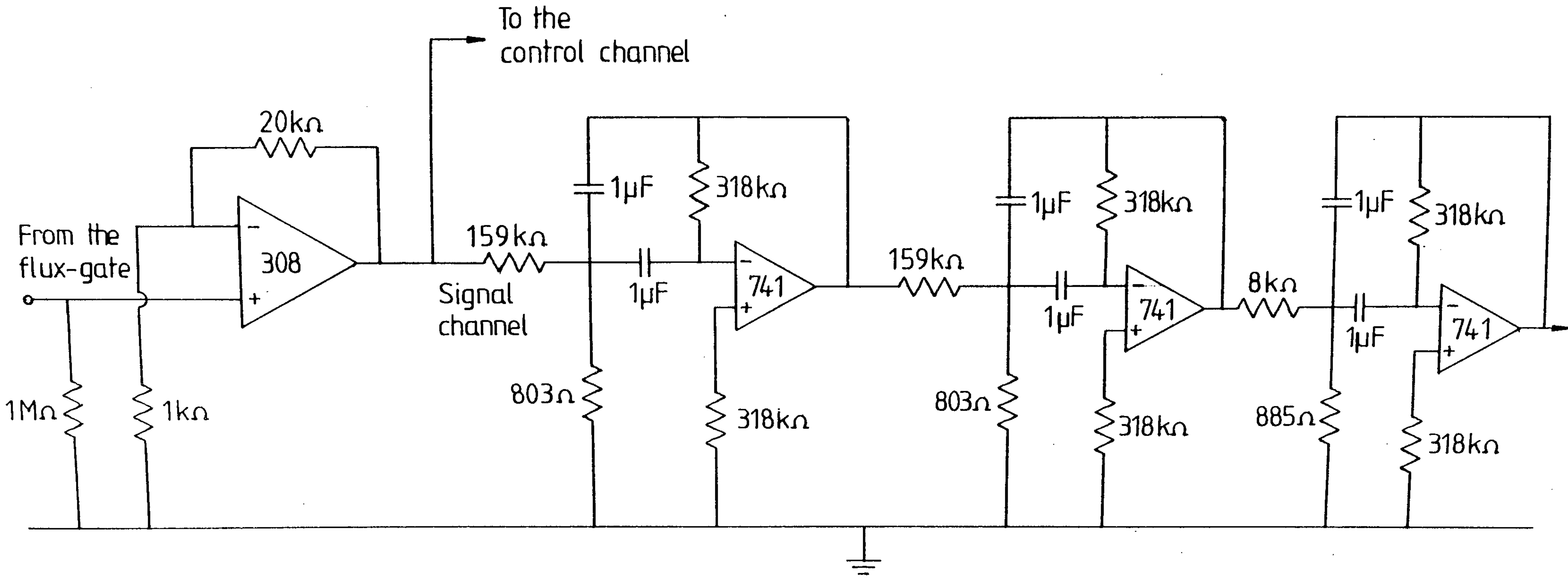

Fig 4.13 The signal conditioning circuit diagram.

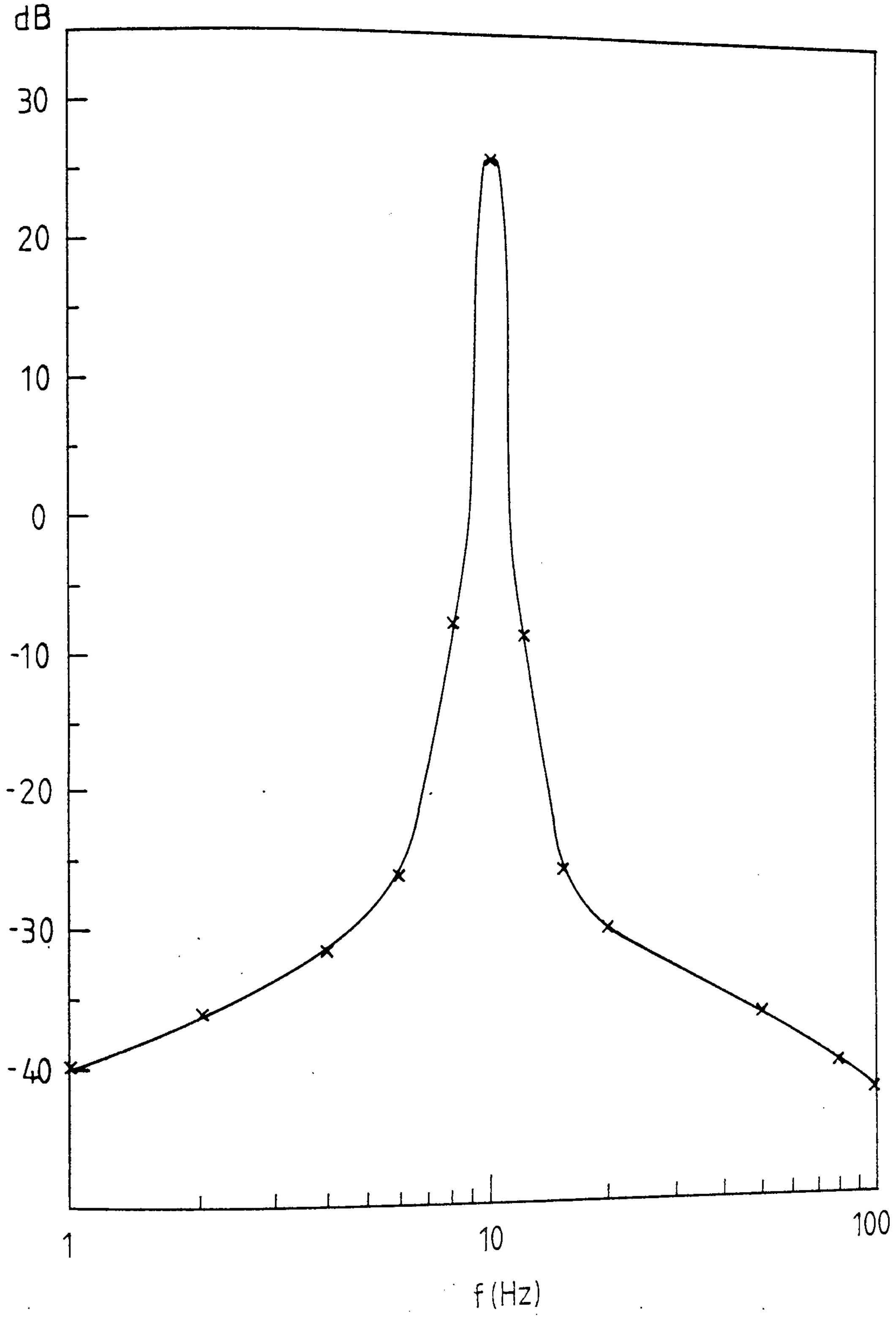

Fig 4.14 Frequency response of the cascaded band pass filters and tuned amplifier.

A phase-sensitive detector can be simply represented by a two-position switch which alternately selects or 'gates' either the signal or the inverted signal into a low-pass filter. The switching action is controlled by a reference or gating signal which is at the same frequency as the signal to be measured. The block diagram of the phase-sensitive detector is shown in Fig. 4.15.

The identical phase-sensitive detector was employed in the ferrous and non-ferrous detector. The analysis and circuit diagram of the phase-sensitive detector are not therefore included here but are given later in the chapter describing the design and construction of the ferrous and non-ferrous detector. The output of the tuned amplifier was fed into the signal input of the phase-sensitive detector. Because of the geometry of the coils and flux-gate, the field components produced by each half of the loop parallel to the axis of the flux-gate are opposite to each other. The signal due to the presence of a ferrous object in one side of the magnetometer is 180° out of phase with the signal due to the presence of the object on the other side of the flux-gate. The reference input of the phase-sensitive detector is connected to the drive unit. In this way the received signal and reference input are synchronised to one another. The phase-sensitive detector demodulates the input signal and gives the signature of the movement of the object on the belt.

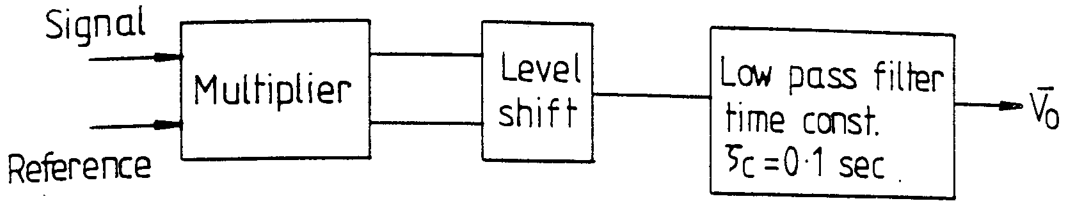

Fig 4.15 Block diagram of the phase sensitive detector

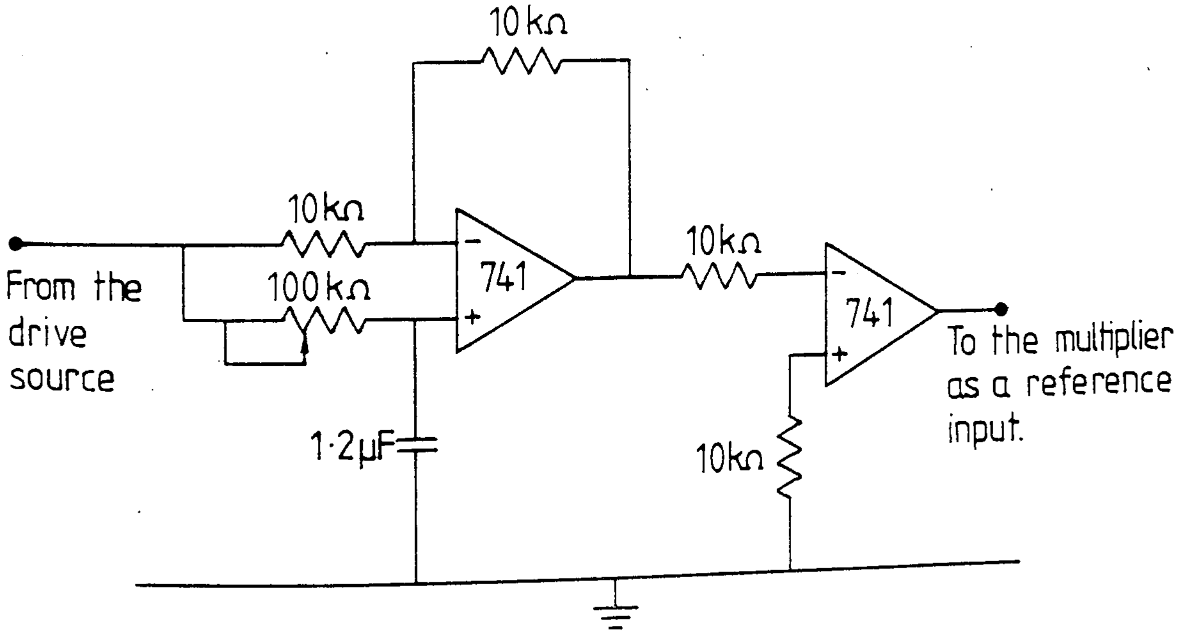

Fig 4.16 The phase shifter and comparator circuit diagram

When the phase-shift between the input signal and the reference signal is zero, the output of the phase-sensitive detector is maximum positive and it is maximum negative when the phase difference is 180°. The reference signal is therefore adjusted to be in phase with the signal due to the presence of the object in one side of the flux-gate and 180° out of phase with the signal from the object on the other side of the flux-gate.

The rate of response of the equipment to the presence of an object on the belt depends on the time constant of the low pass filter. The bandwidth of the phase-sensitive detector is also dependent on the time constant (τ_c) of the low pass filter. An optimization can therefore be made between the rate of response of the system and the bandwidth of the phase-sensitive detector for any particular speed of the belt for a given application of the equipment.

4.5.4 Phase Correction Network and Comparator

A phase correction network was employed in the path of the reference signal, to adjust the phase-shift between the signal input and reference input to the phase-sensitive detector to either zero or 180°.

Normally, a square wave is fed into the reference input of the phase-sensitive detector. Since the signal from the drive unit is sinusoidal, a zero crossing detector was used after the phase correction network to obtain the required square wave. The circuit diagram of the phase correction network and zero crossing detector is given in Fig. 4.16.

4.5.5 A.C. Amplifier and Inverter

The output of the phase-sensitive detector is connected to an a.c. amplifier. The circuit diagram of the amplifier is shown in Fig. 4.17. By employing an a.c. amplifier the d.c. offset and d.c. drift voltages may be eliminated. This circuit also attenuates all the frequencies below the cut-off frequency $(\frac{1}{2\pi R_1 C})$ and passes the signals above this frequency with gain of $\frac{R_2}{R_1}$. The values of R_1, R_2 and C are chosen to match any particular speed of the belt, the dimensions of the electromagnetic coil and the sensitivity requirements for a specific application of the equipment. The component values in Fig. 4.17 were selected as suitable for a belt speed of about 1.6 m/s and a square loop side of 60 cm.

As already mentioned, the output of the phase-sensitive detector is positive when the ferrous object is to one side of the flux-gate and negative to the other side of the flux-gate. To make use of the signals from the both sides, an inverter was employed at the output of the a.c. amplifier. In feeding the outputs of the unity-gain inverter and a.c. amplifier into two individually biased comparators, it is possible to convert the signals from both sides of the flux-gate into TTL

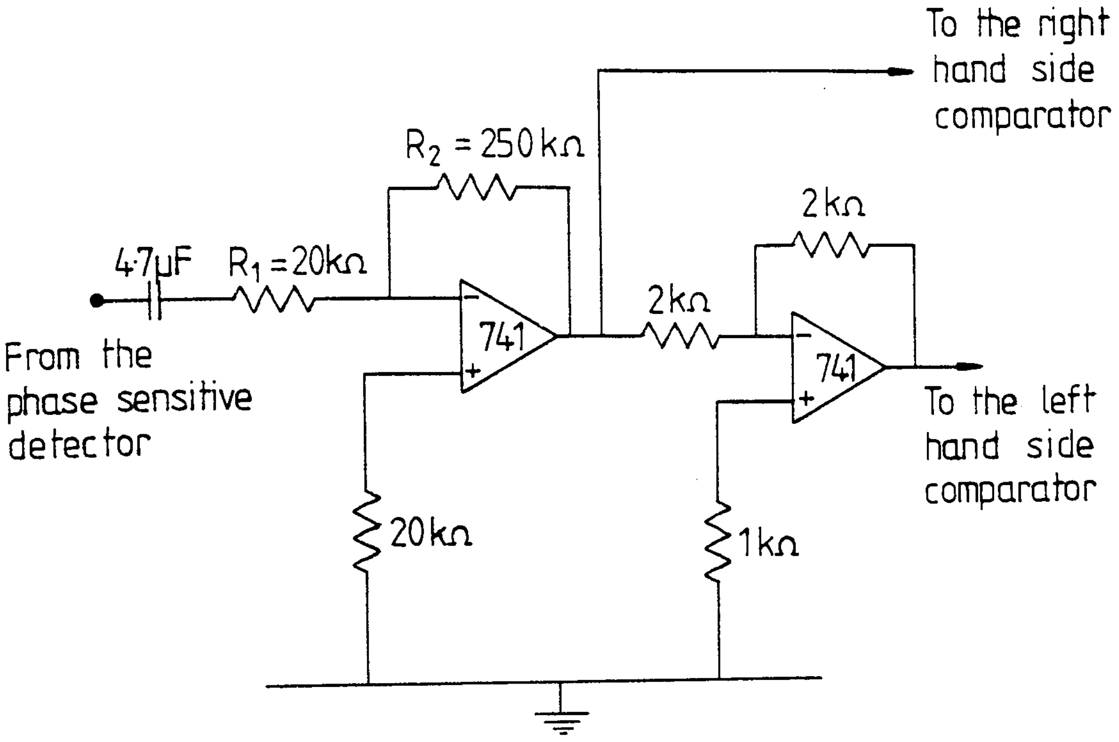

Fig 4.17 The A.C. amplifier and inverter

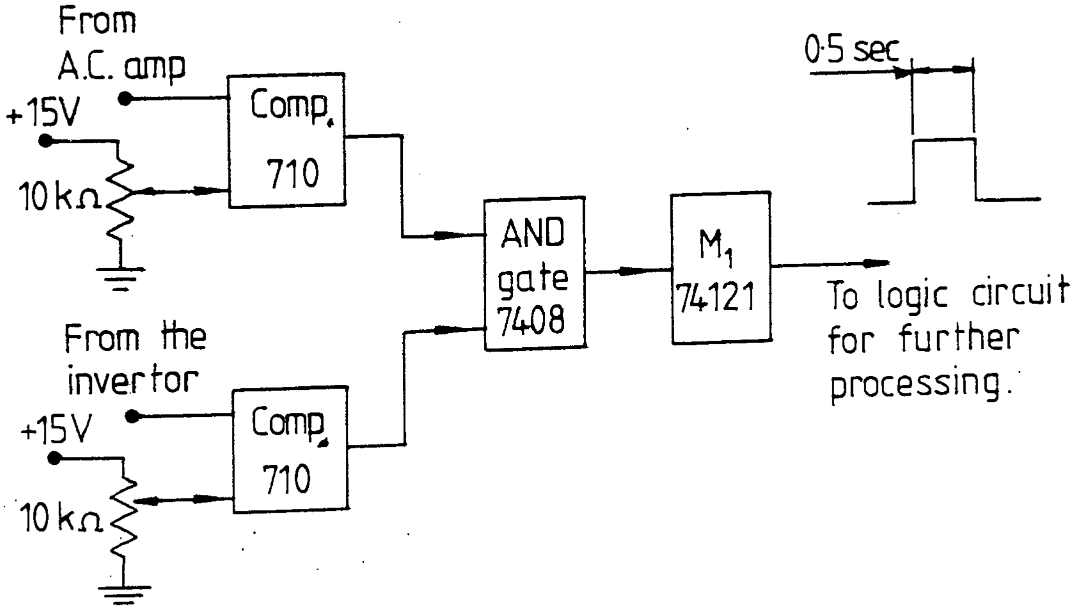

Fig 4.18 TTL pulse shaping circuit diagram

compatible pulses. These are further processed to indicate the presence of a ferrous metal object and provide the appropriate pulse for switching on the electromagnetic separator when required.

4.5.6 The Biassed Comparators and Pulse Shaping Circuit

Two integrated circuit voltage comparators type 710 giving a TTL compatible pulse output with a sensitivity of a fraction of a millivolt are used to convert the analogue signals to TTL compatible signals. The a.c. amplifier and inverter each drives one comparator and the threshold level is adjusted to identify the signal from the background noise.

When a ferrous metal is passed through the detection zone of the equipment, each comparator gives a TTL output signal. An AND gate is used at the output of the comparators to combine the two pulses from them. To obtain a single output pulse for each object a positive-edge-triggered monostable (M_1) was connected to the output of the AND gate. The output pulse duration was adjusted to be just greater than the period which the object takes to travel within the detection range of the system. For a loop side of 60 cm and belt speed of 1.6 m/s, the duration has to be made about 0.5 sec. The schematic diagram of the pulse shaping circuit is shown in Fig. 4.18.

4.5.7 Logic Circuit to Eliminate the Masking Effect

The period of the monostable (M_1) in Fig. 4.18 should be made short enough to ensure that if a second piece of ferrous metal arrives during this period, it would be extracted. This condition is nearly always satisfied, since it only needs to be long enough to override the occurrence of two pulses when one piece of ferrous material passes through the detection range of the equipment. The system is therefore blind to further tramp iron only during the energising period of the high power switch. The logic circuit shown in Fig. 4.19 is used to overcome this problem. This can be best explained by considering the events when the tramp iron is detected. If there is no tramp iron, the system is quiescent and the output of the circuit in Fig. 4.19 is zero as well as both inputs to NOR_1. When a metal object is detected, monostable (M_1) gives an output pulse with a fixed period. On the leading edge of this pulse monostable (M_2) starts its timed period, in turn putting a high input on NOR_1. This changes the counter 7490 from reset mode to count mode, because the input on $R_{o(1)}$ is low. On the falling edge of the pulse from the monostable (M_1), the counter records one and the output goes high. The output of monostable (M_1) is delayed by monostable (M_{d1}) for a certain period depending on the detector-separator distance and the energising time constant of the separator. The delayed pulse triggers monostable (M_3) which causes it to begin

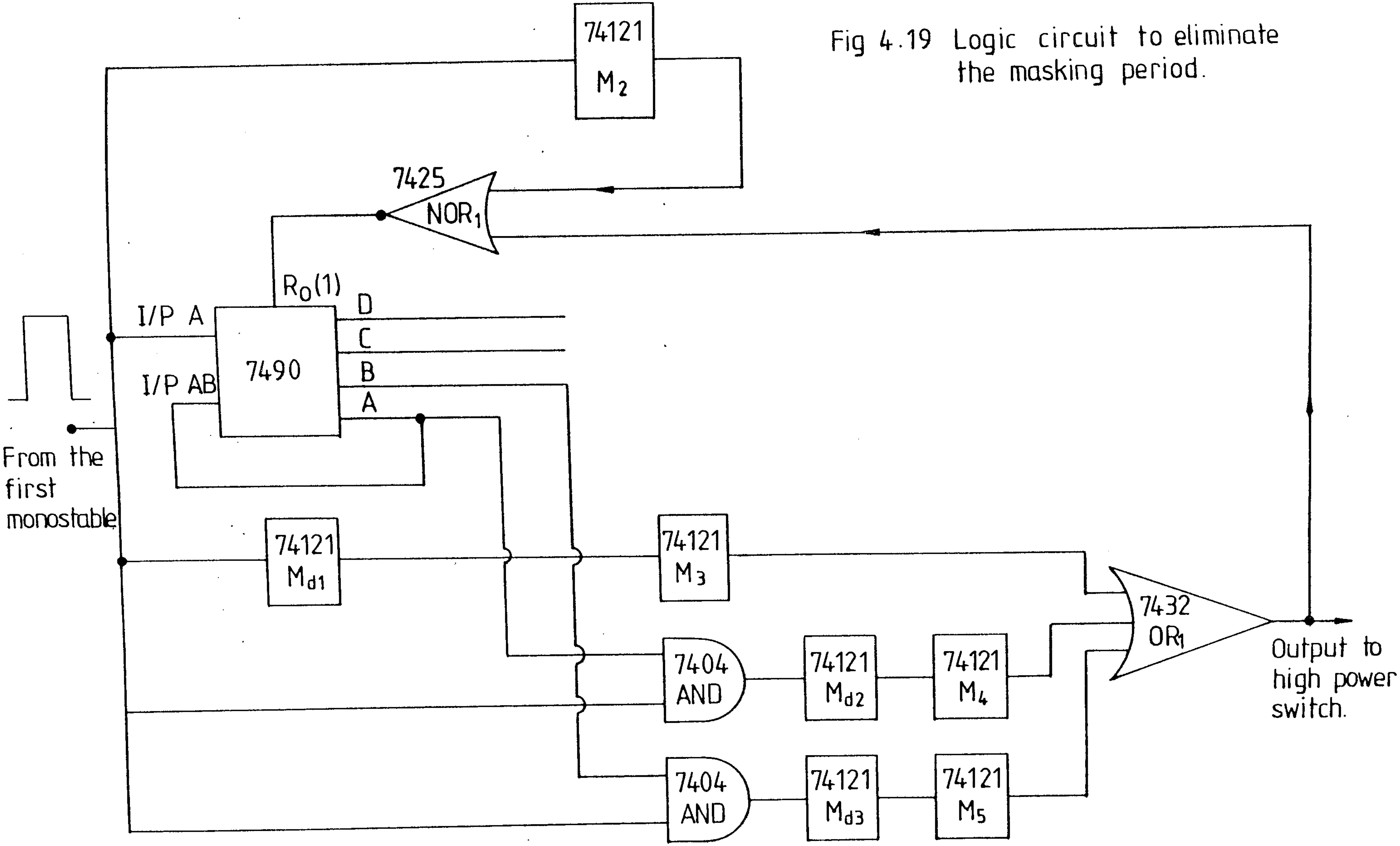

Fig 4.19 Logic circuit to eliminate the masking period.

its timed period. Since M_3 is energised, the output from OR_1 is high. This energises the magnet and also puts a high input to NOR_1. The high output of OR_1 maintains the 7490 in count mode. When the timed period of M_2 is ended, the 7490 stays in count mode until the output of OR_1 eventually goes low. If a second pulse arrives during M_3 timed period, it could not see the pulse. However, the input to AND_1 is high for the duration of the second input pulse and from the previous input pulse, the output A of the 7490 is also high. Monostable (M_4) therefore starts its duration after the delayed period. The monostable (M_4) ensures that the magnet stays energised long enough to remove the second metallic object. Meanwhile, on the falling edge of the second pulse the 7490 counts, putting the output B high and hence a third input pulse sets the monostable (M_5) high and so on. Supposing that the third pulse has not arrived, at the end of M_4 timed period, the output of the OR_1 goes low and the counter is reset, hence the system returns to the primed state.

4.6 THE CONTROL SYSTEM FOR ELIMINATING THE EARTH'S FIELD

4.6.1 General

The flux-gate magnetometer detects the earth's field and gives an output proportional to this field. When the flux-gate has detected this field, it is no longer working on the centre of its characteristic for the purpose of detecting the field at the drive frequency. This will reduce the sensitivity of the system. Also, the rotation of the rollers of the conveyor belt disturbs the earth's field. The flux-gate detects this disturbance and gives a continuously false detection signal, making the equipment ineffectual.

These problems may be overcome by employing a feedback control system for automatically eliminating the earth's magnetic field.

4.6.2 Electronic Design of the Control System

The circuit diagram of the control system is given in Fig. 4.20. The system makes use of the following items:-

(1) Pre-Amplifier

This amplifier is required because the output of the flux-gate due to the earth's magnetic field is very small (between zero and ±300 mV). An amplifier with a gain of 20 was employed after the flux-gate , to make the signal adequate for further processing.

(2) Low Pass Filter

If the output of the pre-amplifier was fedback directly, then the output of the flux-gate,due to magnetic fields at all frequencies would have been attenuated, including the drive frequency. This means the control circuit would reduce the overall sensitivity of the equipment. An active low-pass filter was therefore used

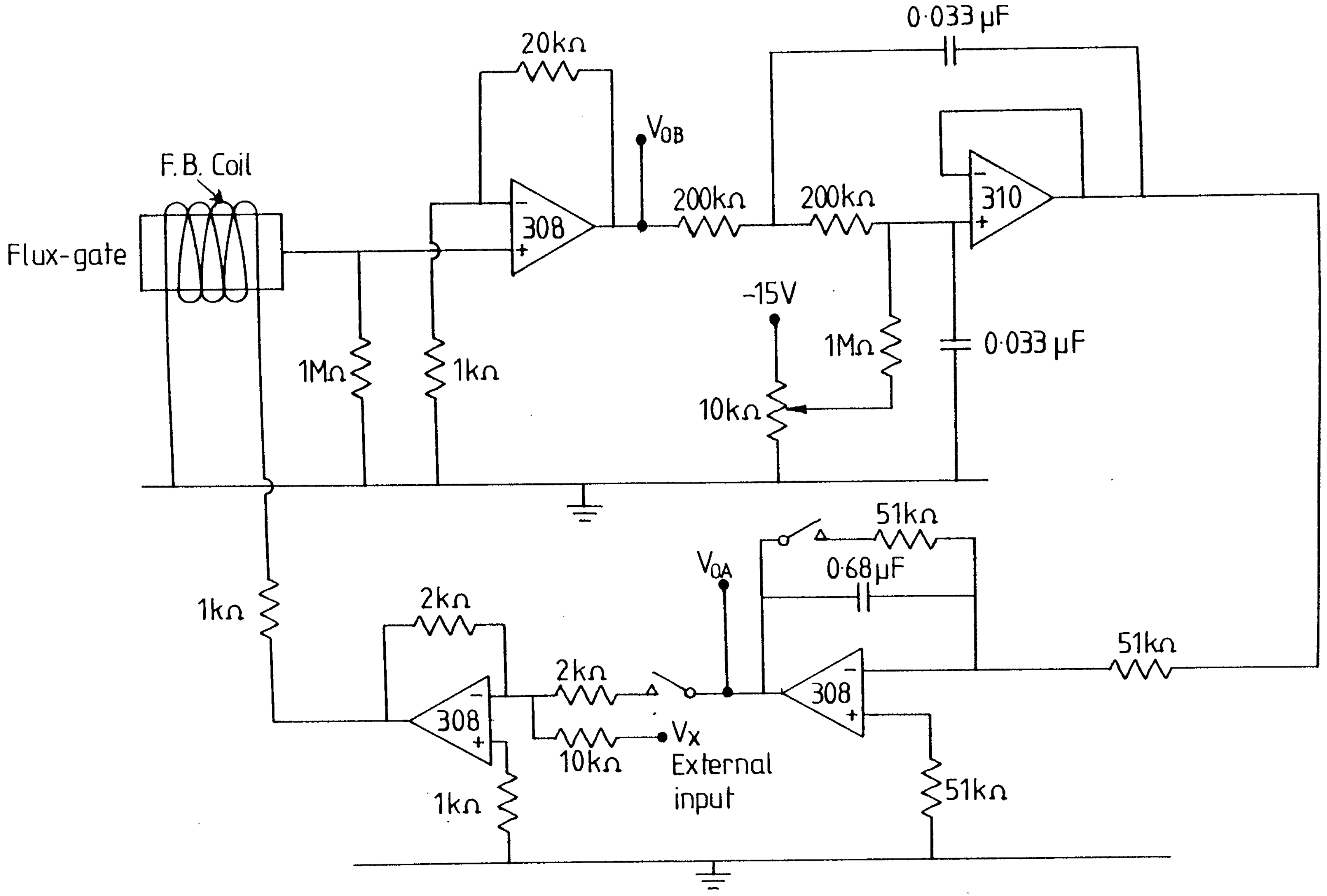

Fig 4.20 The circuit diagram of the control system

which passes all the frequencies below the drive frequency with a minimum attenuation, but heavily attenuates the drive frequency. The frequencies below the drive frequency, therefore, go through to the feedback coil and generate a magnetic field opposite to the field detected by the flux-gate.

(3) Integrator

The output of the low-pass filter is integrated by an integrator consisting of a low-drift operational amplifier type LM 308, together with a capacitor and a high stability resistor. The integrator control eliminates the earth's field by providing automatically the signal required to drive the feedback coil in order to eliminate the effect of the earth's field$^{(47)}$. Using the integrator control, all frequencies below the drive frequency are also attenuated. A proportional control facility is provided by connecting a resistor in parallel with the feedback capacitor of the integrator to enable a comparison of the two modes of operation to be carried out.

(4) Summation Amplifier

The amplifier has two inputs, one from an external source and the other, the feedback voltage from the integrator. The amplifier inverts the signal from the integrator, making the overall feedback negative.

The performance of the control system was tested by injecting a signal V_x at the external input of the summation amplifier, as shown in Fig. 4.20, and measuring the output at points V_{OA} and V_{OB} for the three modes of operation (section 4.6.3)..

(5) Feedback Coil

This coil was constructed by winding 200 turns of a fine SWG 42 wire on a wooden frame around the flux-gate magnetometer. This coil produces a magnetic field proportional to the feedback signal, thus eliminating the earth's field completely and attenuating the unwanted fields with frequencies below the drive frequency.

4.6.3 Tests on the Control System

Various tests were carried out on the control system. It was found that the system worked sufficiently well to achieve the target requirements. The tests are discussed in the following sections.

4.6.3.1 Static Tests

Three sets of static tests were carried out for the three modes of the control system, open loop, proportional and integrator control. The measurements were made out at points V_{OA} and V_{OB} as shown in Fig. 4.20. The results of the tests are given in Figs. 4.21 and 4.22. It is obvious from the open-loop test that V_{OA} and V_{OB} have some values other than zero, although input V_x is zero. This means that the system was detecting the earth's field. Also, it is clear from the results that V_{OA} and V_{OB}

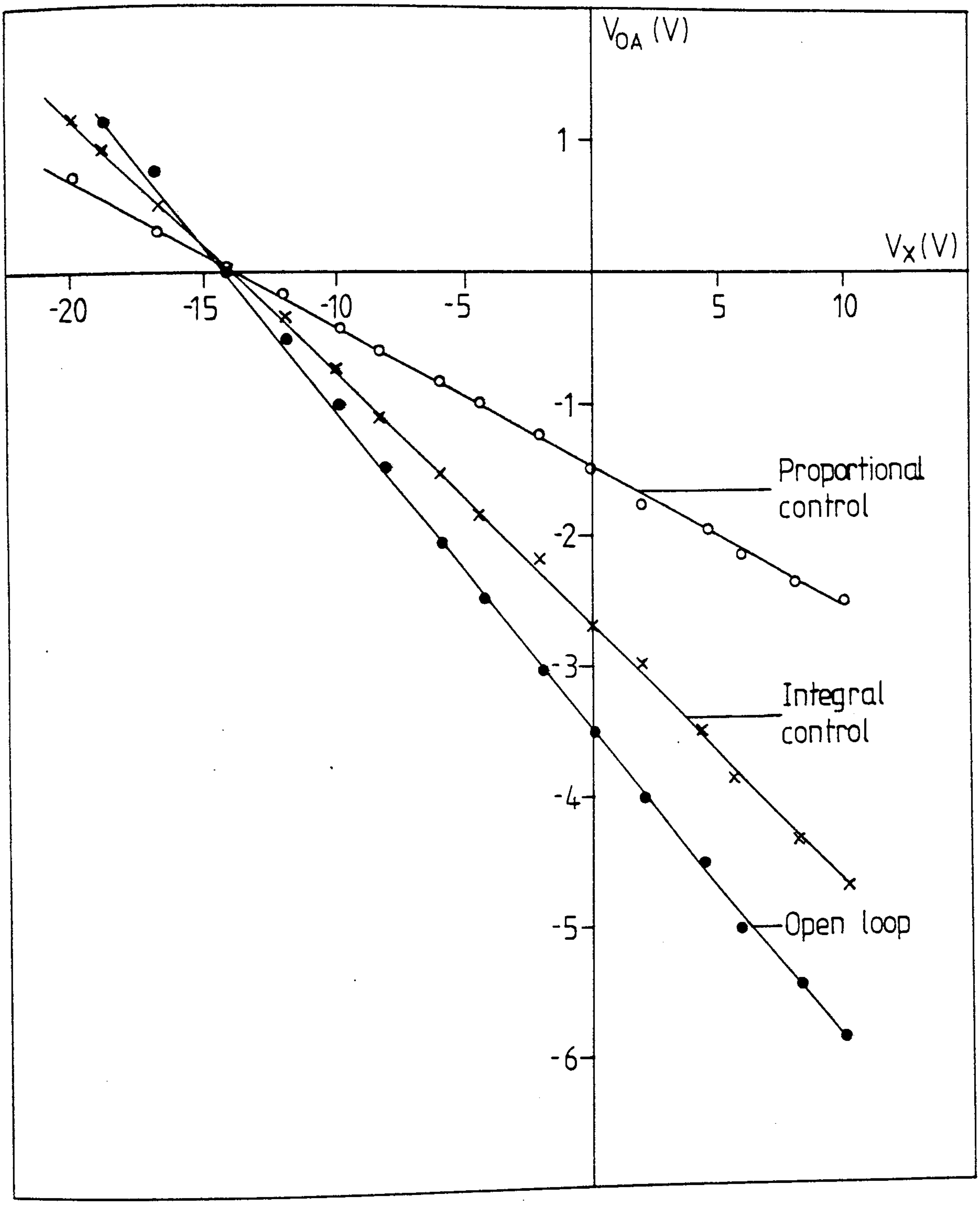

Fig 4.21 D.C. test on the control system. The output is measured at point V_{OA}.

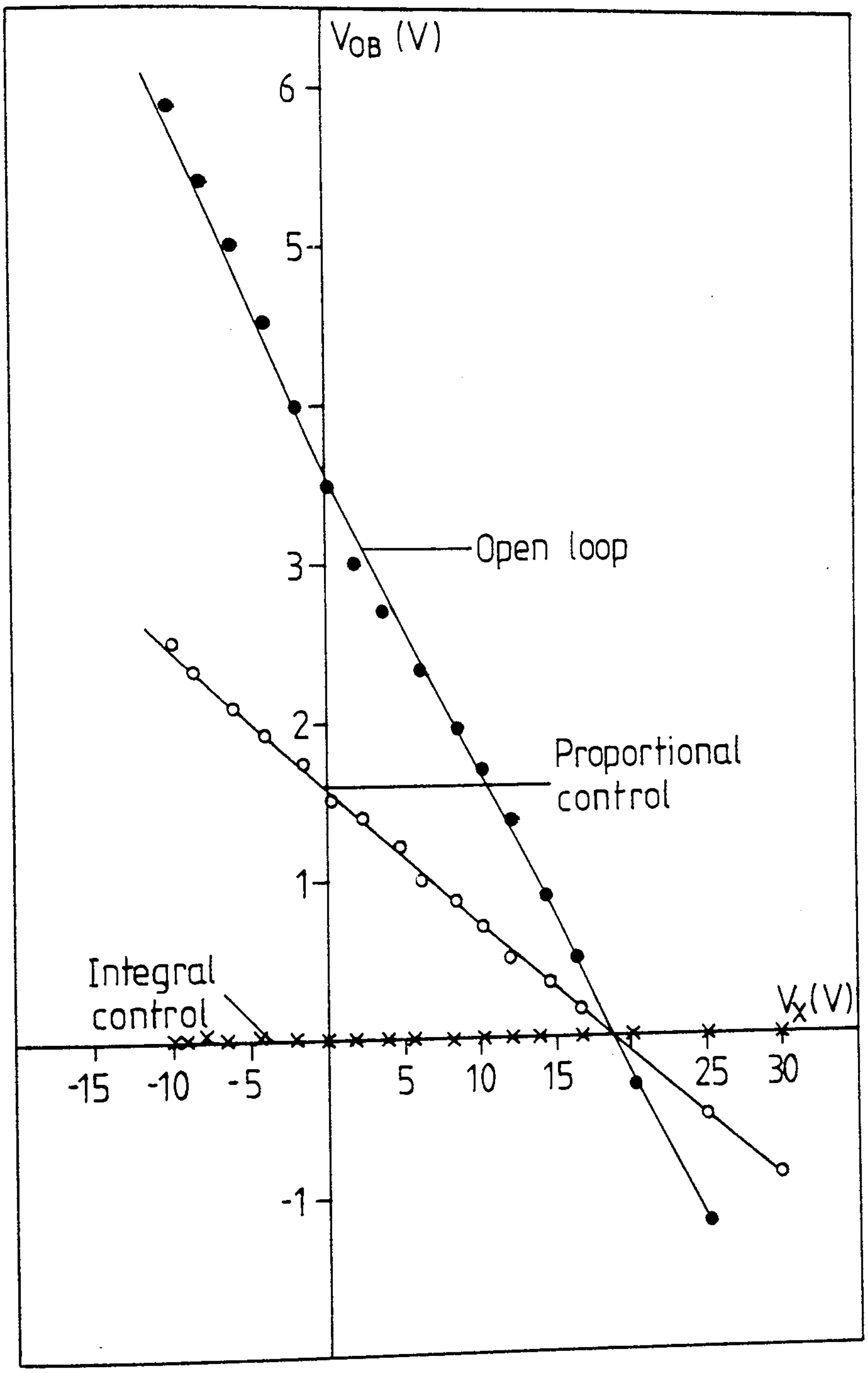

Fig 4.22 D.C. test on the control system at point V_{OB}

are linear with input voltage V_x.

In the proportional control the value of V_{OB} was less than in the open-loop case for various V_x values. Increasing V_x, the feedback voltage V_{OA} also increased and this has eliminated more of the ambient fields which in turn makes V_{OB} less in the proportional control case than in open-loop control.

In the integrator control mode the value of V_{OB} was always zero for all values of V_x, since the integrator automatically provides the necessary feedback voltage to compensate for any variation in the ambient field. It is concluded from the results that when the control system is in the integrator control mode, which is the normal operation of the system, all the external d.c. fields can be eliminated by the control system.

4.6.3.2 Dynamic Tests

(a) Frequency Response Test

An experiment was performed to measure the amplitude response of the overall control system as a function of frequency. A test signal was injected at the external input V_x of the summation amplifier from a signal generator and outputs at points V_{OA} and V_{OB} were measured at different frequencies. The results of the measurements are shown in Fig. 4.23. The control system was optimised to pass the signal at drive frequency and attenuate the signals below this frequency. The signals above the drive

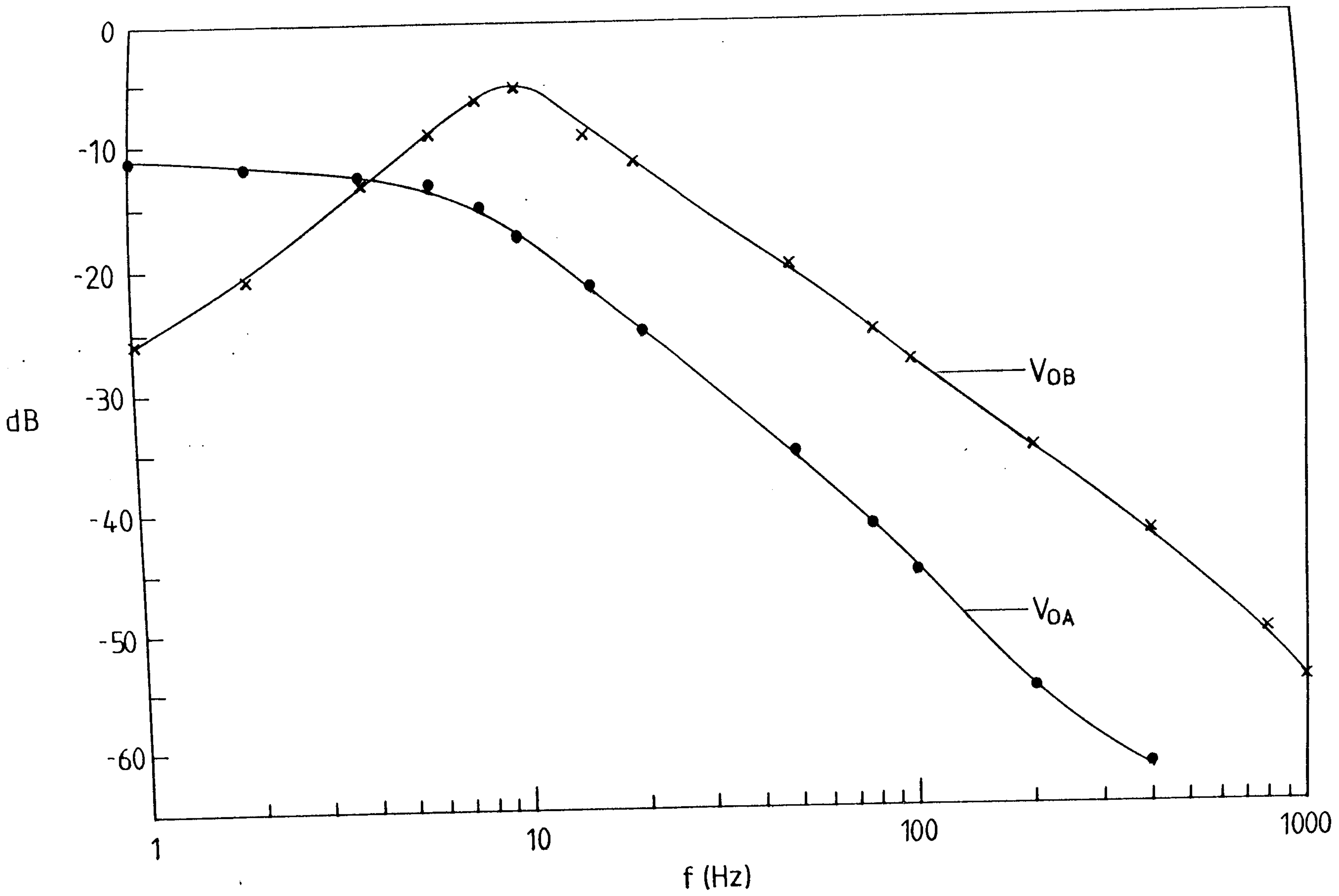

Fig 4.23 Frequency response test on the control system at points V_{OA} and V_{OB}

frequency were also attenuated, as shown in Fig. 4.23, because the natural cut-off frequency of the flux-gate is at about 17 Hz.

(b) Step Response Test on the Control System

The time response of the system was examined in the integrator control mode. A step input V_x was applied at the external input of the summation amplifier and the output at V_{OA} displayed as a function of time. With the time constant of the integrator adjusted to pass the drive frequency without attenuation, it was found that the control system was stable, fast enough for this application and reached the final output value without much over-shooting.

4.7 APPLICATION OF THE SYSTEM IN THE POWER INDUSTRY

The equipment was not in fact tested in the actual power station environment. However, it has been demonstrated that the system could detect ferrous objects by moving these objects within the range of the equipment. Also the electronic design of the detector has taken account of the problems which may arise in the power station environment. The detector is therefore designed for use in the power industry.

Most of the electrical power supplied by the Central Electricity Generating Board is provided by coal fired generating units. It is essential that coal handling plant is both reliable and efficient in order to maintain a high availability of such units. The process of transportation of the coal from the coal mine to the power station often leads to the inclusion of undesirable foreign material such as scrap iron; or other metals amongst the coal. There are two items of power station plant particularly susceptible to damage from the foreign material in the coal: these are the coal feeders and the pulverising mills which they supply.

It is normal practice within the C.E.G.B. to provide electromagnetic separators to remove ferrous metals from the coal. The separators are interlocked to the main conveyor system so that the electromagnet is energised whenever a conveyor system is in operation. The separators remain energised even though no tramp iron is present in the coal. This leads to a considerable waste of energy since the incidence of tramp iron is usually fairly small.

As the coil warms up, its resistance increases. Hence on a fixed voltage supply, the current in the winding drops. This effect is illustrated in Fig. 4.24 which shows how the magnet's temperature increases from switch-on time and causes the current in the windings to be reduced. The efficiency of extraction therefore, decreases considerably. Also, to avoid the risk of fire, the temperature on the separator surface should be kept below 100°C.

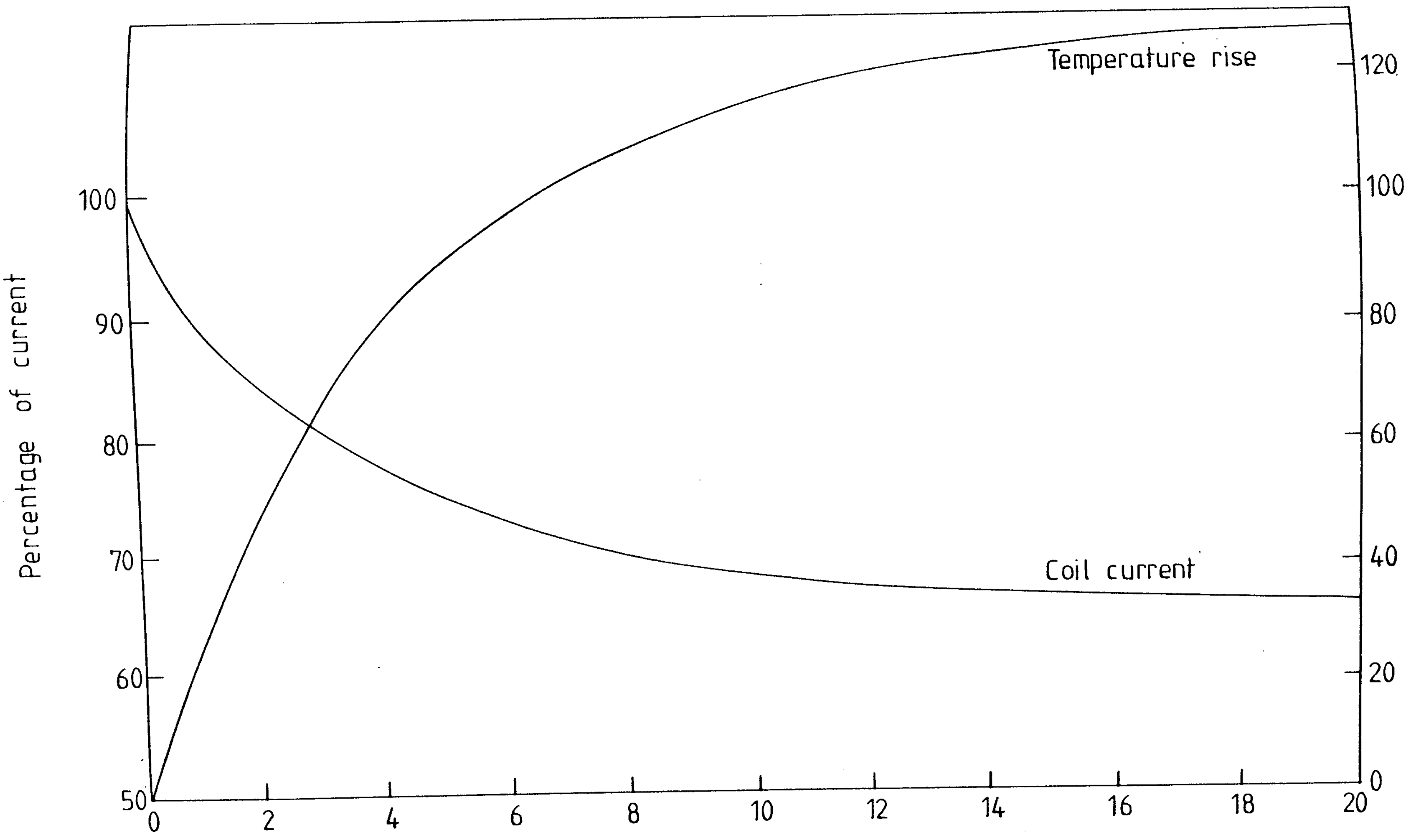

Fig 4.24 Typical temperature and current of a magnetic separator from switching on against the time

The equipment described in this chapter may be used in the power station to detect ferrous metal objects in the coal and provide a control signal to switch the separator on only when required. This increases the efficiency of the separator, because it remains cooler than it would under continuous operation. The overall saving in power is considerable since the separator is only on for very short periods. As the separator remains cool, there is, therefore, no need for further cooling, as is normally necessary in the case of the permanently energised separator.

Because the current in the separator is only required for short periods it is possible to design the switchable separator with a thinner gauge of wire than is used in the present separator. This means that the weight of the copper and size of the separator can both be reduced. The cost would, therefore, be less than that of the currently available electromagnetic separator.

4.8 SUMMARY

In this chapter, the design and practical development of a ferrous metal detector using a flux-gate magnetometer has been described in detail. The equipment was developed to detect extraneous ferrous metals in coal conveyors in the power industry. A brief background description of the flux-gate magnetometer and its principle of operation have been included in the chapter. The theoretical principles on which the operation of the system is based were discussed. The advantages which may be obtained by using the equipment in the power industry were also discussed.

Chapter Five

The theoretical basis of the ferrous and non-ferrous equipment design

5.1 INTRODUCTION

Magnetic field generating sources and electromagnetic phenomena in the conductors have been discussed in Chapter 3. This chapter outlines the theoretical basis on which the prototype equipment was developed. The theoretical principles of the detection and discrimination of ferrous and non-ferrous materials are discussed in this chapter. The principles involved in object location are also described.

Production of a large current in the electromagnetic loop for a given applied voltage is an important factor which can be enhanced by good coil Q. It is however, hindered by the self-capacitance of the loop. The dimensions of the loop will be dictated by the dimensions of a specific conveying system. Loop self-capacitance , however is mainly dependent upon inter-turn spacing. The self-capacitance of the loop is discussed in section 5.2.1.

The theoretical analysis of the phase-sensitive detector which is used to demodulate the signal produced by the presence of a metallic object and to detect the different phase-shifts caused by ferrous and non-ferrous objects is given in section 5.3.

The sensitivity and accuracy of the detector are considered in section 5.7. The output of the receiving coil has been calculated for a simplified model of the system to confirm the experimental measurements of output of the receiving coil. The agreement between the theory and experimental results demonstrates that the equipment design was based on correct principles.

5.2 SELF-CAPACITANCE AND INDUCTION FIELD ENERGY OF THE ELECTROMAGNETIC LOOP

5.2.1 Self-Capacitance of the Loop

Large magnetic field strengths are necessary for good detector performance and this implies large coil currents for a given applied voltage. Large currents can be obtained by careful tuning of the coils. A high Q value for the receiving coil is also necessary since it magnifies the signal amplitude, increasing the overall system sensitivity and range of detection. This is discussed in greater detail in Chapter 6.

The coil Q is reduced by self-capacitance which provides a shunt path for currents and decreases the energy stored in the magnetic field. The loop coil is likely to exhibit considerable capacitance between turns and to ground .

In electrostatic or quasi-static cases, the usual method of calculating the capacitance of two long parallel conductors is to assume a conductor charge, evaluate the resulting electric flux density $\bar{D}$ and electric field strength $\bar{E}$ and to perform an appropriate integration to solve for potential at a point. Finding the potential between two points of interest and eliminating the original charge gives the capacitance per unit length between the conductors (34,48).

The capacitance calculation for two long conductors is presented here since it forms the basis of self-capacitance calculations for loop coils. Considering the two long conductors shown in Fig. 5.1, the electric flux density due to a single long conductor at a distance r is:

$$D = \frac{Q_A}{2\pi r} \qquad (5.1)$$

and

$$E = \frac{Q_A}{2\pi\varepsilon_o r} \qquad (5.2)$$

where Q_A is the charge per metre on conductor A. The potential difference between two points A and B is given by the line integration along any path between them:

$$V_{AB} = \int_A^B \frac{Q_A}{2\pi\varepsilon_o r}\, dr \qquad (5.3)$$

$$V_{AB} = \frac{Q_A}{2\pi\varepsilon_o} \log_e \frac{B}{A} \qquad (5.4)$$

The total capacitance per metre is given by:

$$C = \frac{Q_A}{V_{AB}} = \frac{2\pi\varepsilon_o}{\log_e B/A} \tag{5.5}$$

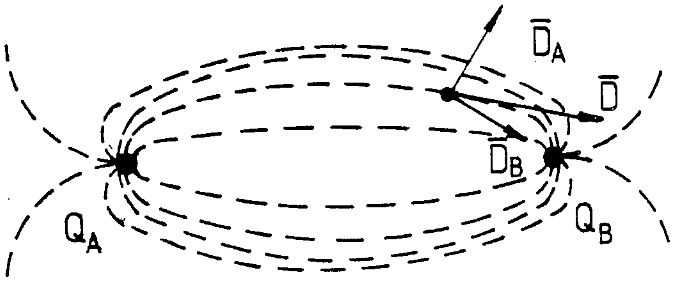

Fig 5.1 Two long conductors in free space.

In general, where a greater number of conductors is involved, a similar process may be adopted, using a matrix solution, to consider all inter-turn capacitances and capacitances to ground(35). The field electromagnetic loops used in this work can be considered as quasi-static because of their size and operating frequency. The loop may be regarded as N parallel conductors. By adopting a similar process of two parallel conductors and using a matrix solution, the total self-capacitance of the loop can be calculated(29). The self-capacitance of the practical loops used in this work were not calculated theoretically, but was assessed by tuning the loop at a range of frequencies and plotting $1/f_o^2$ against the tuning capacitor. The experimental assessment of the self-capacitance is described in section 6.2.1. From the self-capacitance assessment curve of a given loop, a chioce of operating frequency was made which avoided the self-resonance of the coil.

5.2.2 Energy Storage in the Magnetic Field of the Loop

The purpose of the electromagnetic loop is to store energy in the adjacent induction field. The energy stored in a single lumped inductance is given by:

$$W = \frac{1}{2} LI^2 \tag{5.6}$$

where

L is the inductance of the transmitting loop

I is the drive current through the loop

The value of the square loop inductance can be found using the following equation:

$$L = \frac{2\mu_o bN^2}{\pi} \log_e \left[\frac{2b}{a(1+\sqrt{2})} - 0.335\right] \tag{5.7}$$

where

μ_o is the free space permeability

b is the square loop side

N is the number of turns of the loop

a is the radius of the conductor of the loop.

The derivation of equation (5.7) is given in detail in Reference (29).

The total energy stored in the magnetic field is given by equation (5.6). The presence of the coil self-capacitance means that the value of the useful induction current in the coil is reduced by the amount shunted in the capacitance. The useful portion of the transmitter drive current is therefore:

$$I_t = I_{supplied} - I_{shunt} \tag{5.8}$$

The difference made by the self-capacitance C_o of the coil is immediately seen by considering the series tuned coil current, I_r. With no significant self-capacitance losses:

$$I_r = (1+jQ)I \tag{5.9}$$

where

I is the current without tuning.

If the coil exhibits significant self-capacitance C_o, then the modified resonant current I_{Kr} is:

$$I_{Kr} = \frac{(1+jQ)I}{(1+j\omega C_o R)} \tag{5.10}$$

The induction field energy can be expressed in terms of the modified current and loop inductance as follows:

$$W = \tfrac{1}{2}LI_{Kr}^2 = \frac{I_{Kr}^2 \mu_o b N^2}{\pi} \log_e\left[\frac{2b}{a(1+\sqrt{2})} -0.3358\right] \tag{5.11}$$

It can be seen from the foregoing analysis that the self-capacitance of the loop reduces the energy stored in the induction field of the loop and hence the sensitivity and range of the overall detector. In practical development of the detector, the operating frequency was chosen so that the effects of the self-capacitances of the loops used in this work were insignificant.

5.3 THEORETICAL ANALYSIS ON THE PHASE-SENSITIVE DETECTOR

The phase sensitive detector was used to detect the amplitude and phase of the signal produced by the presence of an object. As shown in Fig. 5.2.(a), the phase-sensitive detector compares the phase of the input signal with a reference signal which is of the same frequency as the signal to be measured. The effect of such a phase-sensitive detector on both synchronous and asynchronous (noise) input signals are shown in Fig. 5.2.(b). Two important features are readily seen from the characteristic of the phase-sensitive detector.

(i) When the signal input and reference input have the same frequency and are in phase, the phase-sensitive detector output gives the average amplitude of the signal. A phase difference between the signal and the reference affects the output value. In particular a phase shift of 90° brings the output to zero, while a phase difference of 180° results in a full value but negative output.

(ii) When the signal and reference inputs are not at the

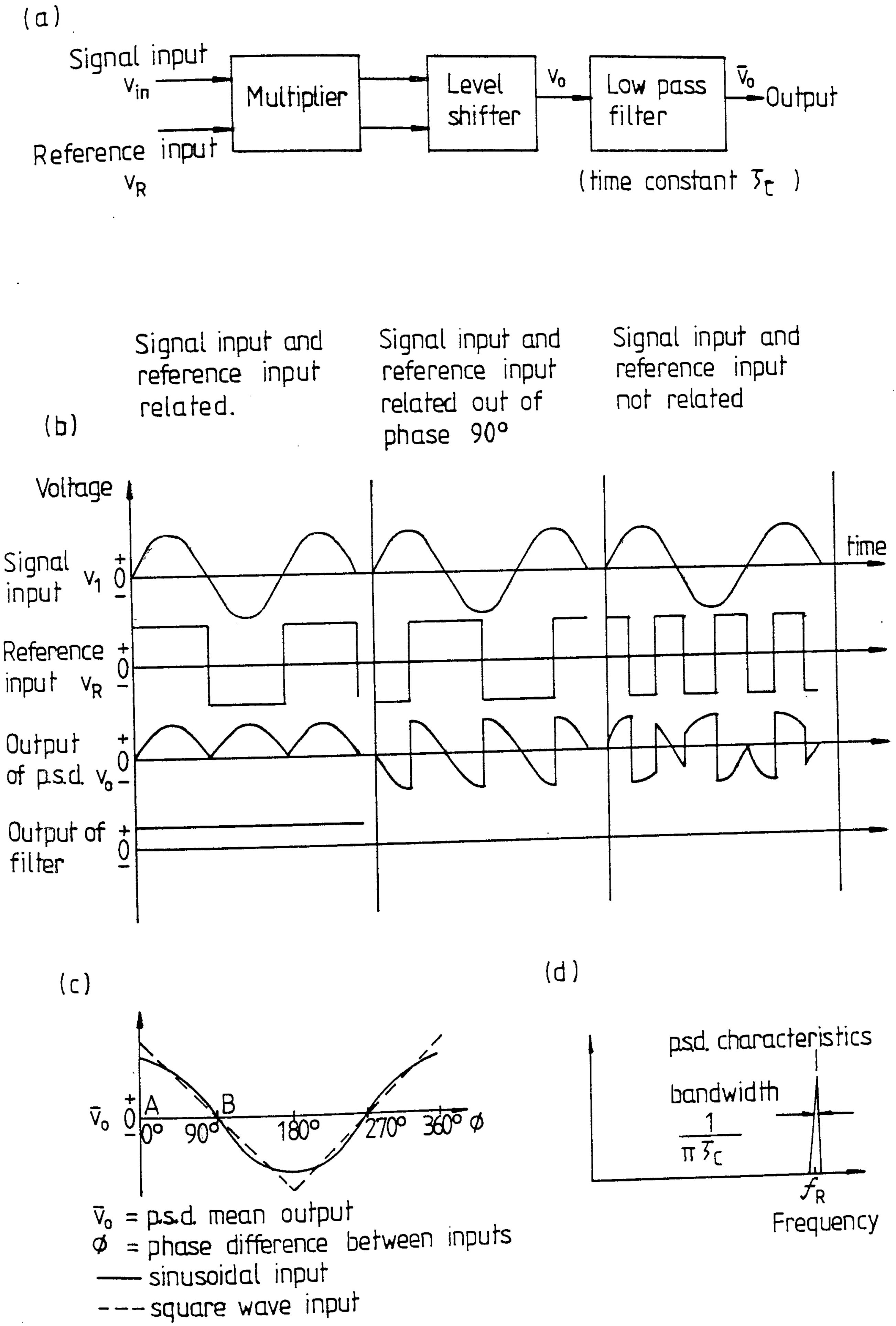

Fig 5.2 (a) Block diagram of the phase sensitive detector
(b) Typical input and output waveforms of the psd
(c) Static characteristic of the p.s.d.
(d) Frequency response of the p.s.d.

same frequency, then the average value of the output is zero, provided a sufficiently long time is taken to establish the average.

The output v_o of the multiplier is the product of the signal input v_1 and the reference input v_R ; that is $v_o = v_1 \times v_R$. The normal reference input v_R is a square-wave of period T_R . This waveform can be described as a superposition of sinusoidal components. The dominant component is at the fundamental angular frequency $\omega_R = \frac{2\pi}{T_R}$. All odd harmonics of this frequency are also present in the reference signal, the amplitude of these terms being inversely proportional to the harmonic number. For simplicity, we consider here only the effect of the fundamental to investigate the behaviour of the multiplier. Hence, $v_R = v_R \cos\omega_R t$, where $\omega_R = 2\pi f_R$ and f_R is the reference frequency. If the signal input to the multiplier is considered to be, $v_1 = V_1 \cos(\omega_1 t + \phi)$, then the multiplier output signal v_o is therefore given by$^{(49)}$:

$$v_o = v_1 v_R = V_1 V_R \cos\omega_R t \cos(\omega_1 t + \phi) \qquad (5.12)$$

If the signal and reference input are synchronous and at the same frequency, then:

$$v_o = V_1 V_R \cos(\omega_R t+\phi) \cos\omega_R t \qquad (5.13)$$

$$= \frac{1}{2} V_1 V_R \left[\cos(2\omega_R t+\phi) + \cos\phi\right] \qquad (5.14)$$

and the average output voltage $\bar{v}_o$ is:

$$\bar{v}_o = \frac{1}{2} V_1 V_R \cos\phi \qquad (5.15)$$

For given amplitudes of the two inputs in the equation (5.14), the output varies with the phase difference between the inputs. The output is positive maximum for $\phi=0^o$ and it reduces as ϕ increases as shown in Fig. 5.2.(c). At $\phi=90^o$, the output is zero. Further increase in ϕ causes the output to increase in negative direction and becomes maximum when $\phi=180^o$ and so on. The phase-sensitive detector also acts as a band-pass filter. The improvement in the signal-to-noise ratio depends on the bandwidth of the filter and the distribution of the noise. The bandwidth of the phase-sensitive detector is $B = \frac{1}{(\pi\tau_c)}$, where τ_c is the time constant of the output low-pass filter, and is centered about the reference frequency f_R as shown in Fig. 5.2.(d). The effective Q of the filter is $Q = f_R/B = \pi\tau_c f_R \simeq 3\tau_c f_R$. The phase-sensitive detector extracts the signature of the metallic object movement within the detection range of the equipment from the amplitude modulated signal and detects the phase difference between the signal and reference inputs. Since the demodulated output of the phase-sensitive detector gives a trace of the travelling object on the conveyor belt, this feature was used to determine the position of the object from the edge of the conveyor belt.

It was mentioned earlier that the bandwidth of the phase-sensitive detector depends on the time constant of the output low-pass filter (τ_c). The speed of response of the system to the movement of the metallic object on the belt also depends on τ_c. An optimum choice, therefore, exists for the speed of response for a given speed of the belt and the bandwidth of the system. The practical optimisation process is described in more detail in section 6.3.1.

5.4 METAL DETECTION PRINCIPLES

5.4.1 Non-Ferrous Metal Detection

A square loop electromagnetic coil was used for the field generating source in the ferrous and non-ferrous detector for the reasons explained in section 3.5. If a metallic target enters the field of the coil, it penetrates the object and causes eddy currents to be induced in the metal. The eddy currents in turn produce their own electromagnetic field which radiates in all directions. A portion of this field is detected by the receiving coil which is balanced against the primary field. The conveyor belt passes between the transmitting and receiving coil since this gives maximum sensitivity.

The loop coil generates a three-dimensional field and it is this field which penetrates the metal. According to the theory given in Chapter 3, the induced eddy current density in the metal may then be found by Maxwell's equation as follows:

$$\nabla \times \bar{H} = \bar{J} \tag{5.16}$$

where $\nabla \times \bar{H}$ is the curl of the magnetic field strength acting on the metal, and

$\bar{J}$ is the induced eddy current density in the metal.

For the three-dimensional case, the eddy current density is(43,50):

$$\bar{J} = \left(\frac{\partial H_z}{\partial y} - \frac{\partial H_y}{\partial z}\right) a_x + \left(\frac{\partial H_x}{\partial z} - \frac{\partial H_z}{\partial x}\right) a_y$$

$$+ \left(\frac{\partial H_y}{\partial x} - \frac{\partial H_x}{\partial y}\right) a_z \tag{5.17}$$

where a_x, a_y and a_z are the unit vectors along the x, y and z directions, respectively. The analytical solution of the above equation is highly complicated and it is therefore more convenient to solve the equation numerically to obtain the eddy current distribution in the metal.

If the dimensions of the metallic object are greater than the penetration depth of the metal, the magnetic field reduces to a two-dimensional field on the surface of the metal. For the x and y components of the field on the surface of the metal, respectively H_x and H_y, the induced eddy current density is given by:

$$J_z = \frac{\partial H_x}{\partial y} - \frac{\partial H_y}{\partial x} \tag{5.18}$$

Equation (5.18) needs to be solved numerically to determine the induced eddy current for a given size of the metal. However, the output of the phase-sensitive detector was measured experimentally for different types, shapes, sizes and positions of the metal, and some of the results are given in Chapter 6.

The net primary field acting on the metal may be regarded as being parallel to the surface of the metal at the point of consideration within the region of the field in the metal. This means that the net field at each individual point within the metal may be regarded as a one-dimensional field with a specified direction.

According to the theory given in Chapter 3, the induced eddy current in the metal for a one-dimensional field depends on the primary magnetic field strength. The induced currents are therefore also dependent on the primary magnetic field strength and hence the sensitivity and range of detection of the equipment. To obtain a good detector performance, the excitation field was maximised for a given size and number of turns of the square loop eletromagnetic coil by tuning it to resonance.

Since the permeability of non-ferrous metal is approximately equal to that of free space ($\mu_o = 4\pi \times 10^{-7}$ H/m), only the eddy current effect is significant. The detection of non-ferrous metal was therefore based on this principle.

5.4.2 Ferrous Metal Detection

Ferromagnetic materials have permeabilities significantly greater than that of free space. When this type of metal enters the detection zone of the equipment, eddy currents are induced in the metal as explained in section 5.4.1. However, it also intensifies the field strength of the appropriate side of the loop due to the high permeability of the metal. The receiving coil therefore detects the combination of the intensifying effect and the eddy current field. The contribution of each of these components to the combined effect depends on the size, shape, orientation and position of the object within the field. The magnitude of the resultant field from these two components cannot be calculated analytically even for a one-dimensional field. However, the magnitude of both effects depends on the magnetic field strength which acts on the metal. As in the case of the non-ferrous metal, the output of the receiving coil due to the presence of the ferrous objects also depends on the transmitting field strength and hence the sensitivity and range of the detection of the instrument.

It should be noted that the ferrous metals have been regarded magnetically linear, since the excitation field strength has been kept below the knee-point on the normal B-H curve of the most common ferromagnetic materials.

5.4.3 Selection of the Operating Frequency

The dependence of the output on the excitation frequency was investigated by considering the mutual coupling between the object and transmitting loop and between the object and receiving coil. The representation of the coupling is shown in Fig. 5.3.

From the circuits of Fig. 5.3:

$$j\omega M_1 I_1 + j\omega L I_2 + I_2 R = 0 \tag{5.19}$$

$$j\omega(M_1 I_1 + L I_2) + I_2 R = 0$$

$$M_1 I_1 >> L I_2$$

Then

$$j\omega M_1 I_1 + I_2 R = 0 \tag{5.20}$$

$$V_3 = j\omega M_2 I_2 \tag{5.21}$$

putting the value of I_2 from equation (5.20) into (5.21) V_3 becomes:

$$V_3 = -j\omega M_2 . \; j\omega \frac{M_1 I_1}{R} \tag{5.22}$$

For a given size, type and position of the object and constant driving current we have:

$$V_3 \propto \frac{\omega^2}{R} \tag{5.23}$$

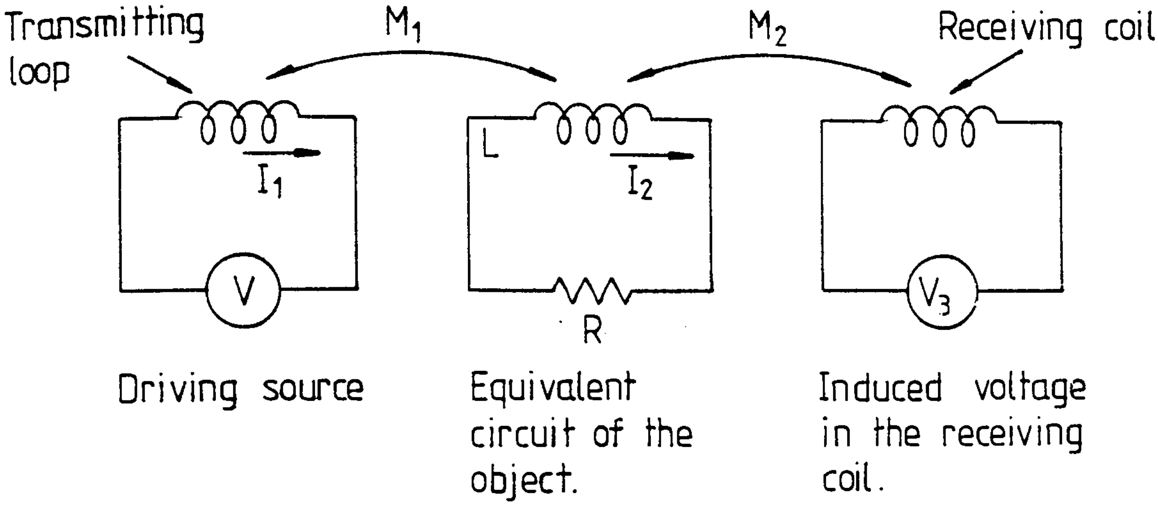

Fig 5.3 The mutual coupling representation between the transmitter - object and object - receiver.

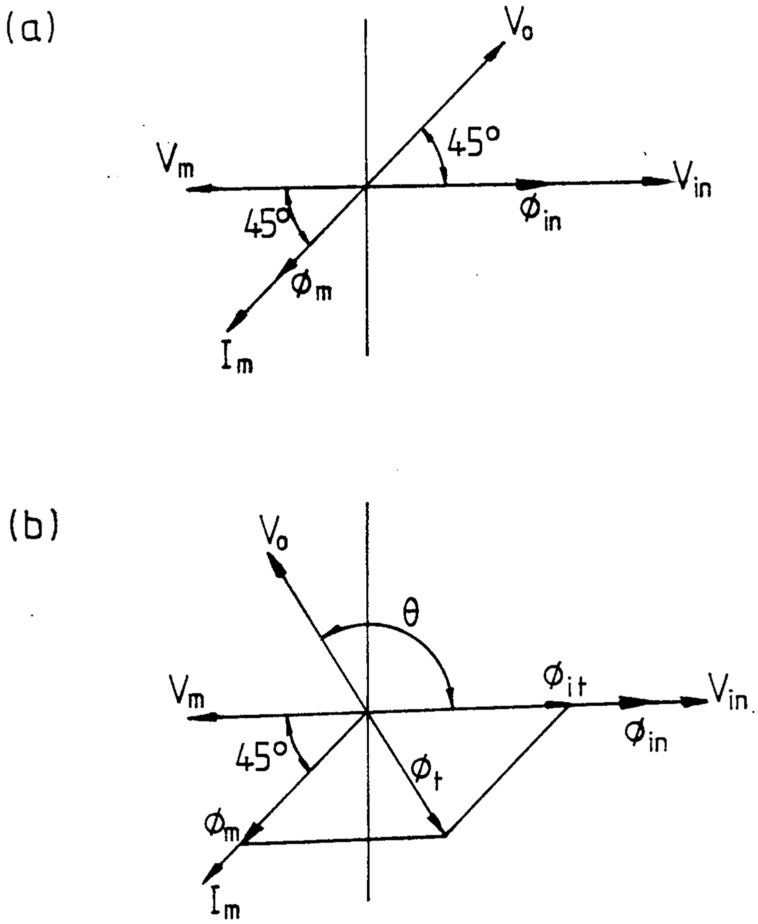

Fig 5.4 The phase relation representation between the drive and output voltages.
(a) for non-ferrous metal
(b) for ferrous metal

But from the theory given in Chapter 3

$$R \propto \frac{1}{\delta} \quad \text{and} \quad \delta \propto \frac{1}{\omega^{\frac{1}{2}}} \qquad (5.24)$$

where δ is the depth of the penetration into the metal and ω is the angular drive frequency.

Therefore,

$$V_3 \propto \omega^{3/2} \qquad (5.25)$$

This equation shows that the output of the receiving coil increases in proportion to the 3/2 power of the drive frequency.

Equation (5.25) is not applicable in the case of ferrous objects since there is an intensifying effect as well as the mutual coupling. Because the depth of penetration decreases with $\omega^{\frac{1}{2}}$, the intensifying effect reduces by the same factor. However, the induced output of the receiving coil is proportional to ω, hence, the overall effect of the increase in frequency on the output due to the intensifying effect is proportional to $\omega^{\frac{1}{2}}$.

Since the output of the receiving coil is due to a combination of both effects, it is not possible to derive an exact equation for the effect of the change in frequency on the output of the receiving coil. From the above discussion it is evident that the output, in general, increases with the increase of frequency in both ferrous and non-ferrous metals.

5.5 DISCRIMINATION BETWEEN FERROUS AND NON-FERROUS OBJECTS

According to the analysis given in Chapter 3, the surface impedance of any magnetically linear conductor subjected to a time varying field is given by:

$$z_s = \frac{(1+j)}{\sigma\delta} \tag{5.26}$$

This impedance is a constant of the material at the given excitation frequency.

From equation (5.26), the surface impedance of the linear conductors thus has a phase angle of 45°. The induced eddy currents which flow through the surface impedance have a similar phase angle, when the induced voltage is taken as the reference. These eddy currents produce their own magnetic field which is then detected by the receiving coil. Thus, the output of this coil has a phase angle different than that of the drive voltage.

Since the ferrous metals are regarded as magnetically linear, for the reason explained in Chapter 3, equation (5.26) is applicable in both ferrous and non-ferrous metal cases. However, in the case of ferrous metal, the net magnetic field produced by the object has a phase angle which is due to the combination of the intensifying effect and eddy current. The value of this phase angle depends on the magnitudes of both the induced eddy current component and the intensifying component. This means that the output of the receiving coil for a ferrous object has a phase angle different than that of the non-ferrous object. The phase relation between the output voltages due to both ferrous and non-ferrous metals and the drive voltage are given in Fig. 5.4.

The parameters given in Fig. 5.4 are as follows:

V_{in} = input voltage
V_m = induced voltage in the metal
I_m = induced eddy current in the metal
ϕ_{in} = primary flux
V_{out} = output voltage
ϕ_{it} = flux due to the intensifying effect
ϕ_m = flux produced by the induced eddy current.
ϕ_t = total flux in the ferrous metal.

As shown in Fig. 5.4, the phase angle of the output voltage for a ferrous object is different than that for non-ferrous metal. This principle was successfully employed in this work to discriminate between ferrous and non-ferrous substances.

5.6 THEORY OF LOCATION OF THE OBJECT ON THE CONVEYOR BELT

The location of the object on the conveyor belt was found in two steps. The theoretical basis for these steps is given in the following two sections.

5.6.1 Determination of the Side of the Conveyor Belt on which the Object Exists

The field analysis of the square loop coil given earlier in the thesis shows that the net fields generated by the coil at each half of the loop are in opposite directions. The geometry of the loop and conveyor belt used in this work was as shown in Fig. 5.5. The position-detecting-coil was placed above the conveyor belt level at a specified height with its axis parallel to the y-axis of Fig. 5.5, and balanced against the fields from each half of the loop. Since the induced eddy current in the metal at a given point is proportional to the field at that point, then the magnetic field of the eddy current in one half of the loop is therefore opposite to the eddy current field in the other half of the loop. The output of the position-detecting-coil when the metal is in one half of the loop is 180° out of phase with the output due to the metal being in the other half of the loop.

The output of the system was measured experimentally for different types, shapes and positions of the object on both sides of the conveyor belt. The results are given in Chapter 6.

An electronic circuit was devised that indicated the side of the conveyor belt on which the metal target was located.

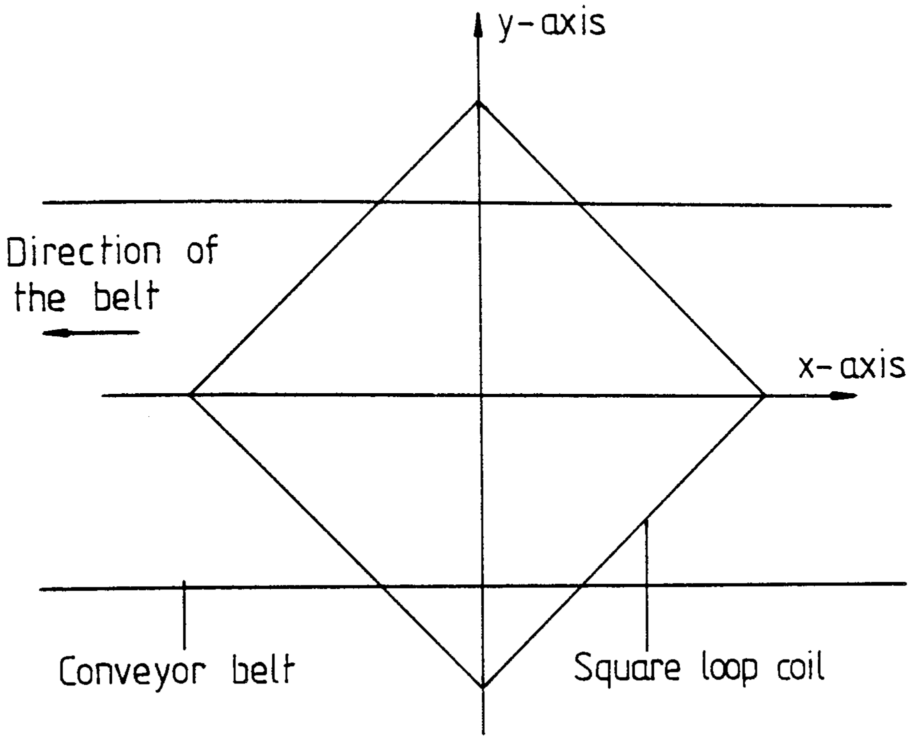

Fig 5.5 The arrangement of the conveyor belt used with the square loop electromagnetic coil.

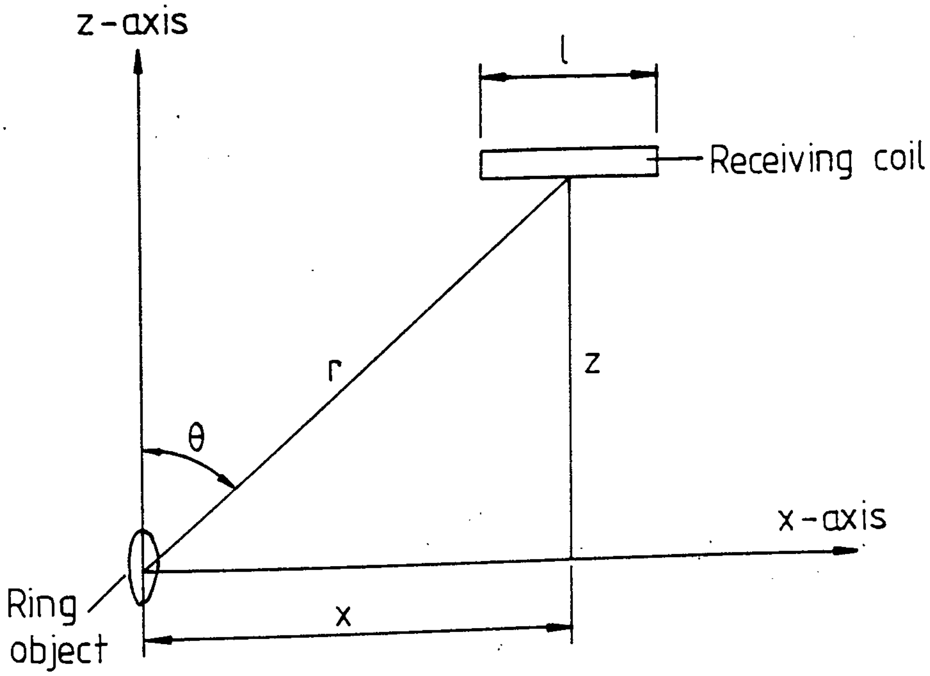

Fig 5.6 The arrangement of the ring object with the receiving coil for the calculation of the output of the receiving coil.

5.6.2 Location of the Position of the Object on the Defined Side of the Belt

It can be seen from the analysis of the loop electromagnetic coil that the field distribution of the coil is well defined by the loop size. Also, the field at the outside of the loop near the conductors is negative maximum, whilst it is positive maximum at the inside of the loop near the conductors. It was also found that the field in one half of the loop is opposite in polarity to the field at the other side of the loop. The eddy current induced in a metal object which enters the field has the same profile as the field, and hence the phase of the signal detected by the receiving coil changes by 180° as the metal passes from the outside to the inside of the loop and also passes from one half to the other half of the loop. The receiving coil of the detector was placed on the top of the belt and just above the position-detecting-coil. The coil was balanced against the primary field with its axis parallel to the x-axis in Fig. 5.5. The coil detects the field parallel to its axis and gives an output which is then processed to indicate the position of the metallic object. The time taken by the metal object to travel from entry into the physical loop to the centre of the loop (y-axis in Fig. 5.5) was measured and then converted into distance to indicate the location of the object from the corner of the loop on the appropriate side of the belt. The technique of measurement and conversion of time to distance are discussed in Chapter 6.

5.7 THE DETECTION PERFORMANCE DEPENDENCY ON THE RECEIVING COIL

5.7.1 Theoretical Calculations of the Output of the Receiving Coil

The eddy currents induced in the metal cannot be calculated analytically for the three-dimensional field and must therefore be solved numerically. Hence the output of the receiving coil cannot be calculated analytically for the three-dimensional primary field. However,the output of the receiving coil was calculated analytically for a non-ferrous ring object at different points along the x-axis as defined in Fig. 5.6 with a ring diameter of 4 cm and the axis parallel to the x-axis.

The transmitting coil is not shown in Fig. 5.6 but in the practical arrangement it was situated below the object level. The photograph given in Chapter 6 shows the detailed arrangement of the system.

The theoretical calculation of the receiving coil was based on the mutual coupling of the field source coil with the object and the object with the pick-up coil. Refering to Fig. 5.3, and equation (5.22), the output voltage of the receiving coil is:

$$V_o = \frac{\omega^2 M_2 M_1 I_1}{R} \tag{5.27}$$

$$M_1 = \frac{\phi_{21}}{I_1} \tag{5.28}$$

$$M_2 = \frac{\phi_{32}}{I_2} \tag{5.29}$$

$$\phi_{21} = \mu_o H_{x'} a_2 \tag{5.30}$$

$$\phi_{32} = \mu_o \mu_r N a_3 \ell H_x \tag{5.31}$$

$$H_x = \frac{I_2 a_2}{4\pi r^3} (2\cos\theta\sin\theta + \sin\theta\cos\theta) \tag{5.32}$$

$$H_x = \frac{3 I_2 a_2 x z}{4\pi (x^2 + z^2)^{5/2}} \tag{5.33}$$

$$V_o = \frac{\omega^2}{R} \frac{\mu_o H_{x'} a_2 N \mu_o \mu_r a_3 \ell 3.x.z}{I_1 (x^2 + z^2)^{5/2}} \tag{5.34}$$

$$V_o = \frac{K H_{x'} \ell x z}{(x^2+z^2)^{5/2}} \tag{5.35}$$

where

ω = Angular excitation frequency

M_1 = Mutual inductance between the field source and object

M_2 = Mutual inductance between the object and receiving coil

I_1 = Excitation current

R = The total resistance of the object

ϕ_{21} = The flux linkage with the object due to the field source

ϕ_{32} = The flux linkage with the receiving coil due to the object.

I_2 = The induced current through the object

μ_o = The permeability of the free space

a_2 = The area of the ring

$H_{x'}$ = The magnetic field strength of the excitation coil as given by equation (3.32).

μ_r = The permeability of the ferrite material

ℓ = The length of the core of the receiving coil

a_3 = The cross-sectional area of the receiving coil.

H_x = The magnetic field strength due to the induced current in the ring object.

All other parameters are as indicated in Fig. 5.6.

K = constant derived from fixed system parameters.

The output was calculated for different lengths and height of the receiving coil from the excitation coil for different positions of the object along the x-axis. The results of the calculations are given in Fig. 5.7 for different lengths of the coil and various positions of the ring, where the distance between the receiving coil and the excitation coil (z) is equal to 20 cm. The calculated outputs at $z = 30$ cm are given in Fig. 5.8. In all these calculations the object was kept at about 5 cm from the plane of the excitation coil. The comparison between the experimental and theoretical results

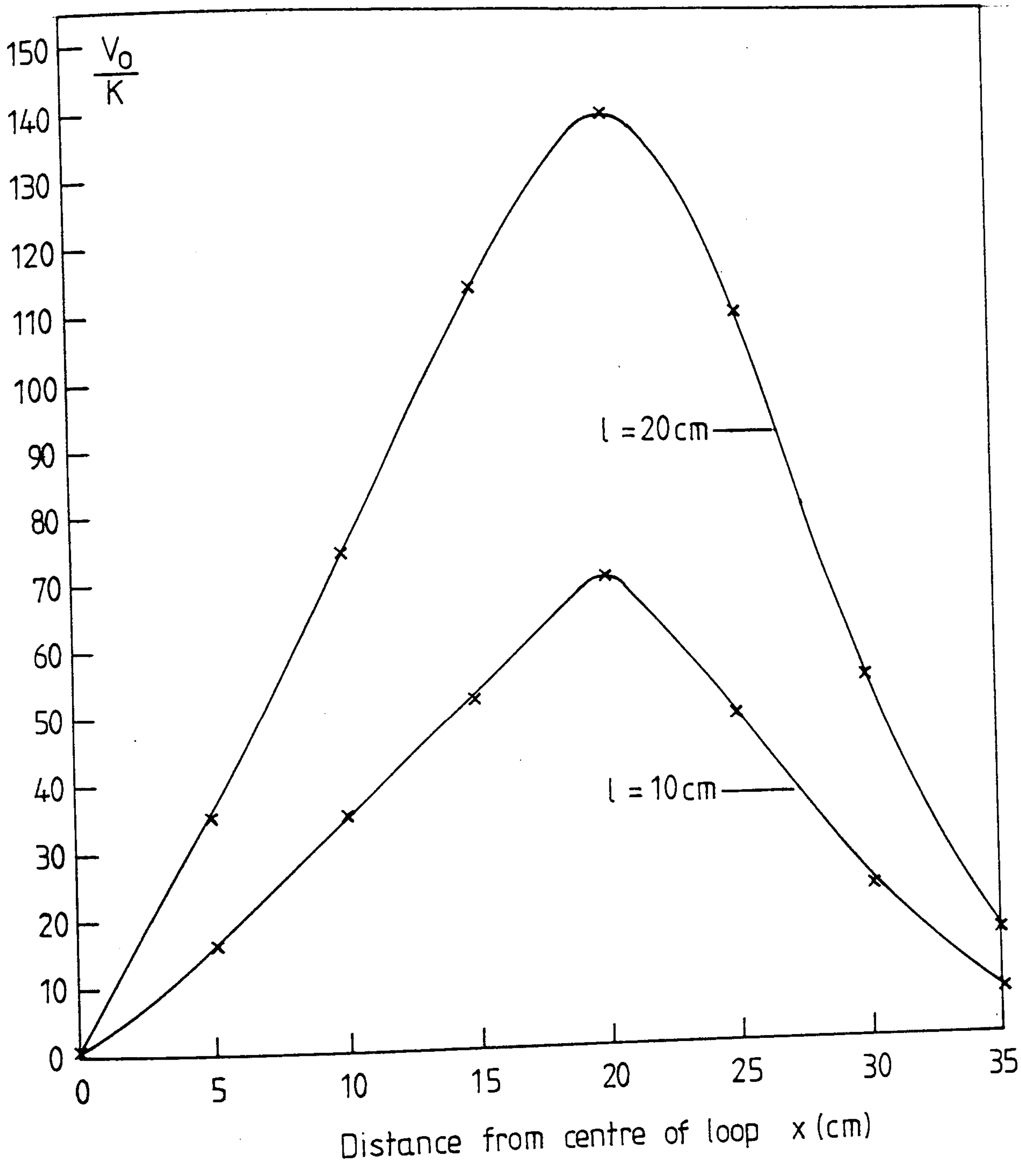

Fig 5.7 The normalized theoretical output of the receiving coil due to moving a ring object along the x-axis for different lengths of the core of the receiving coil at z = 20cm and excitation loop side of 35cm.

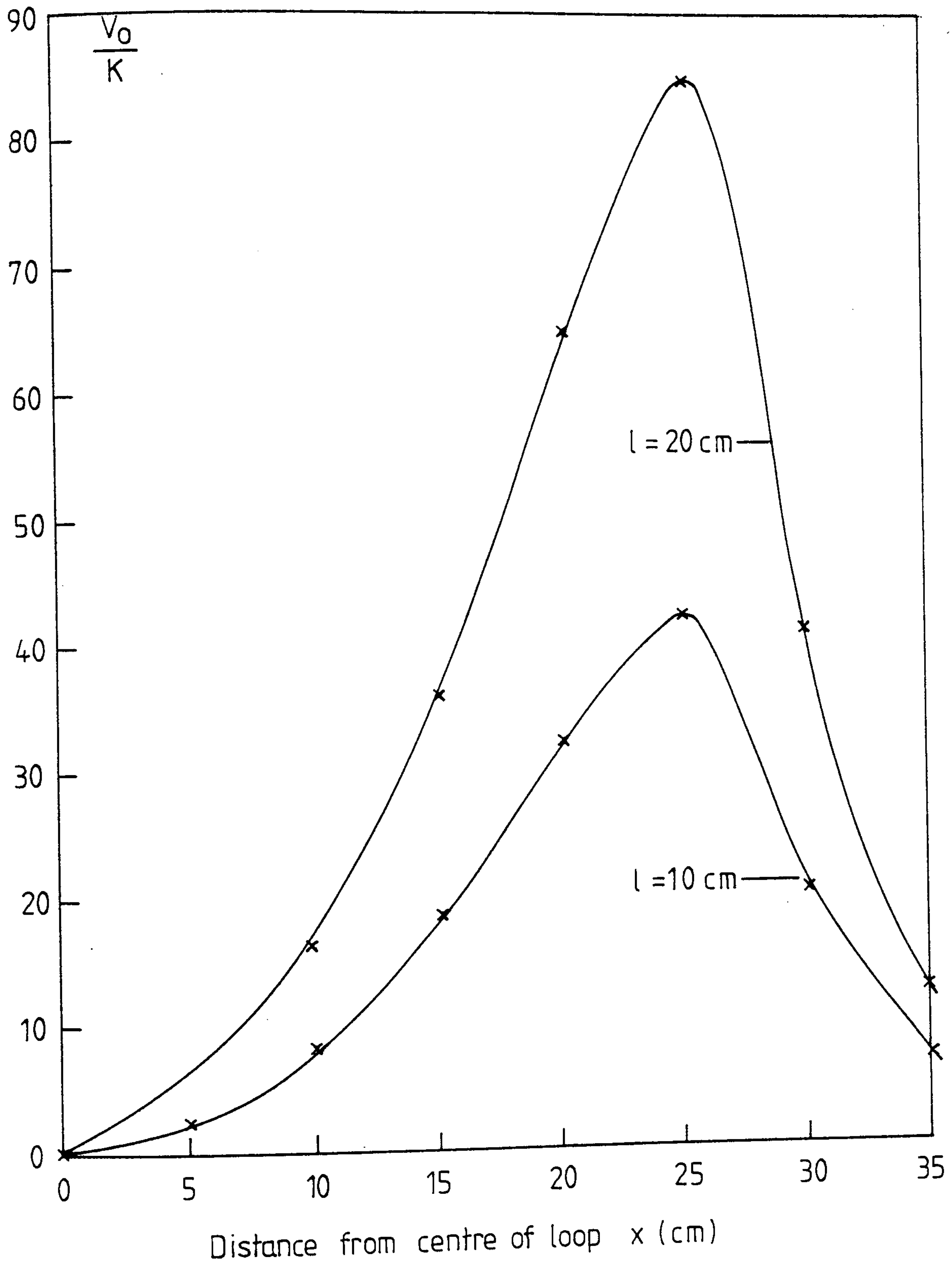

Fig 5.8 The normalized theoretical output of the receiving coil due to moving a ring object along the x-axis for different lengths of the core of the receiving coil at z=30cm and excitation loop side of 35cm.

is given in detail in Chapter 6.

It should be noted that the output of the receiving coil for ferrous objects was not calculated analytically for the reason given in section 5.4.2.

5.7.2 The Sensitivity and Accuracy of the Detection

As explained earlier in this chapter, the current through the transmitting coil can be increased, and hence the sensitivity, by careful tuning of the coil. The tuning of the receiving coil also increases the sensitivity, because the induced voltage of the tuned coil is multiplied by the Q factor of the coil. The self-capacitance reduces the Q of both coils and thus the sensitivity. However, in practice, the self-capacitance of both coils used in this work were kept insignificant by choosing the excitation frequency so that self-resonance was avoided.

This detector has an extremely narrow bandwidth, due to the fact that the receiving coil is tuned for resonance. This characteristic increases the accuracy of the equipment because the coil detects only the fields which are at the excitation frequency and strongly attenuates the fields at all other frequencies. The frequency response characteristic of the ferrite core receiving coil was determined experimentally and is included in section 6.2.2.

The theoretical results obtained in section 5.7.1 show that the output of the detector increases with increasing length of the coil when the other parameters are kept constant.

Thus, the sensitivity of the system increases with the length of the coil. It is also seen from the results that the range of the detection extends over wider areas for the longer receiving coils. This means the accuracy of detection decreases with the length of the coil because it becomes capable of detecting more interference fields from the surrounding regions of the system(14). It can also be seen from the calculations that the amplitude of the detected signal is strongly affected by the distance between the receiving and excitation coils.

However, in practical applications of the equipment a compromise can be made between the sensitivity and accuracy of the detector depending on the length of the receiving coil for a specific conveying system.

Since the flux linkage with the receiving coil is a function of the permeability of the core material, the use of a ferrite core increases the flux linkage and hence the sensitivity of the detector. The accuracy of the system also increases, because by using a ferrite cored coil, the physical cross-sectional area of the coil can be reduced considerably. In turn this may decrease the linkage of the interference field with the coil.

5.8 SUMMARY

The theoretical basis for the ferrous and non-ferrous detector design have been discussed in this chapter. The principles of metal detection, discrimination and location of the metallic object on the conveyor belt have been given in detail. The dependency of the detector performance on the self-capacitance of both transmitting and receiving coils was investigated. The effect of the dimensions, core material and tuning of the receiving coil on the sensitivity and accuracy of the equipment has also been considered.

Chapter Six

practical development of the ferrous and non-ferrous detector and experimental tests

6.1 INTRODUCTION

This chapter describes the equipment which was designed to detect ferrous and non-ferrous metal objects within materials carried on conveying systems. Details of the development of the excitation loop coils, the receiving coils and the detection equipment are given.

The experimental results obtained from practical tests on the equipment are also given.

6.2 ELECTROMAGNETIC COILS

The performance of a detector is controlled by many different factors. The transmitting and receiving coils are among the important parts of the system. Electromagnetic coils are required to convert electrical currents or voltages into magnetic fields, or vice-versa. Good performance for a transmitting coil is regarded as the production of large magnetic field strengths from a given driving current, while sensitivity to low level magnetic fields is the criterion for a successful receiver.

The performance of any such coil, large or small, is considerably enhanced by a high value of magnification factor Q. If the coil is a large air-cored loop transmitter, tuning will cause the coil current to be multiplied by the coil Q factor. In the case of the receiver, the high value of Q has the effect of magnifying the coil induced voltage from a particular magnetic field strength.

Voltages induced in the receiving coils may be regarded as a voltage generator in series with the coil inductance. The coils which are used to detect the fields associated with the metal targets can therefore be considered in the same way as the series driven transmitter. The sketch below applies to both types of coils.

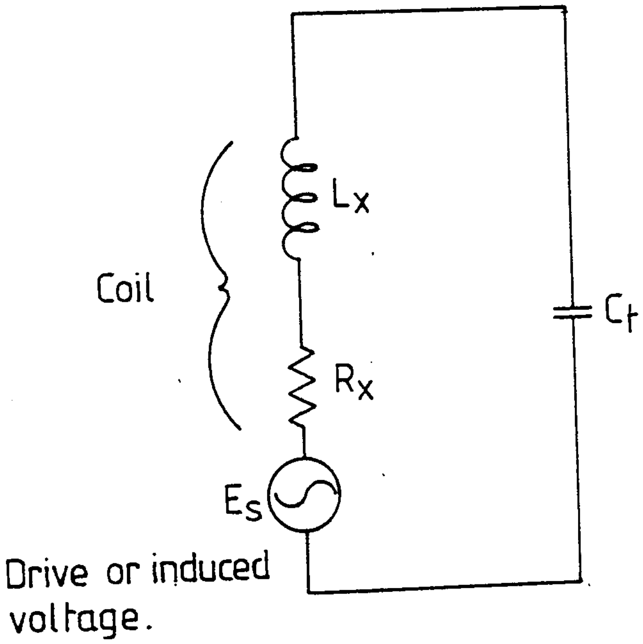

Fig 6.1 The transmitting and receiving coil equivalent circuit diagram.

An elementary analysis shows that the Q of the tuned transmitter directly increases the loop current(51) and hence the magnetic field intensity produced. The Q of the receiving coil directly increases the amplitude of the voltage appearing across the coil due to a particular magnetic field strength, and hence increases the sensitivity and range of the detection of the equipment.

Theory shows that an increase in the loop coil area improves the transmission performance. In the case of large air-cored loops, the effective area is equivalent to the geometric area. The effective area and hence the detection sensitivity of smaller coils is related to the relative permeability of ferrite core. This fact makes the use of high relative permeability ferrite cores a necessity for physically small coils.

To design an induction coil for a specific task, consideration has to be given to conductor type, size, cross-section and to the coil structure.

6.2.1 Loop Electromagnetic Coils

Using large loop areas increases the sensitivity and range of the detector. On the other hand, the accuracy of the detector decreases because the system encompasses greater physical dimensions. Also, the large loops have high self-capacitance between the windings of the coil which provides a shunt path for a portion of the inductor current. However, in practical implementations of the detector, the loop size is determined by the dimensions of a specific conveying system and is thus out of the designer's control.

If the inductor self-capacitance becomes comparable with the tuning capacitor at the chosen frequency, then the shunt path for the inductor current will be significant, and the energy stored in the induction field will be greatly reduced. The overall resistance of the loop increases with increasing dimensions of the loop, causing the current to be reduced for a given drive voltage. The skin effect on the current flow in the conductors of the loop increases coil resistance causing the current to be reduced as the operating frequency is increased. This effect can be minimised by using stranded wires to form the windings.

In this work several loops have been wound using different types of wires and number of turns, with various dimensions of the loop. The self-capacitance assessment of the loops was achieved by driving the loops with different frequencies and tuning them to resonance. The self-capacitance of each loop was assessed from the plot of $\frac{1}{f_o^2}$ against the tuning capacitance(29). The assessment curves for the various practically wound loops are given in Fig. 6.2. From the results shown in the previous graph, it can be seen that the self-capacitance, O-A intercept increases with the increasing dimensions and number of turns of the loop. Also, it can be seen that the self-capacitance of a loop with the same dimensions and number of turns formed from stranded wire is less than that of the copper enamelled solid wire of the same cross-section. This means the use of stranded wire for the loop windings maximises the Q factor of the coil. This type of loop is therefore recommended for use in actual applications of the detector because, according to the theory given in Chapter 5, increasing the Q factor of the

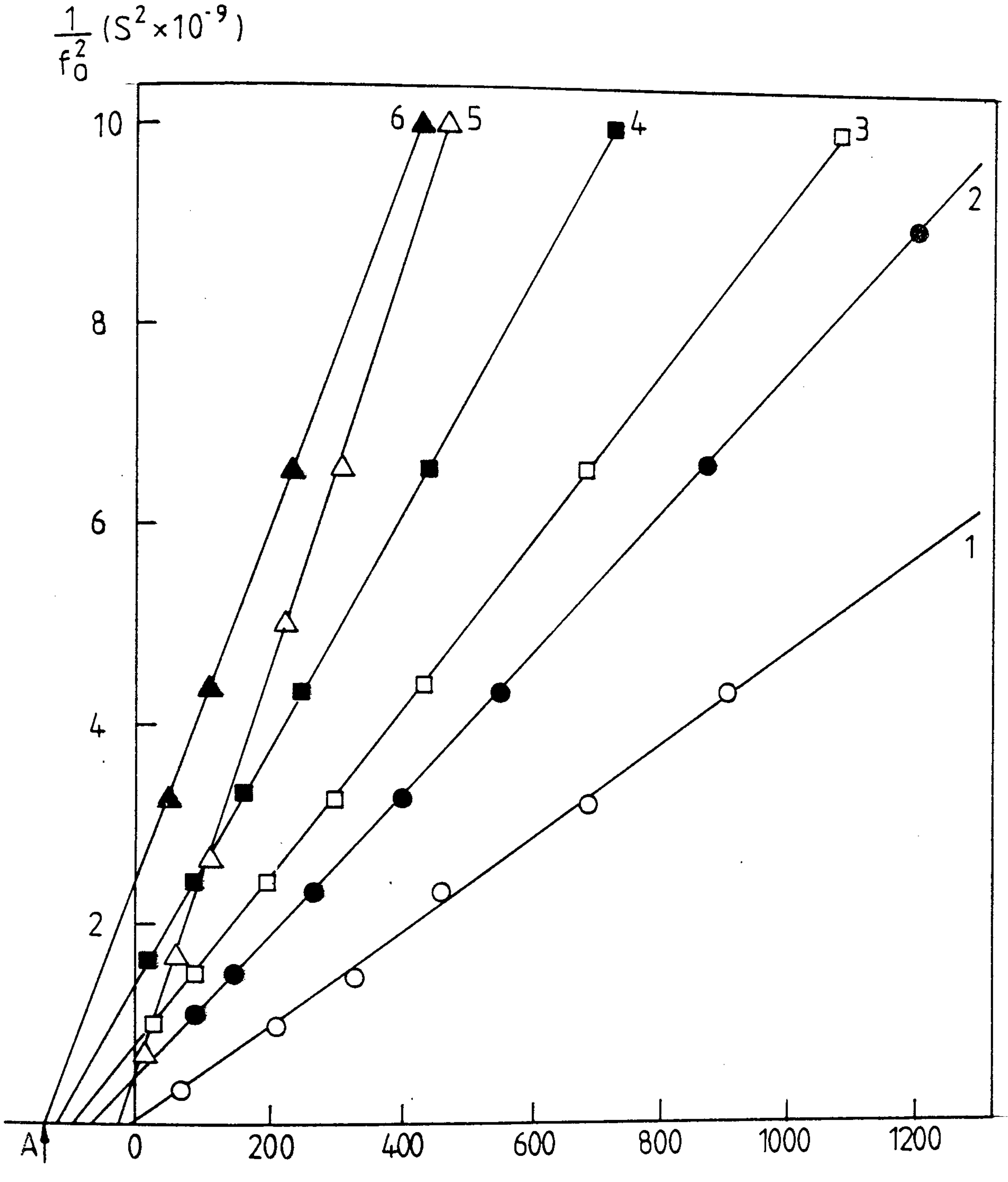

Fig 6.2 The self-capacitance assessment curves of the practically wound square loops.

(1) Loop side 30cm SWG 16 n = 10 turns.
(2) Loop side 30cm SWG 16 n = 20 turns.
(3) Loop side 60cm SWG 16 n = 10 turns.
(4) Loop side 35cm SWG 16 n = 20 turns.
(5) Loop side 35cm stranded wire with diameter of 2mm n = 20 turns.
(6) Loop side 60cm SWG 16 n = 20 turns.

At coil resonance $2\pi f_0 L = \frac{1}{2\pi f_0 (C_t + C_0)}$ $1/f_0^2 = 4\pi^2 L (C_0 + C_t)$

Gradient = $4\pi^2 L$ 0-A Intersect = C_0 = Self-capacitance.

coil maximises the sensitivity and range of detection of the equipment.

However, to cover the complete conveyor belt width of about 42 cm used in this work, a square loop of 35 cm side length was wound using 20 turns of stranded wire of 2 mm diameter. From Fig. 6.2 the self-capacitance of this loop is about 25 nF and the self-resonance frequency is about 55 kHz. Normally, the operating frequency of such a system is chosen to be about one fifth of the self-tuning frequency(29). The excitation frequency in this work was therefore selected to be about 12 kHz. At this operating frequency the Q value of the loop used was about 30.

For simplicity, all the loop coils mentioned so far were wound with negligible inter-turn spacing. The loops could be formed with some inter-turn spacing and this could reduce the self-capacitance allowing higher excitation frequencies to be used. If large inter-turn spacings are used to reduce the self-capacitance, the inductance of the coil is also reduced. To maximise the Q factor of the coil, an experimental compromise has to be made between bunched conductors and the loss in inductance.

The power amplifier shown in Fig. 4.9 was employed in both detectors to drive the excitation loop with the required current.

6.2.2 The Receiving Coils

The use of high permeability core material increases the effective area of the coil and hence the flux linkage with the receiver. The effect of the permeable material on the performance of the receiving coil was dealt with in Chapter 5. In this work, the receiving coils were wound with high permeability ferrite cores. The cores consisted of 20 cm long, 3 cm diameter ferrite bars. Each coil consisted of 600 turns of SWG30 copper enamelled wire. At an operating frequency of about 12 kHz, the Q factor of the receiving coils was about 120. With this Q value, the coil, can be tuned to have a very narrow receiving bandwidth with large magnification of the pick-up voltage. The frequency response characteristic of the receiving coils is shown in Fig. 6.3. The receiving bandwidth of the coils is about 100 Hz. This feature increases the accuracy of the system, by attenuating unwanted outband signals.

The output of the pre-amplifier for copper and iron objects size (1×2×3 cm) was measured at different frequencies with the receiving coil balanced against the fields of the excitation loop. During the measurements the objects were positioned at 10 cm from the corner of the loop in the geometry of Fig. 5.5,and 15 cm from the receiving coil (i.e. mid distance between the transmitting and recieving coils). The excitation loop and receiving

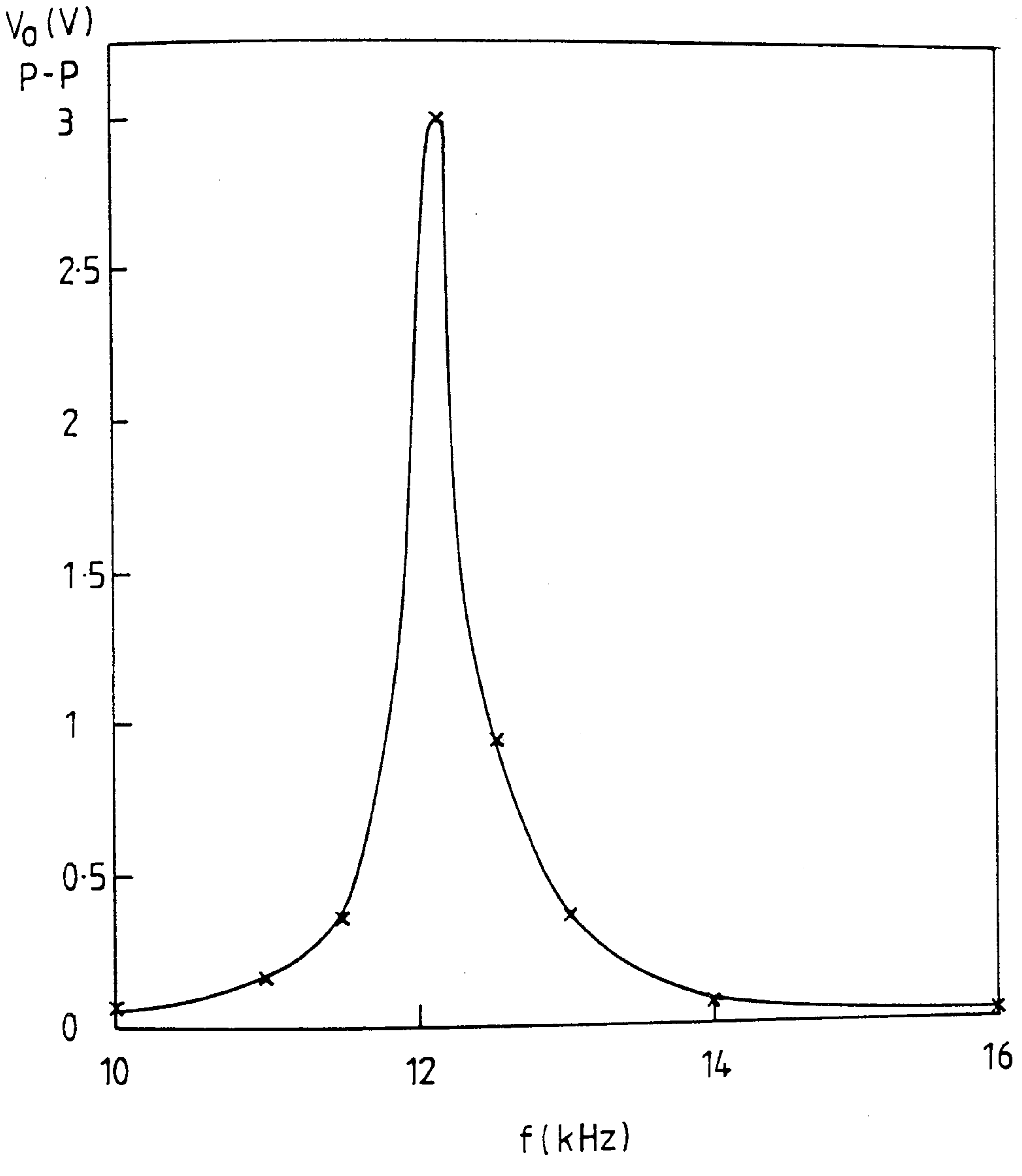

Fig 6.3 Frequency response of the tuned receiving coil. The bandwidth of the coil is about 100Hz and Q of 120.

coil were tuned for resonance and the current through the transmitter coil was maintained at 1A r.m.s.The results of the measurements are shown in Fig. 6.4, and are seen to agree well with the theoretical analysis given in Chapter 5.

These results indicated that the output increases with the increasing frequency. However, as mentioned in section 6.2.1, the operating frequency must be selected at about one-fifth of the self-tuning frequency of the coils. The operating frequency of about 12 kHz was therefore selected.

The output of the receiving coil pre-amplifier was measured as a brass ring object of 4 cm diameter was moved along the x-axis in the arrangement of Fig. 5.5. The distance between the excitation and receiving coils was 30 cm, with a current of 1A r.m.s. through the loop during the measurement. The measurements were carried out for different lengths of the receiving coil. The results are given in Fig. 6.5. Comparing these results with those of Fig. 5.8, the profile of the response curves are in agreement for both lengths of the coil whilst the metal object is inside the loop. However, they do not completely agree when the metal is outside the loop. The reason for this is that in the theoretical calculations of the output only the x-component of the field was considered in order to simplify the calculation. Since the net field at the outside of the loop is in the

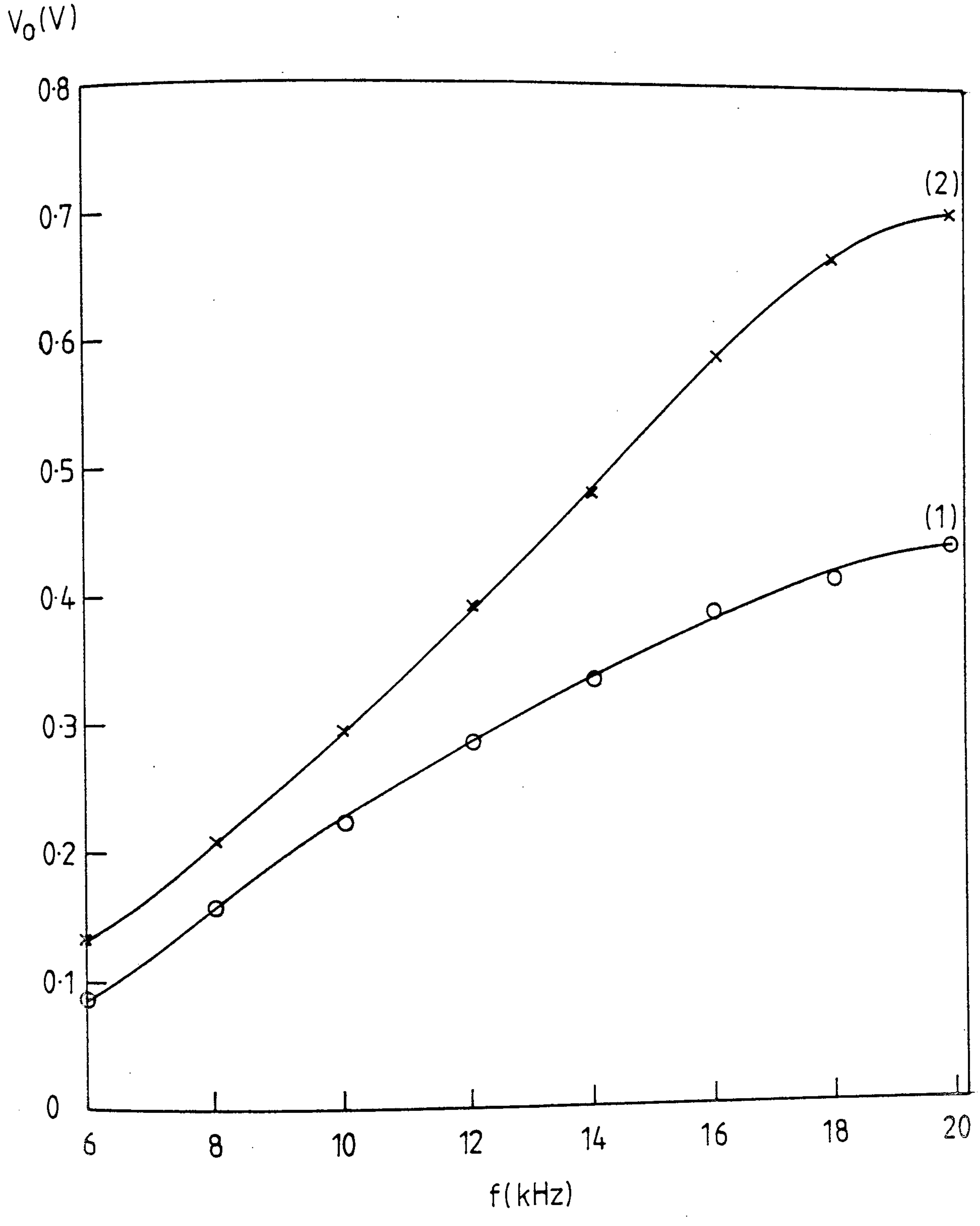

Fig 6.4 The output of the pre-amp due to the metal objects at different excitation frequencies with all other parameters kept constant
(1) Using iron object (1 × 2 × 3 cm) size.
(2) Using copper object (1 × 2 × 3 cm) size.

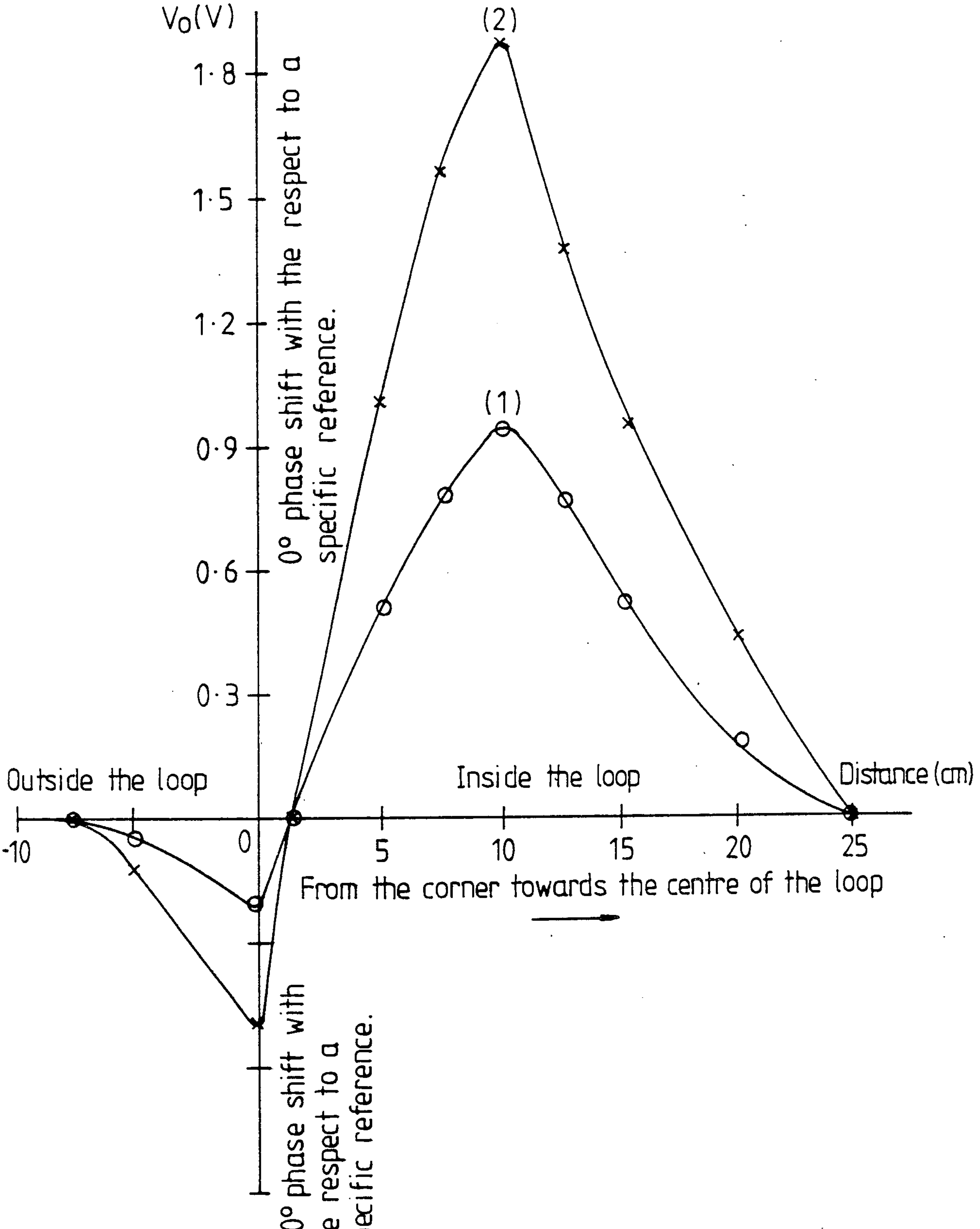

Fig 6.5 The output of the tuned amplifier at different distances of the brass ring object along the x-axis with 30cm distance between transmitting and receiving coils.
(1) For receiving coil length of 10 cm.
(2) For receiving coil length of 20 cm.

reverse direction to the net field inside the loop, the recieved voltages for the metal ring inside and outside the loop are 180° out of phase with each other. In Fig. 6.5 the output of the pre-amplifier was plotted only for the metal ring being in the first half of the loop. When the metal passes to the second half of the loop, the output has the same profile, but is 180° out of phase with respect to the output due to the metal being in the first half of the loop. Again, the reason of this is that the net fields of the two halfs of the loop are opposed to each other.

It should be noted that all the descriptions and measurements given in this section are valid for both metal detection and side determination receiving coils.

6.3 ELECTRONIC DESIGN OF THE EQUIPMENT

This section describes the detailed electronic design of the ferrous and non-ferrous detector. The block diagram of the complete receiving part of the equipment is given in Fig. 6.6

6.3.1 Design of the Analogue Part of the Detector

As explained in section 2.4, two receiving coils were used in the development of the detector; one coil for the detection and discrimination of the metallic object and other for side determination. The output of each receiving coil was processed separately to perform

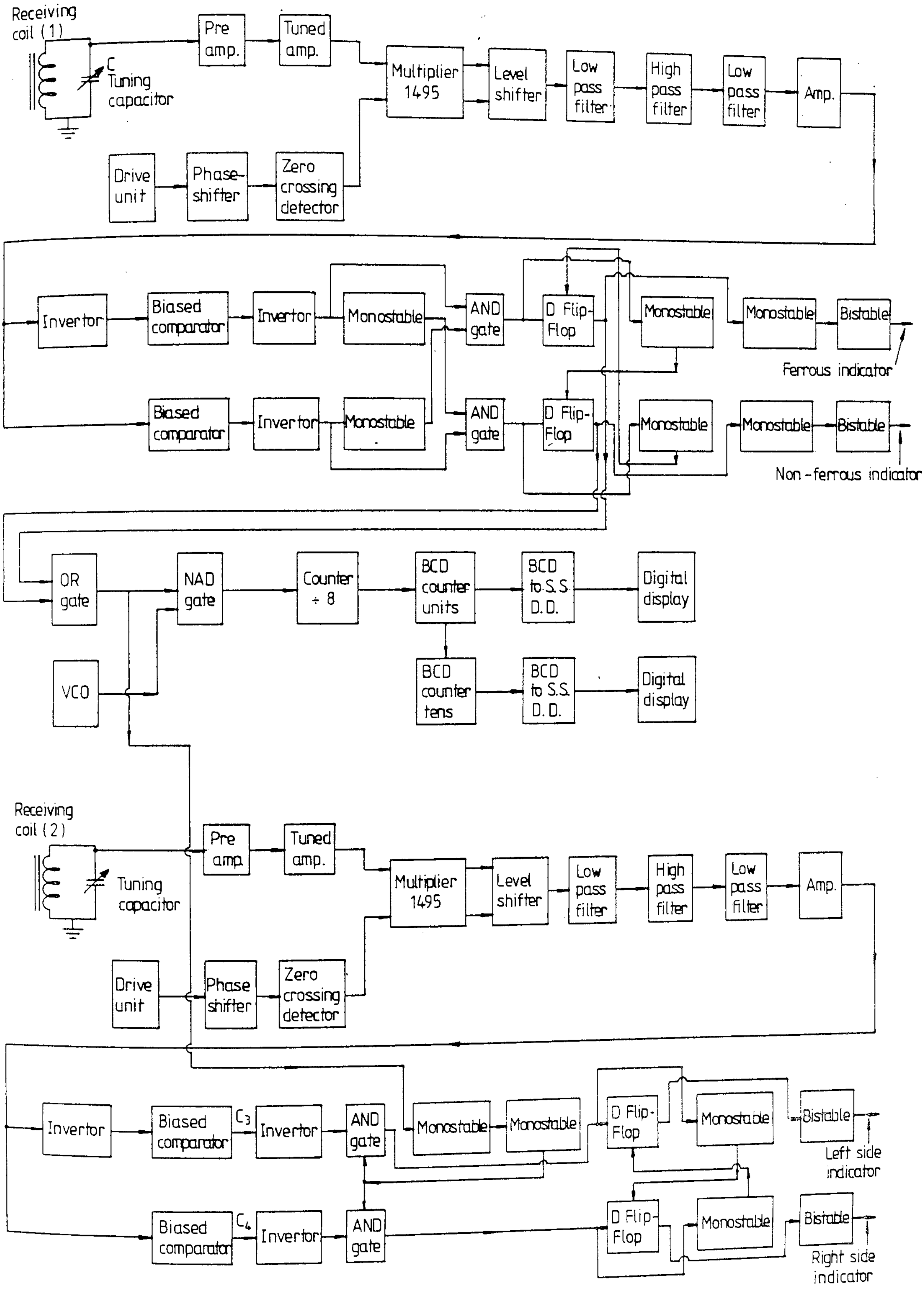

Fig 6.6 The complete block diagram of the ferrous and non-ferrous detector.

their separate tasks.

6.3.1.1 Analogue Signal Processing for the Detection and Discrimination

The detailed circuit diagram of this part of the equipment is shown in Fig. 6.7 and it consists of the following items:-

(1) The Pre-Amplifier.

A high input impedance amplifier wiht a gain of 10 is used to amplify the output from the receiving coil to a level suitable for the efficient operation of the following electronic circuits.

(2) Tuned Amplifier.

The detected signal was then further amplified and unwanted signals attenuated by means of a tuned amplifier, centred at the excitation frequency. The frequency response of the tuned amplifier is shown in Fig. 6.8. It is evident from this response and that of the tuned receiving coil that the overall system has a very sharp frequency response centred at the drive frequency. The drive unit should therefore have a frequency stabilised signal generator.

(3) The Phase-Shifter and Comparator.

A phase correction network was put in the path of the reference signal from the signal generator to the

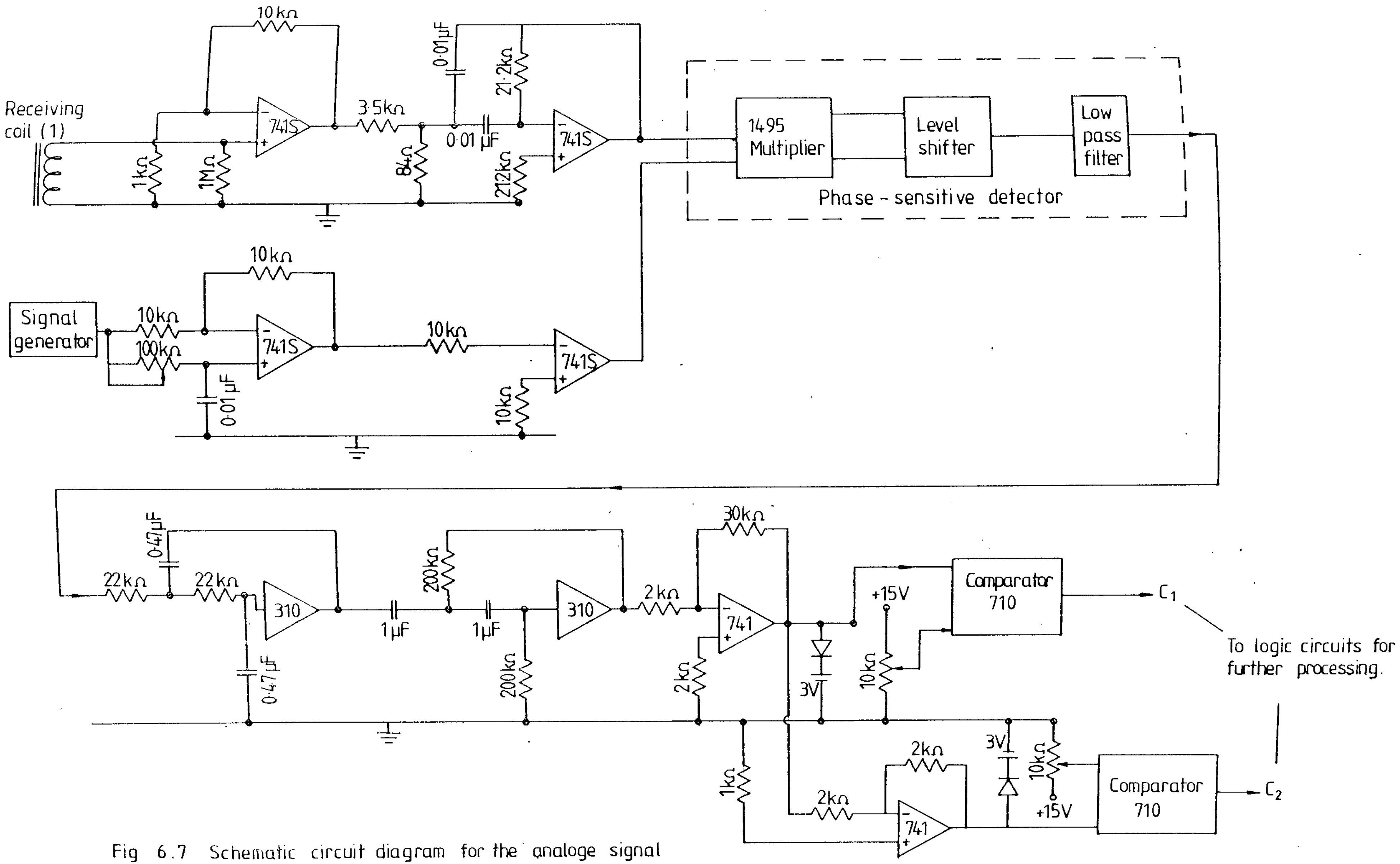

Fig 6.7 Schematic circuit diagram for the analoge signal processing of the detection and discrimination part of the receiver.

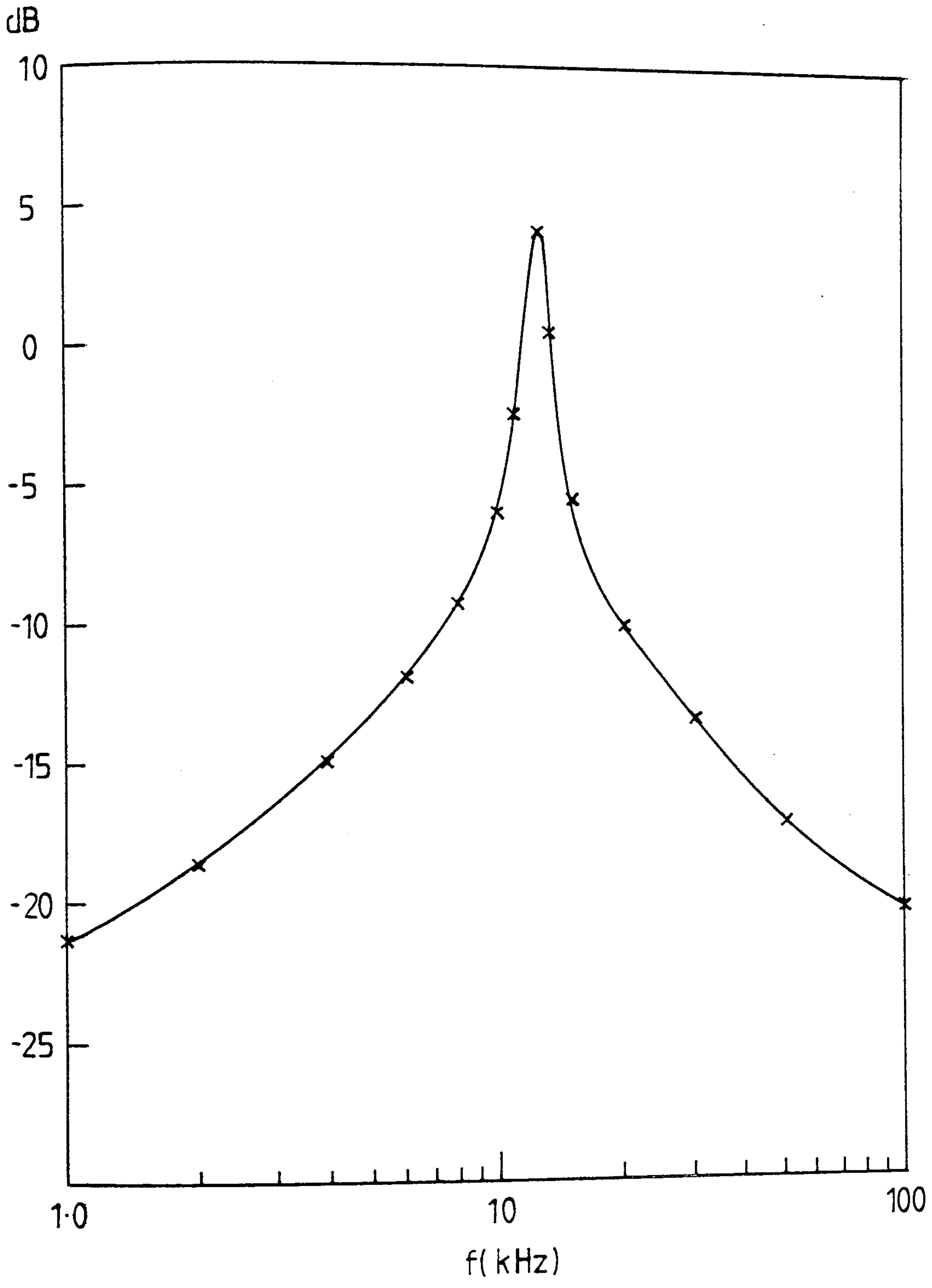

Fig 6.8 Frequency response of the tuned amplifier.

phase-sensitive detector. This circuit provides the necessary adjustment to the phase of the reference signal with respect to the phase of the received signal. This is required in order to discriminate between ferrous and non-ferrous metals.

The output of the phase-shifter was connected to a zero-crossing comparator. The comparator converts the sinusoidal signal to a square wave for use as a reference signal for the phase-sensitive detector.

(4) The Phase-Sensitive Detector.

As was mentioned earlier in the thesis, the phase-sensitive detector is used to extract the signature of the movement of the metallic object on the conveyor belt and detect the phase difference between the reference signal and the received signal. The detailed circuit diagram of the phase-sensitive detector is given in Fig. 6.9. The theoretical analysis given in section 5.3 showed that the output of the phase-sensitive detector is positive if the phase-shift between the input and reference signal is less than 90^{o}, the output becoming negative when the phase shift is greater than 90^{o} and less than 270^{o} and so on. In Chapters 3 and 5 it was shown that the detected signal due to ferrous metal has a phase that is different from that due to non-ferrous metal. By including the phase adjustment facility described in point (3), it becomes possible to discriminate between ferrous and non-ferrous metals. The output of the phase-sensitive detector was

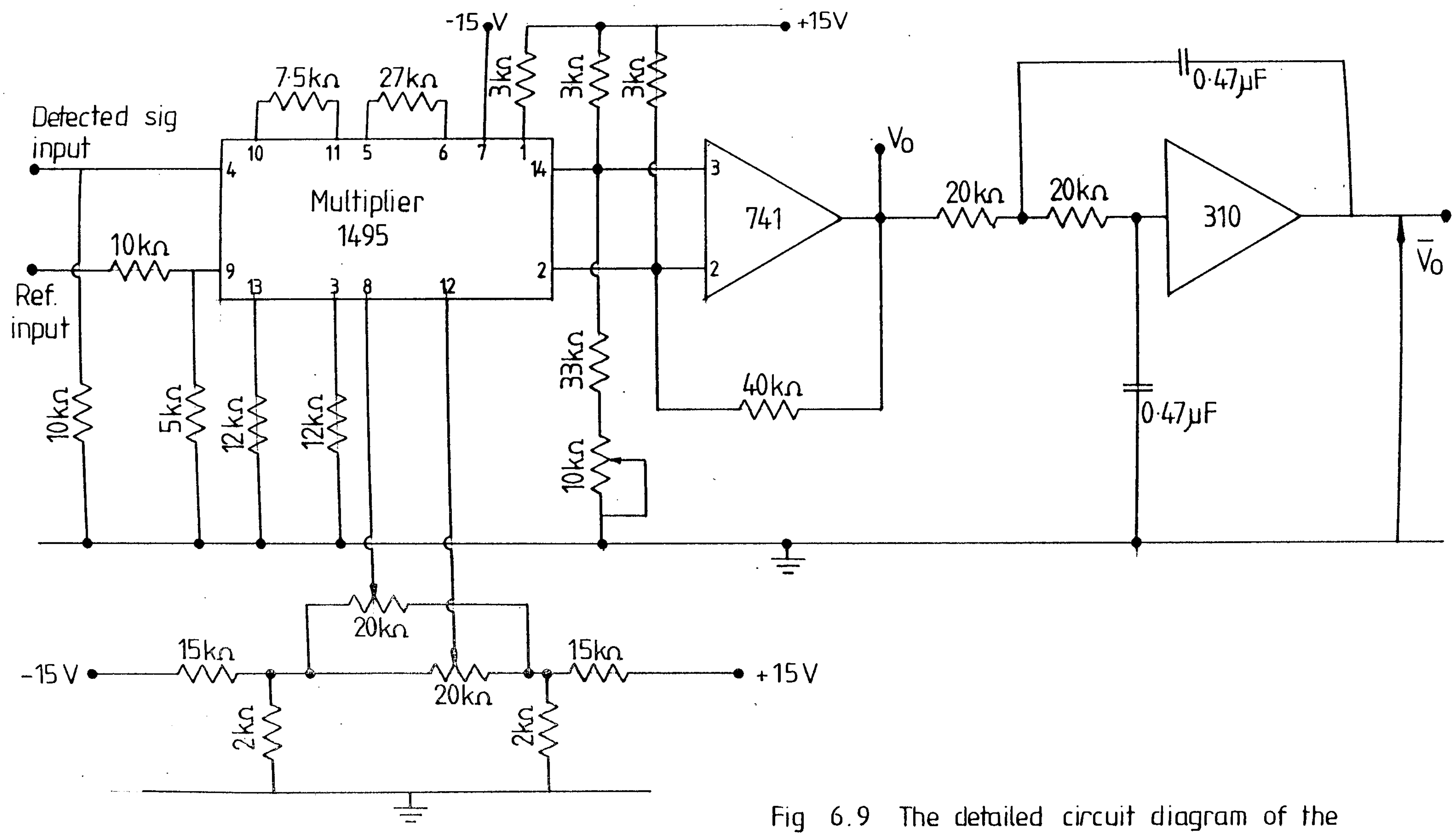

Fig 6.9 The detailed circuit diagram of the phase-sensitive detector.

measured for various shapes, sizes and positions of both ferrous and non-ferrous metals. The results for ferrous and non-ferrous $\frac{7}{16}$" B.S.W. nuts at different positions along the direction of the belt are shown in Figs 6.10 and 6.11. It can be seen from these graphs that the output of the phase-sensitive detector due to ferrous metal objects is of opposite polarity to the output for non-ferrous metal objects. This is so, whether they are outside or inside the excitation loop. It can also be seen that the outputs for both ferrous and non-ferrous objects outside the loop are opposite to the output for objects inside the loop. However, the polarity of the output also changes when the object passes from one half of the loop to the other half in both the ferrous and non-ferrous cases. These features can be used to discriminate between ferrous and non-ferrous objects and to locate the position of the object on the defined side of the belt.

It was mentioned in section 5.3 that the speed of the response of the detector to the movement of the object on the belt depends on the time constant τ_c of the low-pass filter of the phase-sensitive detector. The bandwidth of the system also depends on τ_c. A practical compromise has therefore to be made between the speed of the response and bandwidth of the system. This was achieved by measuring the step input response of the low-pass filter for different time constant values and comparing the time taken by the output to reach the

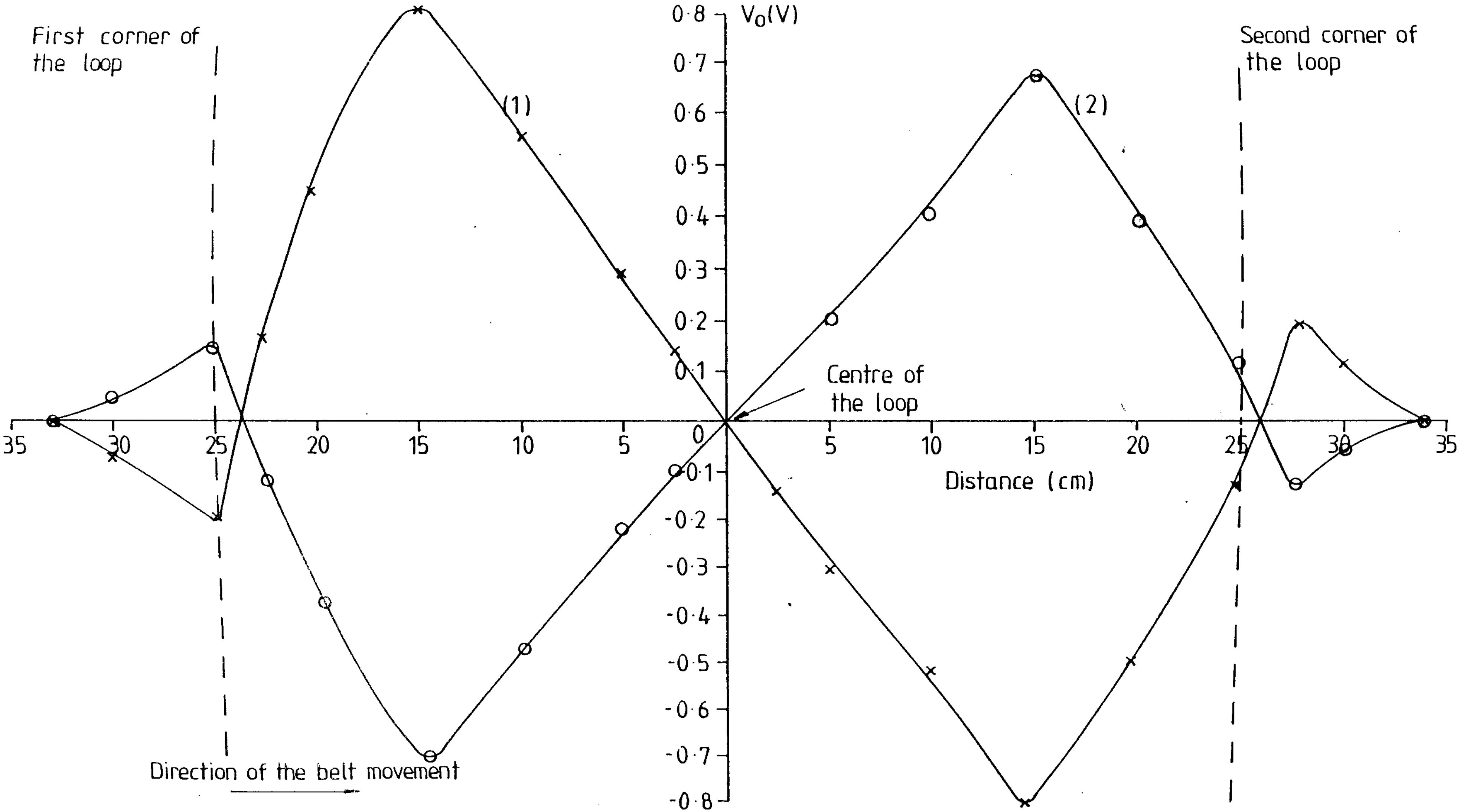

Fig 6.10 The output of the phase-sensitive detector for an object moving along the diagonal of the loop in the direction of the belt. (1) Non-ferrous and (2) ferrous object.

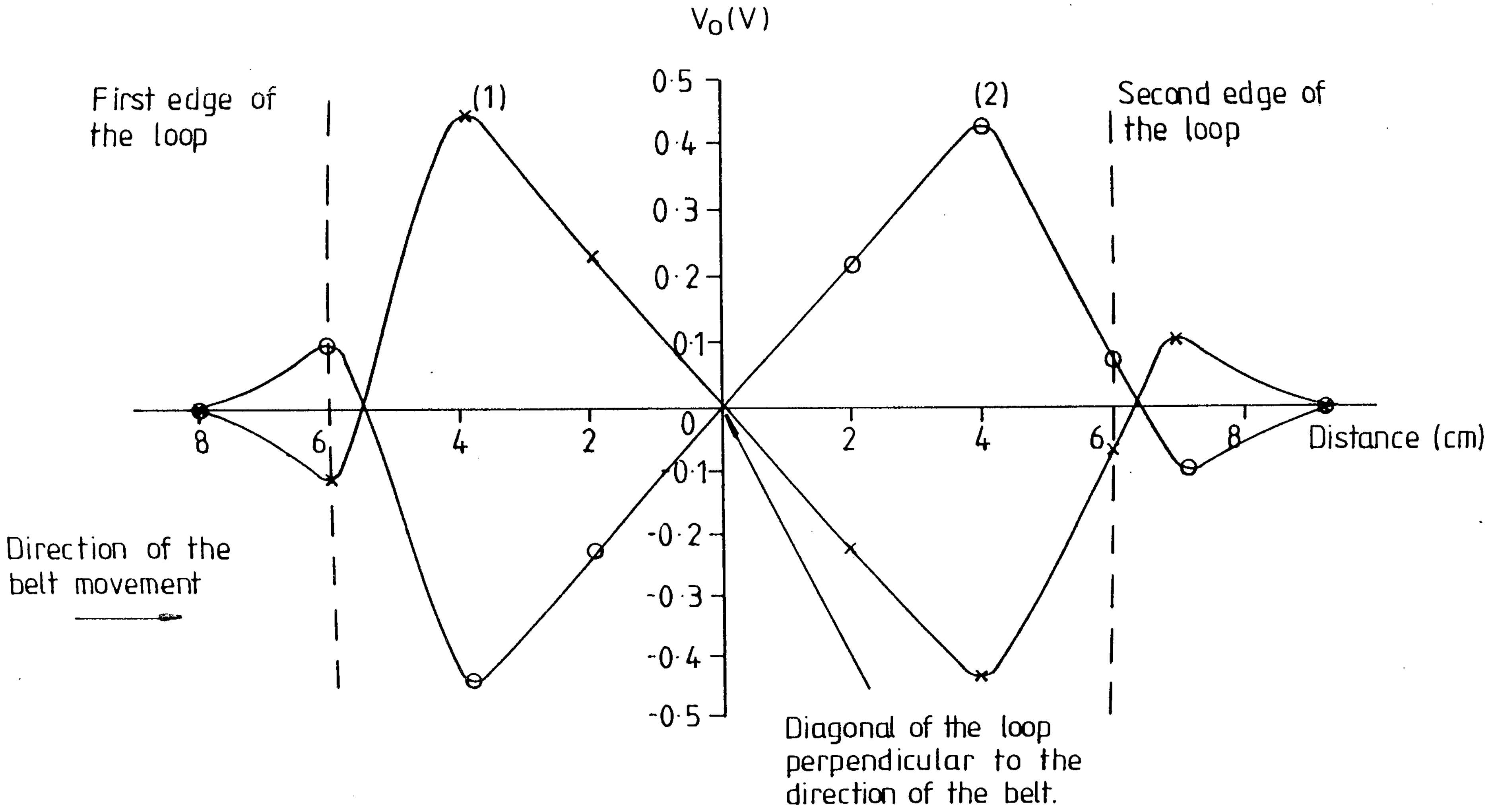

Fig 6.11 The output of the phase-sensitive detector for an object moving along a line parallel to the direction of the belt movement with 6cm distant from the corner of the loop near the edge of the belt. (1) Non-ferrous and (2) ferrous object.

the steady-state value with the speed of the belt. A time constant of about (9 msec) was found to be sufficient to track the movement of the object on the conveyor belt, with the belt travelling at a speed of about 1 m/sec. With this filter's time constant, the bandwidth of the phase-sensitive detector was about 33 Hz. This was sufficient to suppress any unwanted signals present in the environment in which the equipment was tested.

(5) The Band-pass Filter.

The band-pass filter was built using a cascaded low pass and high pass filter at the output of the phase-sensitive detector. This filter eliminates the d.c. off-sets and d.c. drifts, hence increasing the reliability and sensitivity of the detector. The filter also attenuates any unwanted signals which are at frequencies greater than the centre frequency of the filter. The filter was designed so that its centre frequency was equal to the reciprocal of the time required by the object to travel within the physical size of the loop in the direction of the belt at the mid-distance from the corner to the centre line of the loop on either side of the belt. The frequency response of the band-pass filter is shown in Fig. 6.12.

(6) The Amplifier and Inverter.

The output of the band-pass filter was further amplified using an operational amplifier. The amplification

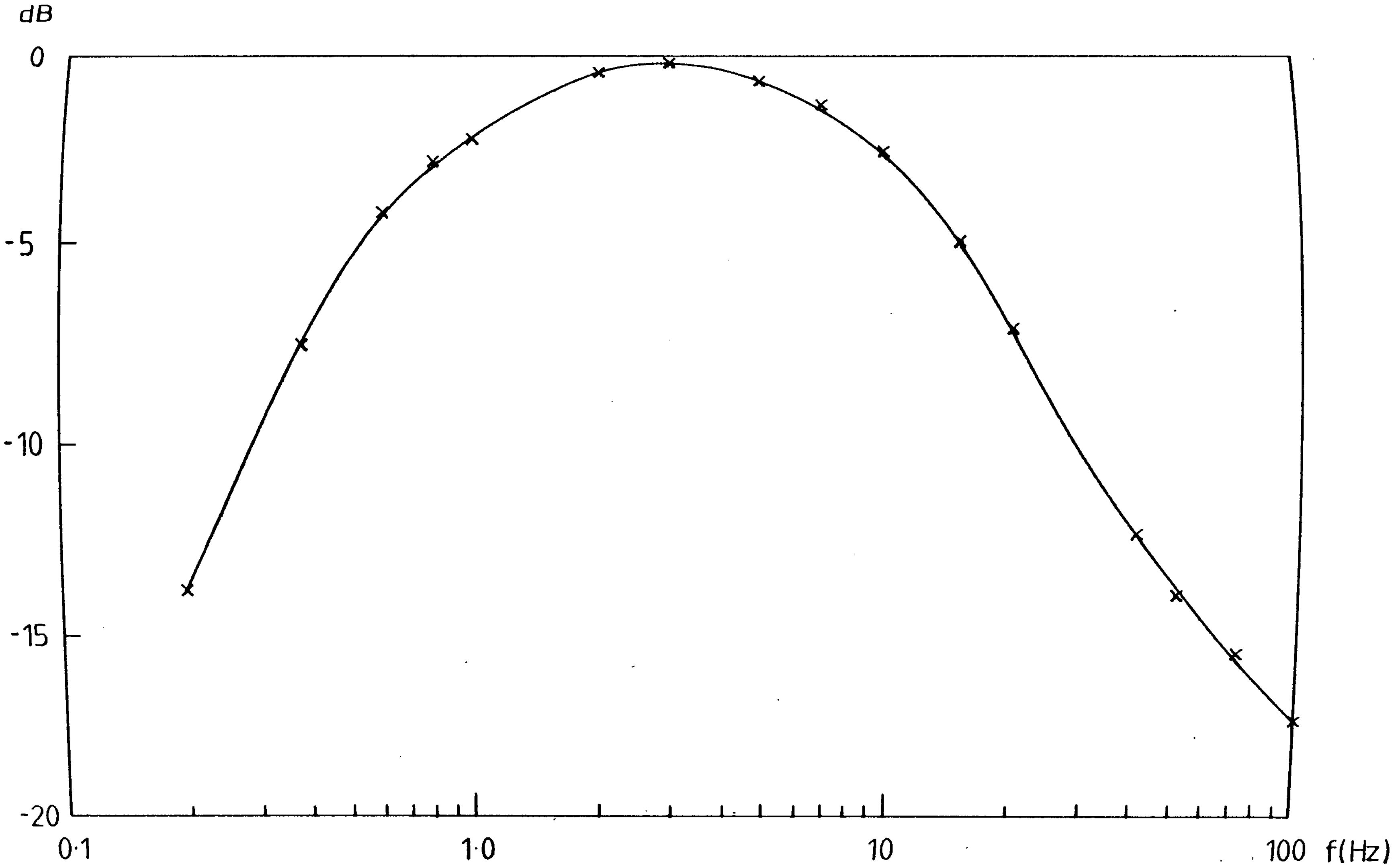

Fig 6.12 Frequency response of the band-pass filter.

was necessary to make the signal of suitable amplitude for further processing for completion of the detector requirements.

An inverter was also required at the output of the amplifier because both polarities of the amplifier output are necessary for the purposes of discrimination and location of detected metal objects

(7) The Comparators.

Two integrated circuit voltage comparators type 710 giving a TTL compatible pulse output with a sensitivity of a fraction of millivolt were used to convert the analogue signals to TTL compatible signals. The amplifier and inverter described above each drive one comparator the threshold levels being adjusted to distinguish the signal from the background noise. In the experimental tests carried out on the performance of the detector, a biassing level of 0.2V to each comparator was sufficient to distinguish the signal from the interference noise. The output of the comparators were fed to the next stage of logic circuits for further processing.

6.3.1.2 Analogue Signal Processing for Side Determination

The output of the second tuned receiving coil was fed to an electronic circuit which is similar to that of Fig. 6.7. Since the detailed description of the elements involved in the development of the circuit were given in section 6.3.1.1, there is no necessity to repeat it again here.

In the case of the signal processing for side determination, the phase-shifter in the path of the reference signal to the phase-sensitive detector was adjusted so that the output of the phase-sensitive detector is positive when the metal is in one side and negative if it is in the other side of the belt. Fig. 6.13 shows that the output is positive for any metal, either ferrous or non-ferrous, when it is within the loop on one side of the belt. It also shows that the output is negative for the metal object being within the loop on the other side of the belt. These measurements were carried out using ferrous and non-ferrous ($\frac{7}{16}$"B.S.W.) nuts moved manually along the stationary belt in Fig. 5.5 with a distance of 15 cm from the corner of the loop near the edge of the belt. During the measurements, the distance between the excitation loop and receiving coil was fixed at 30 cm and the current through the loop was 1A r.m.s. The output of the analogue signal processing circuit was connected to a logic circuit for further processing to determine the side of the belt on which the metal is located.

6.3.2 TTL Circuits to Discriminate Between Ferrous and Non-ferrous Objects

The logic circuit to process the output of the comparators for discrimination between ferrous and

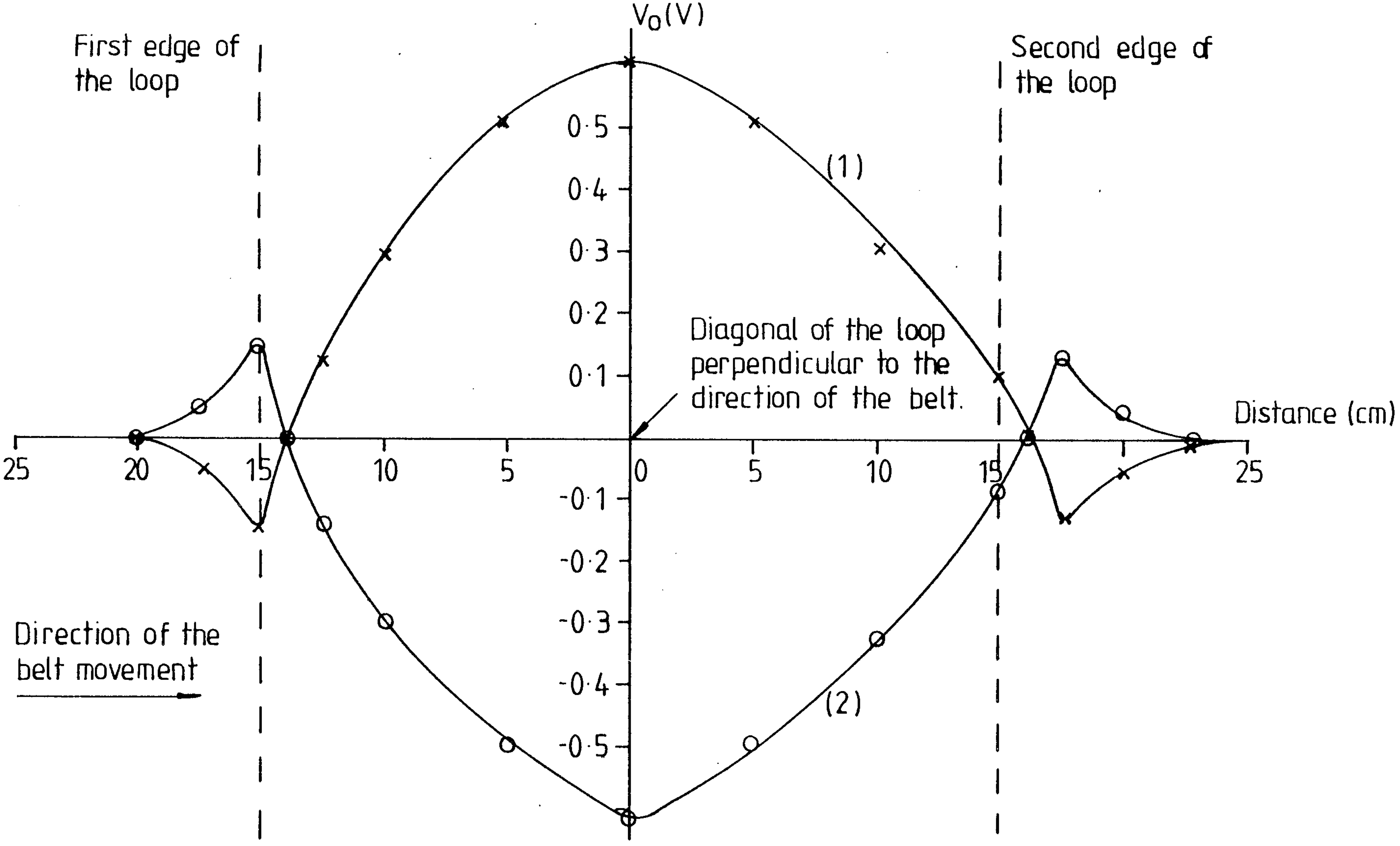

Fig 6.13 The output of the side determination phase - sensitive detector for ferrous and non - ferrous metals moving along a line parallel to the direction of belt movement with 15cm distant from the corner of the loop near the edge of the belt. (1) Left and (2) Right side of the belt.

non-ferrous metal objects is shown in Fig. 6.14. Waveforms at different points of the circuit are given in Fig. 6.15. The inverted waveform of the comparators C_1 and C_2 are respectively I_1 and I_2. In both outputs the narrow pulses occur when the metal object is outside of the loop and the wide pulses occur when the metal object is inside the loop. The rising edge of the first pulse in each output I_1 and I_2 is used to trigger a monostable. I_1 triggers M_1 and I_2 triggers M_2. The output M_1 opens the gate A_2 which allows I_2 to pass through and M_2 opens the gate A_1 and allows I_1 to pass. The periods of M_1 and M_2 were adjusted so that they were just greater than the time taken by the object to travel within the detection zone of the system. The output A_2 was fed to a D flip-flop which gives an output D_2. A_2 also triggers a monostable, causing it to give the output M_4. Connecting M_4 to the 'clear' input of the other D-type flip-flop clears it to give the output D_1. The A_1 output triggers monostable M_3 which was used to clear the D_2 flip-flop at the end of the A_2 pulse. A_1 was also connected to the D_1 flip-flop to indicate the other type of metal. The D_2 signal was used to trigger the monostable M_6 at the falling edge of the pulse. This means monostable M_6 starts its time period when the object reaches the centre line of the loop which is perpendicular to the direction of the belt whatever is the position of the object on the width of the belt. In the actual installation of the equipment, the period of M_6 can be made so that it ends when the

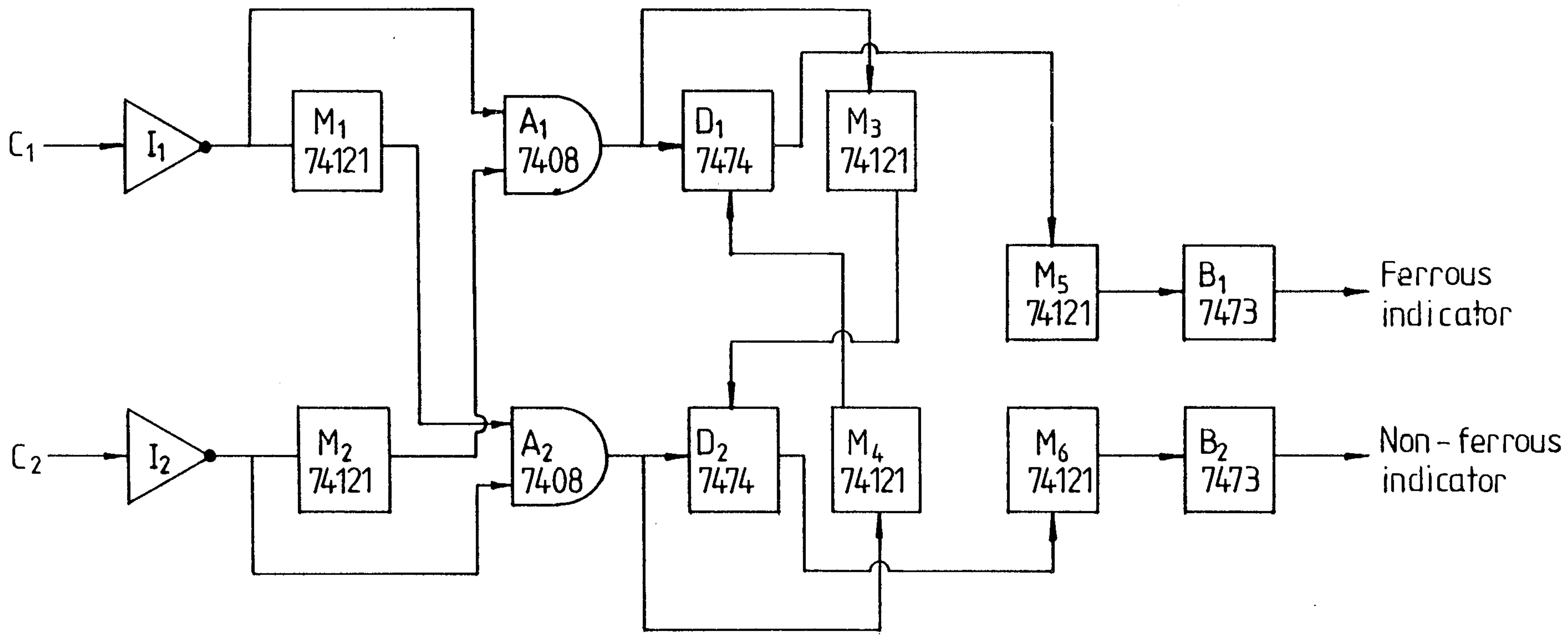

Fig 6.14 TTL circuits for discrimination between ferrous and non-ferrous objects.

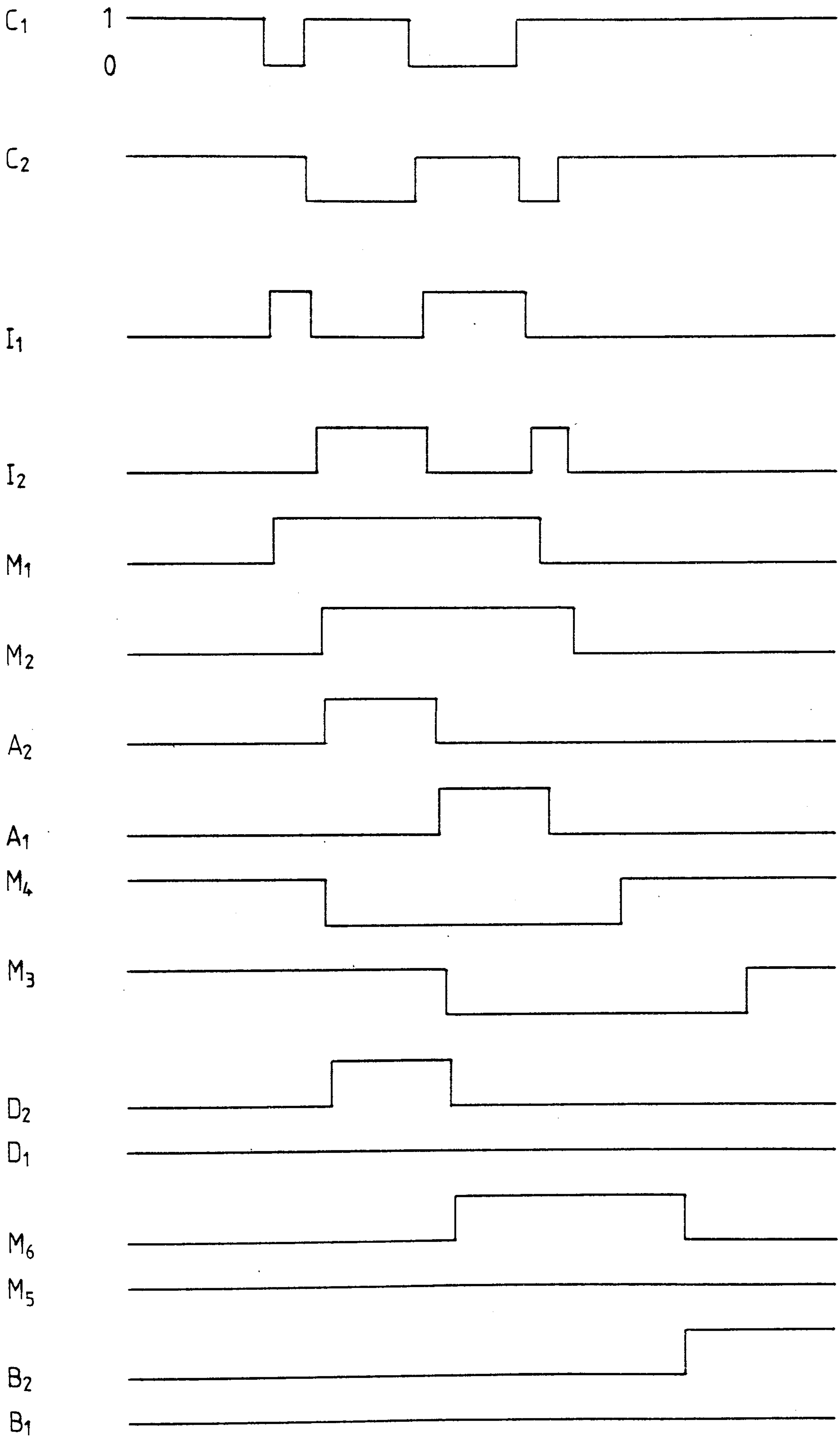

Fig 6.15 The waveforms of the TTL circuits for discriminating between ferrous and non-ferrous metals.

object moves out of the detection zone of the equipment. At the end of the M_6 period the belt can be marked along a line perpendicular to the direction of the belt to indicate the position of the object on the belt which can be stopped and the object removed. The M_6 monostable was connected to a bistable switch B_2. The output of the switch was used to indicate a particular type of metal. It can also be used to stop the belt at the required time. The D_1 flip-flop was connected to the monostable M_5. As in the case of monostable M_6, the monostable M_5 was also used to excite a bistable switch B_1. The discussion given for D_2, M_6 and B_2 is equally applicable to D_1, M_5 and B_1.

Assuming the above description was for the presence of a ferrous object, then for non-ferrous metal all the outputs are reversed and D_1 gives an output pulse while D_2 is reset. The high output of D_1 causes M_5 to be triggered which sets B_1 to be high. Two different lights were employed at the outputs of B_1 and B_2 for indication of the metal type. In this way it was possible to discriminate between ferrous and non-ferrous metals.

The symbols used in Fig. 6.15 refer to the output of the appropriate integrated circuits employed in Fig. 6.14.

6.3.3 Logic Circuit to Find the Side of the Belt on which the Metal Exists

The TTL circuits for side determination of the belt on which the metal exists are shown in Fig. 6.16. Waveforms

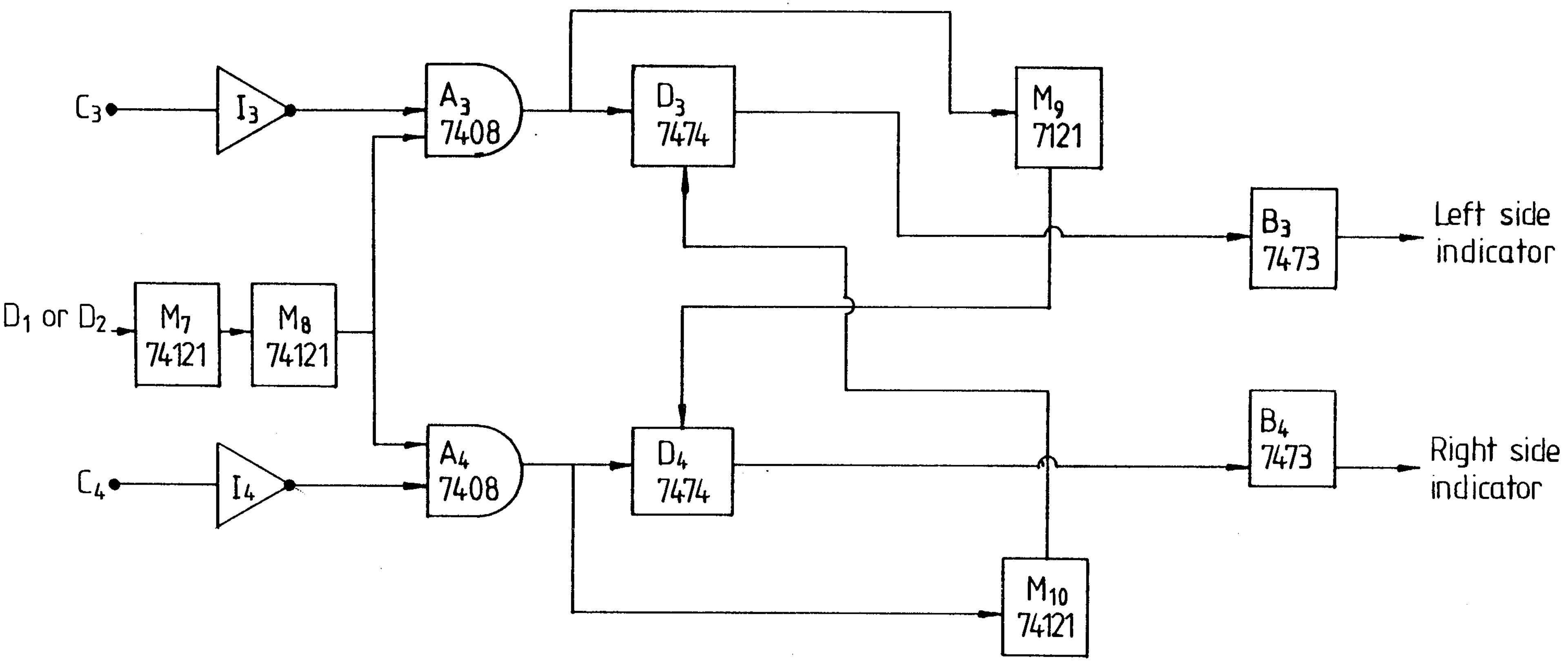

Fig 6 . 16 TTL circuit for the determination of the side of the belt on which the metal exists.

at different points are given in Fig. 6.17. The inverted forms of the output of the side-finding comparators are I_3 and I_4. The signal D_1 or D_2 from the discrimination logic circuit opens the gates A_3 and A_4 for a period defined by the monostable M_8. Hence, the outputs of the gates are A_3 and A_4 as shown in Fig. 6.17. A_3 and A_4 were fed to monostables M_9 and M_{10} respectively. They were also connected to D_3 and D_4 flip-flops. The outputs M_9 and M_{10} were connected to D_4 and D_3 respectively. The D_4 flip-flop gives a pulse which is similar to the A_4 and at the same time the monostable M_{10} clears D_3 flip-flop and resets it to zero as shown in the waveforms given in Fig. 6.17. At the end of the A_4 pulse, the A_3 pulse triggers monostable M_9 which clears the D_4 flip-flop to zero. The periods of M_9 and M_{10} were made long enough to be greater than the maximum time required by the object to travel within the zone of the system. The D_4 output sets bistable B_4 to high level and stays at this level until it is reset manually while B_3 remains unset because of the low output of the D_3 flip-flop. The bistable switches B_3 and B_4 were connected to two different lights which indicate the side of the belt on which the metal exists.

Assuming the above discussion was for the metal being in the left side of the belt, the output waveforms

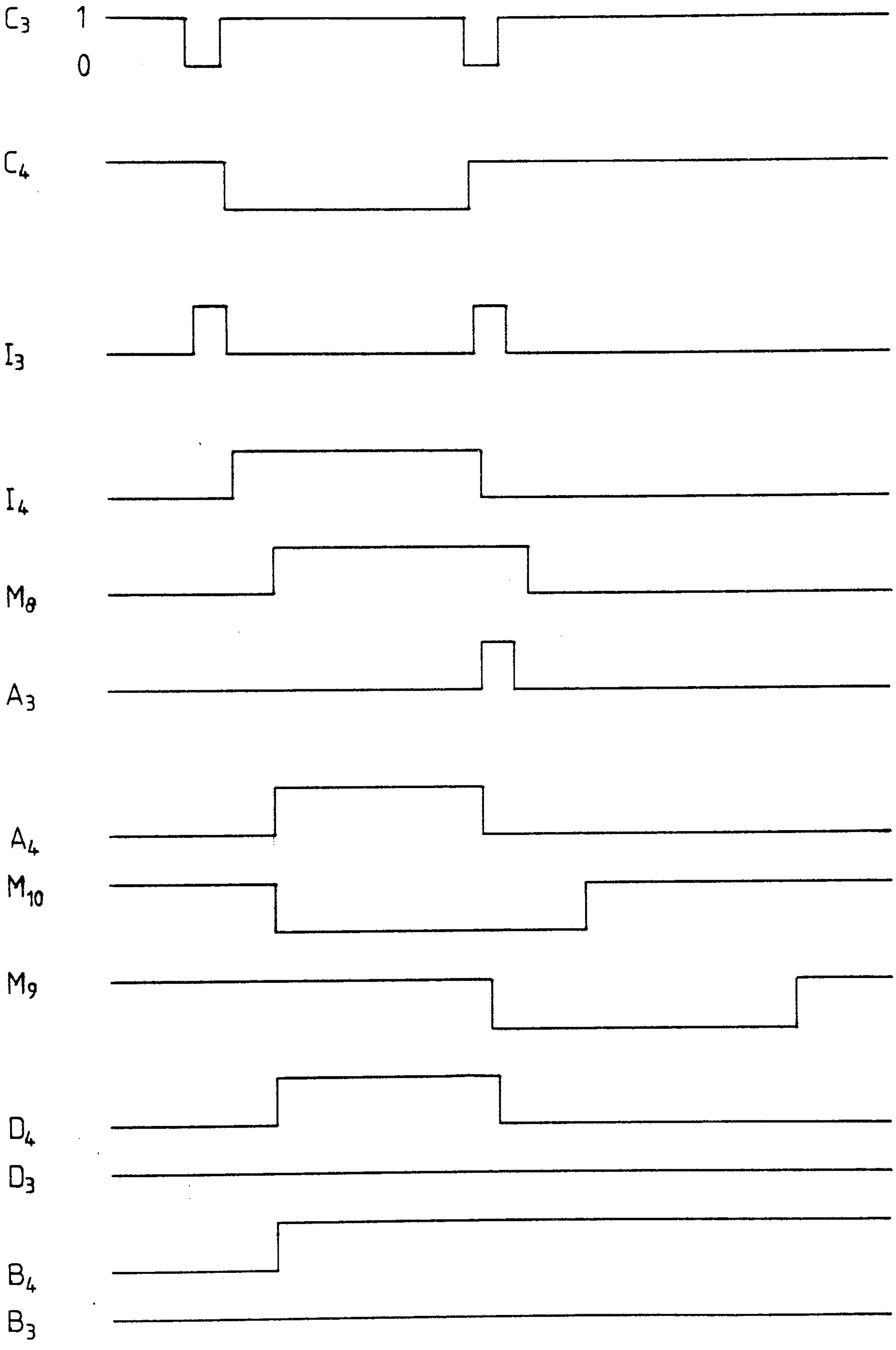

Fig 6.17 The waveforms at different points of the TTL circuit for determination of the side of the belt on which the metal exists.

are reversed for metal being in the right side of the belt. In this case the D_3 flip-flop gives a pulse which sets bistable B_3 high to indicate the right side of the belt. Again, it remains high until it is reset manually.

When the metal is in the centre of the belt, neither of the side indicating lights operate because the component of the field produced by the metal parallel to the axis of the side detection coil is zero and hence there is no output from the side determination coil.

6.3.4 Locating the Object on the Defined Side of the Belt by Using TTL Circuits

Either the output of the D_1 flip-flop or the D_2 flip-flop opens the gate A_3 when the metal object, ferrous or non-ferrous, enters the physical geometry of the loop. A voltage controlled oscillator integrated circuit type 74124 running at 750 Hz produces continuous pulses which pass through the gate during the opening period. Both the D_1 and D_2 pulses start at the entrance of the object to the loop and end as the object reaches the centre lines of the loop perpendicular to the direction of the belt movement. The time taken by any object of a defined size at any point on the width of the belt on the given side is therefore equal to the number of pulses passing through the gate, multiplied by the period of each pulse.

The distance along the belt from the start of the square loop coil at any point of the belt on the defined side to the centre line is equal to the perpendicular distance from the corner of the loop to the location of the object. Counting the number of pulses passed during the periods D_1 or D_2 and calibrating it to distance therefore gives the location of the object from the corner of the loop. At a VCO frequency of 750 Hz and with the speed of the belt of about 1 m/sec, the counting can be achieved using a 4-bit binary counter N_1 to divide the output of A_3 by 8 and then counting the result of the division by employing two 4-bit BCD counters N_2 and N_3. The position of the object on the defined side can then be displayed numerically using seven segment displays. The position-measuring system was designed to be reset manually after removing the metal from the processing material.

The position-measurement logic circuit diagram is shown in Fig. 6.18 and waveforms at different points of the circuit are shown in Fig. 6.19.

6.4 EXPERIMENTAL TESTS ON THE PERFORMANCE OF THE EQUIPMENT

6.4.1 The Experimental Rig

In order to test the performance of the equipment for detection, discrimination and location of a metal object in the material carried on a conveying system, a conveyor belt system was constructed with the aid of the workshop staff from facilities available in the department. The

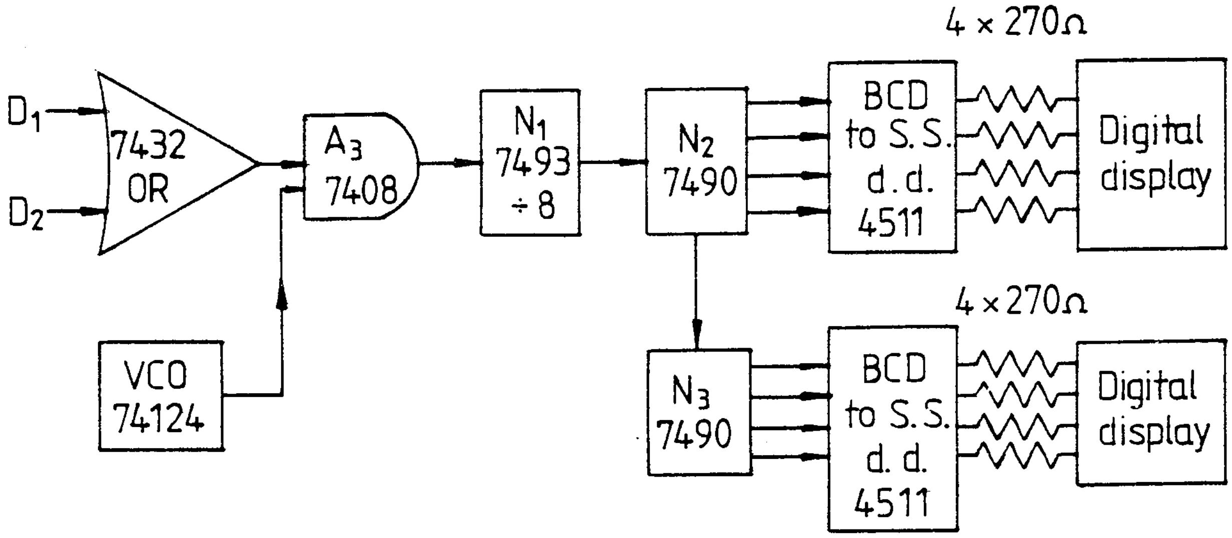

Fig 6.18 Logic circuit for location of the object in the defined side of the belt.

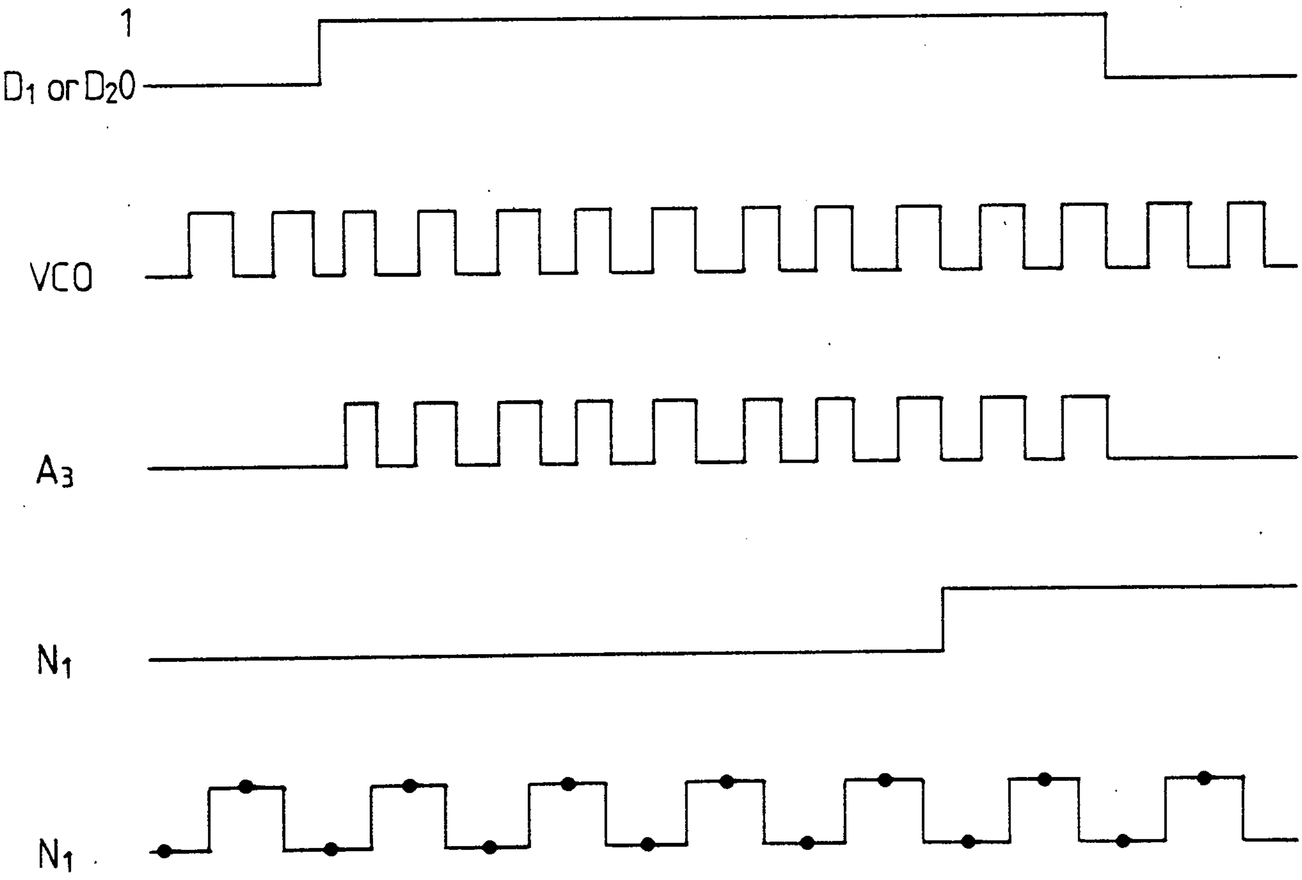

Fig 6.19 The waveforms at different points on the logic circuit used to measure the position of the object on the defined side of the belt.

width of the belt used was 42 cm. The speed of the belt was made about 1 m/sec which is similar to the speed of a typical conveyor belt used in the food processing industry. The excitation electromagnetic loop was situated under the belt with one diagonal parallel to the direction of the belt and the other perpendicular. It was rigidly fixed to prevent mechanical vibration being caused by the running of the belt motor. The receiving coils were also fixed rigidly at the centre above the belt. The distance between the excitation loop and the receiving coils was about 30 cm. The axis of one of the receiving coils was made parallel to the direction of the belt and the axis of the side-detection coil was arranged to be perpendicular to the direction of the belt. The complete arrangement of the detector with the conveyor belt is shown in Fig. 6.20.

6.4.2 Experimental Tests on the Equipment

The performance of the system was examined by putting different types of metal samples on the conveyor belt and observing the response of the detector. It was found that the equipment worked successfully in achieving the project aims. The equipment correctly detected and discriminated between ferrous and non-ferrous metals of different sizes at different position on the belt when included within non-conductive conveyed material. The system was also able to successfully determine the side of the belt on which the metal existed and to locate the

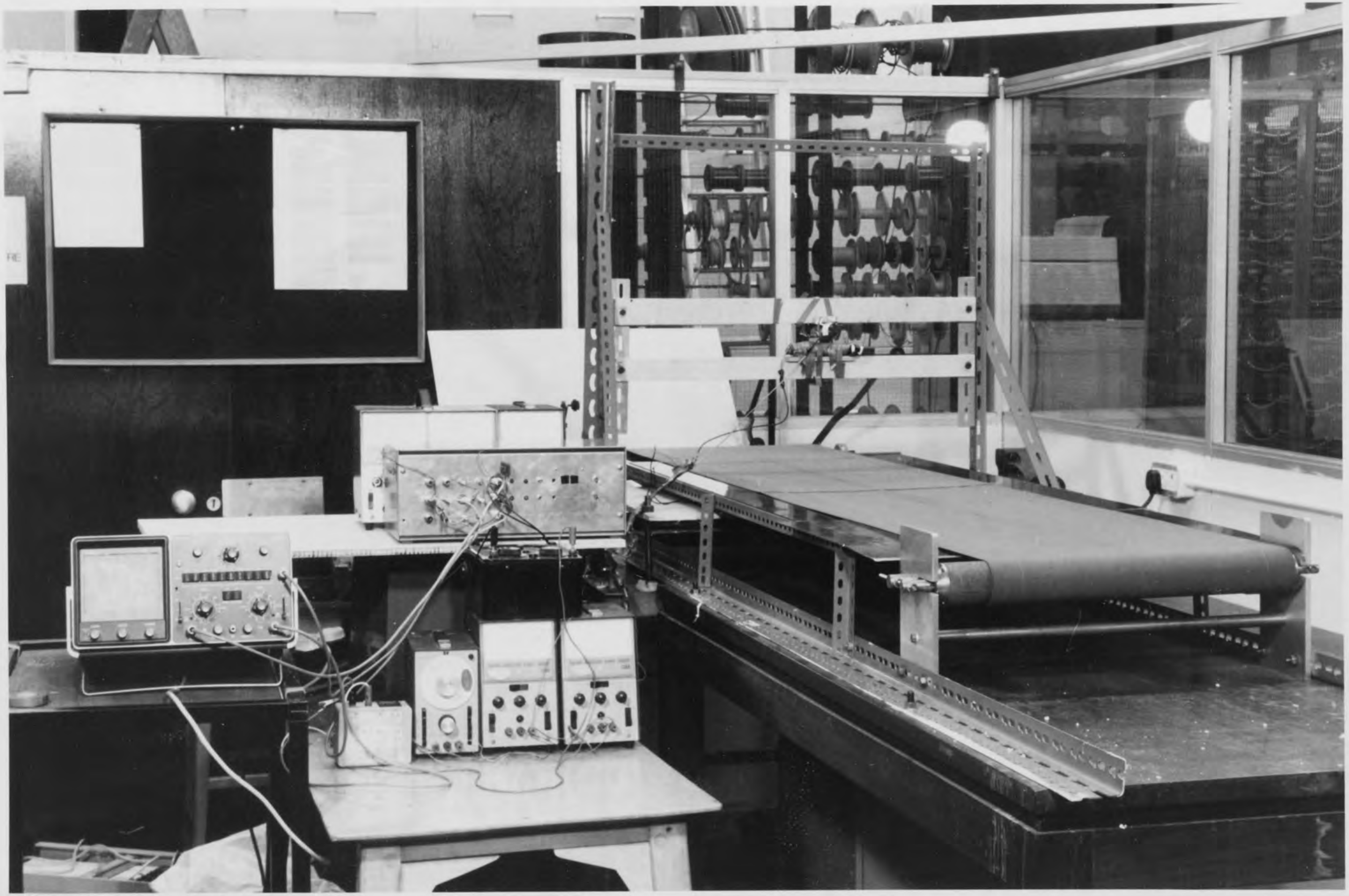

Fig. 6.20 The arrangement of the excitation loop and receiving coils with conveyor belt

position of the object on the defined side from the corner of the loop near to the edge of the belt. The minimum size of the metal objects detected, discriminated and located on the belt was ($\frac{5}{16}$" B.S.W.) nut. The position measurements on the defined side of the belt for some of the samples used to test the performance of the detector are presented in Tables 6.1 and 6.2. The first table is for metals on the left side and the second table for objects on the right side of the belt.

It can be seen from the above tables that the maximum error in the measurement of the position of the objects was about 1 cm which is about 2% error on the total width of the belt. This error was due to the fluctuation of the belt on the rotating rollers and variations of the speed of the motor driving the conveying system.

6.5 SUMMARY

In this chapter, the actual development of the ferrous and non-ferrous metal detection and location equipment has been described. The self-capacitance problem associated with both the excitation loop and the receiving coils and the importance of the tuning of the coils were discussed in detail. The effect of the length of the core of the receiving coils on the sensitivity and accuracy of the detector was also included. The design of the electronic equipment for the detection, discrimination and location of the object on the belt was given in full detail. The experimental tests on the performance of the equipment were also included in this chapter.

TABLE 6.1

The Measured and Actual Positions of Different Metal Samples on the Left Side of the Belt

Type of the metal sample	The measured position (cm)	The actual position (cm)
($\frac{5}{16}$" B.S.W.)brass nut	6	4 - 5.5
	10	10 - 11.5
	15	15 - 16.5
	22	20 - 21.5
	25	23.5 - 25
($\frac{5}{16}$"B.S.W.) iron nut	5	4 - 5.5
	11	10 - 11.5
	16	15 - 16.5
	20	20 - 21.5
	24	23.5 - 25
1 pence coin	6	4 - 5
	9	10 - 11
	15	15 - 16
	21	20 - 21
	24	24 - 25
Iron Block (1×2×3 cm)	6	4 - 6
	13	10 - 12
	16	15 - 17
	22	20 - 22
	25	23 - 25

TABLE 6.2

The Measured and Actual Positions of Different Metal Samples on the Right Side of the Belt

Type of the metal sample	The measured position (cm)	The actual position (cm)
($\frac{5}{16}$" B.S.W.)brass nut	6	4 - 5.5
	11	10 - 11.5
	15	15 - 16.5
	20	20 - 21.5
	24	23.5 - 25
($\frac{5}{16}$" B.S.W.)iron nut	5	4 - 5.5
	11	10 - 11.5
	16	15 - 16.5
	21	20 - 21.5
	24	23.5 - 25
1 pence coin	6	4 - 5
	10	10 - 11
	15	15 - 16
	22	20 - 21
	25	24 - 25
Iron Block (1×2×3 cm)	7	4 - 6
	12	10 - 12
	16	15 - 17
	21	20 - 22
	25	23 - 25

Chapter Seven

Conclusions and suggestions for further work

7.1 CONCLUSIONS

At the early stages of this project a study of the available metal detectors was made and deficiencies of these detectors for the present application were pointed out. From the results of this work, the following conclusions and observations are made.

(1) A ferrous metal detector was designed and built based on the flux-gate magnetometer. The equipment was designed to detect the tramp iron which may exist in the coal used for firing the generating units of a power station. Using this detector in the power industry provides a means of putting the magnetic separator on only when required. This increases the efficiency of extraction, reduces the waste of energy in the separator and also reduces the cost of separator construction. The performance of the system was tested in the laboratory by moving iron pieces within the zone of the system and noticing the response of the detector. It was found that the equipment successfully detects tramp iron and gives a signal which may be used to control the operation of the magnetic separator.

(2) A ferrous and non-ferrous metal detector was designed and built for detection of both types of metals on the conveying systems. The equipment was designed to detect, discriminate and locate the metal on the belt. In testing the performance of the system, it was found that the equipment detects, discriminates and locates the object

along the belt and on the width of the belt within a non-conductive material carried on a conveying system. The instrument can therefore be used for the continuous inspection of different types of materials.

Spurious metal objects can be hazardous to processing machinery, injurious to the operator or damaging to the end product. The detection of spurious metal is therefore essential to many manufacturing processes. Typical materials which can be examined using this detector are: plastic, rubber, tobacco, food (packed or loose) and confectionery products, grain, chemicals, liquids and powders.

Since the equipment has the ability to discriminate between ferrous and non-ferrous materials, it can be used for the detection of ferrous metal within non-ferrous materials or vice-versa. This process can be acheived either by manual bias adjustment or by automatically biassing the system, possibly using microprocessor technology. The principle of discrimination can also be used for identifying between ferrous and non-ferrous metals. This process has application in many industrial fields. The instrument also has the facility of finding the position of the object on the belt. This characteristic makes the removing of the tramp metal from the processing material very easy and reduces the period required for removing the metal from the conveyed material. The instrument is thus an aid in producing a high quality end product and increasing the production plant efficiency, which are the objectives of most material processing operations.

(3) It was found from the investigations of the field distribution of different field source geometries that the loop coil geometry has stronger fields than the other geometries considered in this work and that its field distribution is well defined by the physical size of the loop. Since the receiver detects the electromagnetic field associated with the eddy currents induced in a given metal target by the primary feild, the sensitivity and range of detection of both equipments therefore depend on the geometry and size of the loop for a given power and number of turns of the loop. From the study of the field distributions of different source geometries, it was concluded that the square loop coil is the appropriate geometry for the purpose of this work.

(4) The distance between the excitation loop and the receiving coil in both instruments strongly affects the sensitivity and range of detection. The length of the receiving coil in the ferrous and non-ferrous detector also affects the sensitivity, accuracy and range of the system.

(5) Since the accuracies of both of the designed detectors is power supply dependent, the employed power supplies should be voltage regulated. The drive frequency in the

case of the ferrous and non-ferrous detector should also be stabilised.

(6) Finally, both the excitation loops and the receiving transducers should be rigidly fixed in order to avoid mechanical vibrations which produce a reduction in the reliability of the detector. Also, the conveyor belt, which passes through the detection zone of the system, must be free from metal fasteners for proper operation.

7.2 SUGGESTIONS FOR FURTHER WORK

The following suggestions for further study are made to improve on the present work and to carry this project forward.

(1) The ferrous metal detector based on the flux-gate magnetometer should be tested in an actual power station for the detection of the tramp iron in the coal material and for the control of the magnetic separator operation. The known defficiencies associated with the operation of the detector in the power station environment, such as to be caused by stray fields produced in the switching on and off of the separator should be investigated.

(2) Using the flux-gate magnetometer, an instrument could be designed for the measurement of high a.c. or d.c. currents based on similar principles as those described in this work

for the detection of metal objects.

(3) Because of the high sensitivity and low power consumption of the flux-gate magnetometer, a communication system could be designed based on the flux-gate for use in mining and similar operations to communicate between the control base and running personnel.

(4) The ferrous and non-ferrous metal detector described in this work could be designed and built using a microprocessor implementation. In this way the biassing of the system for discrimination between ferrous and non-ferrous metals could be controlled more easily by employing software to control the discrimination process. This could lead to more reliable detection of ferrous metal within non-ferrous metals or vice-versa. The position of the object on the conveyor belt could also be measured more easily and accurately by the use of a microprocessor based system.

References

(1) R. F. MERWIN "Successful removal of ferrous elements from powder", Proceedings International Powder and Bulk Solids Handling. Rosemont, Illinois, 16-18 May 1978.

(2) W. J. BRONKALA "Magnetic removal of tramp iron", Minerals Processing, August 1970.

(3) R. L. ANDERSON "Electromagnetic loop vehicle detectors", IEEE Trans. Vehicular Tech., Vol. VT.19, No. 1, p. 23, February 1970.

(4) J. L. BARKER "Radar, acoustic and magnetic vehicle detectors", IEEE Trans. Vehicular Tech., Vol. VT.19, No. 1, p. 30, February 1970.

(5) M. K. MILLS "Future vehicle detection concepts", IEEE Trans. Vehicular Tech., Vol. VT.19, No. 1, p. 43, February 1970.

(6) J. F. SCARZELLO and G. W. USHER "A low power magnetometer for vehicle detection", IEEE Trans. Magnet. Vol. Mag. 13, No. 5, p. 1101, September 1977.

(7) J. H. LOUGHEED and D. ZIMMERMANN "Buried marking of point locations", IEEE Trans. Inst. and Meas., Vol. IM.22, No. 4, p. 399, December 1973.

(8) J. R. WAIT "Electromagnetic induction technique for locating a buried source", IEEE Trans. Geosci. Electronics, Vol.GE.9, No. 2, p. 95, April 1971.

(9) R. M. DUNBAR "The performance of a magnetic loop transmitter-receiver system submerged in the sea", Radio and Electron Engr., Vol. 42, No. 10, p. 457, October 1972.

(10) I. S. BOGIE "Conduction and magnetic signalling in the sea - A background review", Radio and Electron Engr., Vol. 42, No. 10, p. 447, October 1972.

(11) J. E. MCFEE and Y. DAS "Determination of the parameters of a dipole by measurement of its magnetic field", IEEE Trans. Ant and Prop., Vol. AP.29, No. 2, p. 282, March 1981.

(12) D. COHEN "Measurements of the magnetic fields produced by the human heart, brain and lungs", IEEE Trans., Vol. MAG.11, No. 2, March 1975.

(13) A. ALDEEN and J. BLITZ "Eddy current investigations of oblique longitudinal cracks in metal tubes using a mercury model", NDT International, p. 211, October 1979.

(14) M. L. BURROW "ELF communications antennas", Peter Peregrinus, England, 1978.

(15) M. H. ACUNA "Flux-gate magnetometers for outer planets exploration", IEEE Trans. Magnet. Vol. MAG.10, No. 3, p. 519, September 1974.

(16) F. F. MOBLEY, L. D. ECKARD, G. H. FOUNTAIN and G. W. OUSLEY "Magsat, a new satellite to survey the earth's magnetic field", IEEE Trans. Maget., Vol. MAG.16, No. 5, p. 758, September 1980.

(17) D. E. O'N WADDINGTON "Beat frequency oscillator metal detector", Wireless World, p. 45, April 1977.

(18) A. FLIND "Induction balance metal detector", Metal Detecting, Technical Forum, March 1979.

(19) F. S. GRANT and G. F. WEST "Interpretation theory in applied geophysics", McGraw-Hill, 1965.

(20) J. A. CORBYN "Pulse induction metal detector", Wireless World, p. 40, March 1980.

(21) K. L. SCOTT "Variation of the inductance of the coils due to the magnetic shielding effect of eddy current in the cores". Proc. IRE, Vol. 18, No. 10, p. 1750, October 1930.

(22) R. LAGAL and C. GARRETT "The theory behind the VLF/TR", Metal Detecting, August 1979.

(23) A. FLIND "Technical forum, Part 6", Metal Detecting, August 1979.

(24) R. LAGAL and C. GARRETT "VLF/TR metal detector handbook", 1979.

(25) K. ASAKAWA, Y. SHIRASAKI and Y. IWAMOTO "Metal detector for tracing submarine telecommunication cables", IEEE Trans. Inst. and Meas., Vol. IM-32, No. 4, p. 477, December 1983.

(26) H. P. WILLIAMS "Antenna theory and design", Pitmans, London, 1966.

(27) YU. A. NARTOV, D. A. GRECHINSKII and V. G. RUIGALIN "Calculations on inductive loop antennae", Soviet J. Inst. and Control, No. 3, p. 13, March 1968.

(28) J. D. KRAUS "Antennas", McGraw-Hill Book Company, USA, 1950.

(29) J. D. S. SCOTT "A telemetry link using electromagnetic induction", Ph.D. Thesis, University of Aston in Birmingham, 1977.

(30) VITKOVITCH "Field anlaysis experimental and computational methods", 1966.

(31) G. LIEBMANN "Electrical analogues", Brit. J. Appl. Phys., No. 4, p. 193, 1953.

(32) P. HAMMOND "Electromagnetism for engineers", Pergamon Press, 1964.

(33) G. H. OLSEN "Field plotting", Wireless World, p. 58, February 1962.

(34) C. OATLEY "Electric and magnetic fields. An introduction", Cambridge University Press, 1976.

(35) G. W. CARTER "The electromagnetic field in its engineering aspects", Longmans, 1967.

(36) W. MACLEAN "Theory of strong electromagnetic waves in massive iron", J. Appl. Phys., Vol. 25, No. 10, p. 1267, October 1954.

(37) P. D. AGARWAL "Eddy current losses in solid and laminated iron", AIEE Trans., Vol. 78, p. 169, May 1959.

(38) A. L. BOWDEN "A study of magnetic non-linearity and finite length effects in solid iron subject to a travelling mmf wave", Ph.D. Thesis, University of Aston in Birmingham, 1973.

(39) A. L. BOWDEN and E. J. DAVIES "Analytic separation of the factors contributing to the eddy-current loss in magnetically non-linear steel", IEE Proc., Vol. 130, Pt. B, No. 5, p. 364, September 1983.

(40) M. L. BROWN "Calculation of 3-dimensional eddy currents at power frequencies", IEE Proc., Vol. 129, Pt. A, No. 1, p. 46, January 1982.

(41) M. J. BALCHIN and J. A. M. DAVIDSON "3-dimensional eddy-current calculation by the network method", IEE Proc., Vol. 130, Pt. A, No. 2, p. 88, March 1983.

(42) H. PORISTSKY and J. M. BUTLER "A.C. flux penetration into magnetic materials with saturation", IEEE Trans. Comm. and Electron., Vol. 83, p. 99, January 1964.

(43) S. RAMO and J. R. WHINNERY "Fields and waves in modern radio", John Wiley and Sons, Inc., New York, 1964.

(44) C. POOL "The switchable separator", Final Year Undergraduate Report, University of Aston in Birmingham, May 1981.

(45) F. PRIMDAHL "The flux-gate mechanism, Part I: The gating curves of parallel and orthogonal flux-gates", IEEE Trans. Magnet., Vol. MAG 6, No. 2, p. 376, June 1970.

(46) P. M. DUNCAN, A. HWANG, R. N. EDWARDS, R. C. BAILEY and G. D. GARLAND "The development and applications of a wide band electromagnetic sounding system using a pseudo-noise source", Geophs., Vol. 45, No. 8, p. 1276, August 1980.

(47) A. A. FATHIMANI "The automation of resonant thermometer probe measurements", Ph.D. Thesis, University of Aston in Birmingham, April 1976.

(48) A. A. ZAKY and R. HAWLEY "Fundamental of electromagnetic field theory", Harrap and Company Limited, 1974.

(49) B. E. JONES "Instrumentation, measurement and feedback", McGraw-Hill Book Company Limited, U.K.,1977.

(50) R. BECKER "Electromagnetic fields and interaction", Blackie and Son Limited, England, 1964.

(51) W. L. CASSELL "Linear electric circuits", John Wiley and Sons Inc., New York, 1964.